On the variational principles of linear and nonlinear resolvent analysis

Thesis by
Benedikt Barthel

In Partial Fulfillment of the Requirements for the
Degree of
Doctor of Philosophy

CALIFORNIA INSTITUTE OF TECHNOLOGY
Pasadena, California

2022
Defended March 16, 2022

Benedikt Barthel
ORCID: 0000-0002-6890-5047

ACKNOWLEDGEMENTS

First and foremost to my advisor, Beverley McKeon, thank you for your patience, wisdom, and encouragement throughout my time at Caltech. You have always been there with the right balance of guidance and "figure it out yourself" attitude. You have given me, and all of your students, the opportunity to pursue our own ideas without ever letting us wander in the dark for too long. You have been both a professional and personal role model, and the opportunity to work with and learn from you has been the honor of a lifetime.

To the other members of my thesis committee, Tim Colonius, Tony Leonard, and Greg Chini, thank you for your constructive feedback and thoughtful questions over the years and during the writing of this thesis. Thank you as well to Xiaojue Zhu, Salvador Gomez, and Yuting Huang who generously provided much of the data used in this thesis. I am also grateful to the Office of Naval Research, which funded much of the work in this thesis under grants ONR N00014-17-1-2307 and N00014-17-1-3022.

To all the members of the McKeon group, thank you not only for the many stimulating academic discussions and collaborations but also for the sense of family fostered among the entire group. I am grateful to Kevin Rosenberg, Sean Symon, Ryan McMullen, and everyone who took the time to answer my countless questions when I was a new (and eventually not so new) student. I would like to thank Salvador Gomez, with whom I had the opportunity to closely collaborate during the last year in what proved to be the most enjoyable scientific venture of my tenure at Caltech. Furthermore, thank you to Morgan Hooper, who has been a true friend from our first class together. Finally, thank you to all the postdocs, Jane Bae, Scott Dawson, Angeliki Laskari, Arslan Ahmed, and Anagha Madhusudanan, who I have had the privilege to learn from over the years.

To the amazing individuals in the Caltech community, including all the students, postdocs, staff, and faculty I have had the privilege to interact with over the years, thank you for making my time at Caltech such an amazing experience. Thank you to Paul Dimotakis, in whose classes I found my passion for mathematics and who has left a profound mark on my approach to scientific research. Thank you to Tony Leonard, who always took the time to listen to my math problems and provide guidance with patience and a good sense of humor. Thank you to all the GALCIT

staff, without whom the department would surely fall apart. Particular thanks to Christine Ramirez, Jamie Meighen-Sei, and Liza Bradulina, who have always been there to solve my problems, no matter how big or small.

To my parents, thank you for your unconditional love and support. I could not possibly do justice to all the ways in which you have shaped me as a person. Your hard work has made possible all the opportunities I have been so fortunate to enjoy. I hope that if I ever have the privilege to be a father, I will be able to provide for my children the same loving home and encouraging environment you have provided for my siblings and I.

To my wife Caroline, thank you for your love and friendship. Meeting you was by far the highlight of my time at Caltech. You have made this whole adventure far more meaningful and enjoyable than it could have ever been without you. You are a daily source of joy and inspiration and I could not be more excited for our life together and all the other adventures yet to come.

This thesis is dedicated to my siblings, Franziska, Julian, and Herbert. Being your big brother has always been my highest priority. For all the times I had the privilege to advise, support, and encourage you, I am grateful, and for the times I have failed, I am sorry.

ABSTRACT

Despite decades of research, the accurate and efficient modeling of turbulent flows remains a challenge. However, one promising avenue of research has been the resolvent analysis framework pioneered by McKeon and Sharma (2010) which interprets the nonlinearity of the Navier-Stokes equations (NSE) as an intrinsic forcing to the linear dynamics. This thesis contributes to the advancement of both the linear and nonlinear aspects of resolvent analysis (RA) based modeling of wall bounded turbulent flows. On the linear front, we suggest an alternative definition of the resolvent basis based on the calculus of variations. The proposed formulation circumvents the reliance on the inversion of the linear operator and is inherently compatible with any arbitrary choice of norm. This definition, which defines resolvent modes as stationary points of an operator norm, allows for more tractable analytical manipulation and leads to a straightforward approach to approximate the resolvent (response) modes of complex flows as expansions in any arbitrary basis. The proposed method avoids matrix inversions and requires only the spectral decomposition of a matrix of significantly reduced size as compared to the original system, thus having the potential to open up RA to the investigation of larger domains and more complex flow configurations. These analytical and numerical advantages are illustrated through a series of examples in one and two dimensions. The nonlinear aspects of RA are addressed in the context of Taylor vortex flow. Highly truncated and fully nonlinear solutions are computed by treating the nonlinearity not as an inherent part of the governing equations but rather as a triadic constraint which must be satisfied by the model solution. Our results show that as the Reynolds number increases, the flow undergoes a fundamental transition from a classical weakly nonlinear regime, where the forcing cascade is strictly down scale, to a fully nonlinear regime characterized by the emergence of an inverse (up scale) forcing cascade. It is shown analytically that this is a direct consequence of the structure of the quadratic nonlinearity of the NSE formulated in Fourier space. Finally, we suggest an algorithm based on the energy conserving nature of the nonlinearity of the NSE to reconstruct the phase information, and thus higher order statistics, from knowledge of solely the velocity spectrum. We demonstrate the potential of the proposed algorithm through a series of examples and discuss the challenges and potential applications to the study and simulation of turbulent flows.

PUBLISHED CONTENT AND CONTRIBUTIONS

Benedikt Barthel, Xiaojue Zhu, and Beverley McKeon. Closing the loop: nonlinear Taylor vortex flow through the lens of resolvent analysis. *Journal of Fluid Mechanics*, 924:A9, October 2021. doi: 10.1017/jfm.2021.623. B.B. developed the theoretical framework, performed the numerical and analytical calculations and was the primary author of the article.

Benedikt Barthel, Salvador Gomez, and Beverley J. McKeon. Variational formulation of resolvent analysis. *Physical Review Fluids*, 7(1):013905, January 2022. doi: 10.1103/PhysRevFluids.7.013905. B.B. developed the theoretical framework, performed all of the numerical and analytical calculations in chapters 2-4 and half of those in chapter 5 and 6, and was the primary author of the article.

TABLE OF CONTENTS

LIST OF ILLUSTRATIONS

LIST OF TABLES

Chapter 1

INTRODUCTION

1.1 Motivation

From the design of airplanes and spacecraft, to the study of natural phenomena ranging from the earth's oceans and atmosphere to the blood flowing through our veins, the physics of fluids is a crucial part of many fields of science and engineering. We make no attempt to summarize the vast history and scope of the field here, but at its heart are the Navier-Stokes equations (NSE) which enforce the conservation of momentum in a fluid. In multi-physics applications, the NSE may be augmented by other equations, however this thesis is restricted to incompressible and purely hydrodynamic flows. In such cases, the NSE are parameterized by a single nondimensional number, the Reynolds number, which quantifies the ratio of inertial to viscous forces. The Reynolds number can generally be interpreted as a measure of overall flow rate or speed of the flow. For low Reynolds numbers, the flow is in an ordered and steady state known as laminar flow. If the Reynolds number is increased beyond a critical value, the flow begins to transition to turbulence (Reynolds, 1883).

Despite decades of research, turbulence remains a challenging problem from both a scientific and engineering point of view. The vast range of spatial and temporal scales make direct simulation of the governing equations impossible for most practical applications. State of the art direct numerical simulations (DNS) generally remain restricted to canonical flows at Reynolds numbers orders of magnitude below those of most engineering applications (Hoyas and Jiménez, 2006). Despite the advent of super-computing, this will likely remain to be the case for the foreseeable future (Pope, 2000; Smits et al., 2011). However, despite its inherently chaotic and high-dimensional nature, it is known that turbulence exhibits a considerable amount of structure in both space and time. The state-space of turbulence seems to preferably visit solutions which exhibit a high degree of spatial and/or temporal coherence, known as coherent structures (Kline et al., 1967; Jiménez, 2018). These coherent structures are known to play important roles in the dynamics of wall-bounded flows (Marusic et al., 2010). Therefore it is often the case that the investigation of a turbulent flow proceeds in two steps. First expensive simulations or experiments are carried out which generate large amounts of data. Second, from the data,

which in its raw form is generally hard to interpret or even visualize, the coherent structures are then extracted using modal analysis techniques such as dynamic mode decomposition (DMD) or proper orthogonal decomposition (POD) (Taira et al., 2017). In other words, the current paradigm of physics discovery is in many ways incredibly inefficient, requiring expensive computations only for most of the data to be thrown out.

These computational challenges motivate the need for reduced order models (ROM's) which allow for the prediction of the dominant coherent structures without direct simulation of the full equations. Such models can generally be grouped into two categories, *"data-driven models"* and *"equations-driven models"*. The former exploit the increasing availability of data from simulations and experiments that *have already been performed* to find patterns without relying on knowledge of the governing equations (Brenner et al., 2019; Kochkov et al., 2021). The latter, the focus of this thesis, aims to predict the dominant physics by deriving or computing one of the following: approximate solutions to the exact equations, exact solutions to approximate equations, or, as is mostly the case, approximate solutions to approximate equations. The term "equations-driven" encompasses a vast range of models from still relatively costly numerical approaches, such as large eddy simulation or generalized-quasi-linear simulations, to cheap numerical models such a linear stability theory, and finally to analytical methods such as weakly-nonlinear theory and asymptotic analysis (Pope, 2000; Schmid and Henningson, 2001; Drazin and Reid, 2004; Marston et al., 2016). This thesis is concerned with highly truncated models. All the results presented herein are either analytical models derived by direct (by hand) manipulation of the governing equations or are able to be cheaply computed on a personal laptop.

In fluid mechanics, the primary mathematical difficulty is the nonlinearity of the governing equations, and thus this subset of of equations-driven ROM's can generally be further categorized into linear (modal) and nonlinear analysis. The former is concerned with the dynamics linearized about a reference state such as a laminar or a turbulent mean solution. Since the linearized equations are independent of the magnitude of the solution, in their most basic form, linear methods are restricted to qualitative predictions. Nonlinear models on the other hand have, in theory, the capability to provide quantitative predictions. However, the inclusion of the nonlinearity generally leads to a significant increase in complexity which often restricts the practical applications of these approaches.

The aim of this thesis is to extend the capabilities of both linear and nonlinear equations-driven models through the implementation of variational calculus and optimization-based techniques. These extensions contribute to the scientific community in two ways. First, by improving the efficiency of numerical ROM's, we aim to increase the scope of problems that may be tackled on a personal computer. Second, by deriving analytical models, we allow for interpretable insights into nonlinear mechanisms underlying the sustenance of turbulence.

1.2 Linear (Modal) Analysis

Due to the difficulty introduced by the nonlinearity, it is common to consider only the linearized form of the governing equations. These are generally derived by performing an asymptotic expansion about some known reference state and considering only the leading order terms (Schmid and Henningson, 2001; Drazin and Reid, 2004). Such methods generally revolve around a matrix decomposition of the linearized differential operator, which results in a set of what are generally referred to as "modes." These modes may in some cases give insight into physical mechanisms in the flow, or may be used as a basis to efficiently represent the solution in conjunction with some other model or calculation. The most basic matrix decomposition is the spectral- or eigen-decomposition. However, many systems in mathematical physics, including the NSE, are non-normal, meaning their eigenvectors are not orthogonal, and in many cases can be nearly parallel. This obscures the physical interpretation of the structures represented by the different eigenmodes and from a practical point of view leads to an ill-conditioned problem susceptible to numerical errors. The singular value decomposition (SVD) circumvents this issue of non-normality and therefore forms the basis of most modern matrix decomposition techniques (Taira et al., 2017).

Linear Stability Theory

In many scientific and engineering applications it is crucial to determine whether a certain solution or configuration is robust (or not) to small perturbations. Therefore, the most widely used avenue of linear analysis is linear stability theory (LST) which determines the stability of the reference state to an infinitesimal perturbation. In LST, one makes the assumption that the solutions to the linearized equations obey an exponential time dependence. This results in an eigenvalue problem for the eigenvalues and eigenvectors of the spatial differential linear operator. If the real part of all eigenvalues is negative, the solution will exhibit exponential decay back

to the reference state for long times, while, if at least one eigenvalue has positive real part, the solution is unstable. In the context of fluid mechanics, one application of such an analysis is the estimation of under what conditions a flow will transition to turbulence. However, some flows transition to turbulence at Reynolds numbers far below those predicted by LST. In these cases the LST prediction fails since stable eigenvalues only signify long time exponential decay, and cannot account for transient growth due to the non-normality of the eigenvectors. This linear transient growth can trigger nonlinear dynamics which lead to transition (Schmid and Henningson, 2001; Drazin and Reid, 2004; Barkley, 2016).

Linear methods have also been used to investigate the stability of time averaged turbulent mean flow profiles. However, since the mean flow is not itself a solution, the physical interpretation of such analyses is not universally agreed upon. This concept was introduced by Barkley (2006) who observed that in the case of cylinder flow the turbulent mean flow was approximately neutrally stable. This property, formally coined "real zero imaginary frequency" (RZIF) by Turton et al. (2015), due to the resulting eigenvalues being purely imaginary, has since been observed in a variety of flow configurations (Bengana and Tuckerman, 2019, 2021). The RZIF property has been used to derive iterative algorithms to self-consistently predict the mean velocity profile in a variety of settings including cylinder flow, thermosolutal convection, and channel flow (Mantič-Lugo et al., 2014, 2015; Beaume et al., 2015; Rosenberg and McKeon, 2019a; Bengana and Tuckerman, 2021). In Chapter 5 of this thesis we extend this approach to a polar coordinate system through the analysis of Taylor Couette flow, the flow between two cylinders.

Resolvent Analysis

Resolvent analysis (RA) considers the forced response of non-normal dynamical systems. This concept was introduced by Trefethen et al. (1993) and Jovanović and Bamieh (2005) who considered the stability and amplification of linearly stable flows to external forcing. Central to RA is the SVD of the resolvent operator, the inverse of the linearized dynamics. The SVD circumvents the non-normality of the operator and provides an orthogonal basis for both the forcing and response. These ideas were later applied to turbulent flows by McKeon and Sharma (2010) who interpreted the nonlinear term in the Navier-Stokes equations as a forcing to the linearized system.

The conceptual framework that has historically been the core of resolvent analysis

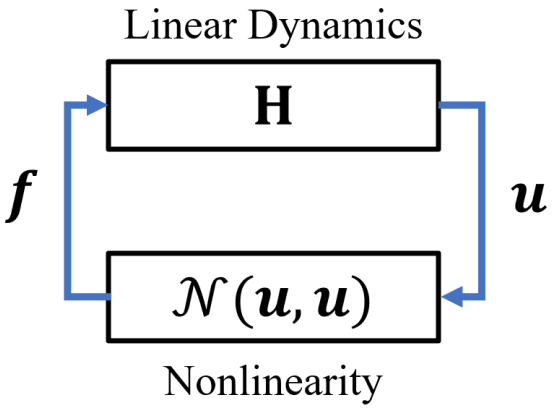

Figure 1.1: Feedback control interpretation of resolvent analysis.

is inspired by control theory (CT). The resolvent operator is interpreted as a transfer function from the forcing to the response. The (velocity) response then feeds back onto the forcing through the nonlinearity of the NSE in a process reminiscent of a feedback control loop, as illustrated in Figure 1.1. The singular values of the resolvent operator represent the linear gain from the input of each resolvent forcing mode to the corresponding response mode. This CT-inspired framework has proven theoretically useful since it is conceptually straightforward and benefits from years of established mathematical machinery. However, from a practical point of view, the reliance on the inversion of the linear operator poses some difficulties. It obscures the analytical tractability of the equations and is computationally costly for all but the simplest systems. Chapter 3 presents an alternative framework based on the calculus of variations which bypasses this inversion. Early on, RA was largely applied to the study of canonical shear flows with only a single non-homogeneous spatial dimension for which the computational cost of the inversion and SVD of the operator is trivial (Jovanović and Bamieh, 2005; McKeon and Sharma, 2010; Hwang and Cossu, 2010; Moarref et al., 2013; Sharma et al., 2017). In these cases, linearly amplified length scales identified by RA were found to correlate with the energetically active scales observed in experiments and simulations, and the corresponding resolvent modes capture the qualitative features of the coherent structures observed in wall turbulence (McKeon, 2017). In particular, resolvent modes have been found to exhibit self-similar behavior characteristic of the attached eddy hypothesis proposed by Townsend (Townsend, 1951; Moarref et al., 2013; McKeon, 2019). Towne et al. (2018) have elaborated on the assumptions under which resolvent response modes correlate with spectral proper orthogonal decomposition (SPOD) modes computed from data, illustrating that RA can predict coherent structure in the full flow field.

More recently, RA has also been extended to 2D flows such as boundary layers (Sipp and Marquet, 2013; Rigas et al., 2021), the flow behind bluff bodies (Symon et al., 2018, 2020), exact coherent states (ECS) (Rosenberg and McKeon, 2019b), and turbulent jets (Schmidt et al., 2018; Pickering et al., 2021). In particular, modal analysis techniques including RA have been used by a variety of authors to implement flow control strategies, for example, to suppress vortex shedding (Gómez and Blackburn, 2017) and delay flow separation (Yeh and Taira, 2019). For these 2D flows, the computational cost and memory requirements becomes considerable and thus the further extension to 3D flows has generally remained limited.

Over the years, these computational challenges have inspired innovative alternative methods of estimating resolvent modes. One area of research has been in so called "matrix-free" methods such as the work of Martini et al. (2021) who use the transient and steady state responses of the periodically forced linearized system and its corresponding adjoint system to estimate the action of the resolvent operator. Another avenue of investigation inspired by the field of data analysis has been in "equation-free" methods such as Herrmann et al. (2021) who use dynamic mode decomposition (DMD) modes to estimate the linear dynamics of a system from a time series of data. Others have made use of iterative Arnoldi Algorithms that replace the cost of calculating the SVD and a matrix inverse with the cost of an LU decomposition and a small amount of matrix multiplications (Sipp and Marquet, 2013; Schmidt et al., 2018). Furthermore, algorithms such as randomized SVD and others have made it possible to efficiently and accurately compute singular modes of data sets that would otherwise be prohibitively expensive (Halko et al., 2011; Moarref et al., 2013; Tropp et al., 2019; Ribeiro et al., 2020).

Resolvent analysis has historically been successful in exploiting the linear dynamics to identify structures in turbulence (McKeon and Sharma, 2010). However, turbulence is by nature a nonlinear phenomenon, therefore recently attempts have been made to explicitly characterize and quantify the influence of nonlinear dynamics within the resolvent framework. For example, Moarref et al. (2014a) and McMullen et al. (2020) used convex optimization to compute reduced order representations of turbulent statistics and Rigas et al. (2021) studied solutions of the Harmonic-Balanced Navier-Stokes equations to identify optimal nonlinear mechanisms leading to boundary layer transition. Additionally, Morra et al. (2021) and Nogueira et al. (2021) have directly computed the nonlinear forcing statistics for minimal channel and Couette flow, respectively, and analyzed the efficacy of low

rank resolvent reconstructions in capturing the relevant dynamics. In this thesis we address both the linear and nonlinear aspects of resolvent analysis.

1.3 Nonlinear Reduced Order Models

While linear models have proven useful in gaining understanding of a variety of physical mechanism in range of canonical and engineering flows, turbulence is a fundamentally nonlinear phenomena and a wide range of physics remains hidden to purely linear models. In particular, since the linearized equations are independent of the magnitude of the state of the system, this approach can not lead to quantitative predictions of the velocity field. In addition to the inherent nonlinearity, another defining characteristic of turbulence is the wide range of relevant spatial and temporal scales. The interaction, and associated energy transfer, between these various scales is the key to the sustenance of the turbulence. When direct simulation of the full equations is not possible, nonlinear reduced order models can provide qualitative and quantitative insight into these scale interactions and provide simplified models of highly complex physics which may be obscured, or difficult to extract from high fidelity data.

Over the decades, a wide range of nonlinear modeling strategies have been proposed, here we focus on two particular models, *'weakly nonlinear (WNL) theory'* and *'quasilinear (QL) theory'* which are most relevant to this thesis. Both of these models proceed by limiting the spatio-temporal scales which are permitted to interact, however they approach this truncation from opposite directions. WNL theory starts with the results of linear models and systematically introduces nonlinearity through an asymptotic expansion. QL theory, on the other hand, begins with the fully nonlinear equations and neglects certain nonlinear interactions to simplify the equations.

Weakly Nonlinear Theory

Weakly nonlinear theory is concerned with flows at conditions near the bifurcation from the laminar state. The foundation is the assumption that spatial structure of the flow in this supercritical regime is given by the unstable eigenmode of the governing equations linearized about the laminar base flow (Barkley, 2006; Gallaire et al., 2016; Ducimetière et al., 2021). The amplitude of this structure, as well as the Reynolds stress driven correction to the base flow, is derived through an asymptotic expansion which sequentially reintroduces the nonlinear interactions under the assumption that

the velocity field at a given length scale is affected only by scales of equal or larger size. The benefits of WNL theory are that it is a primarily analytical theory which allows for simple and interpretable models and since the nonlinearity is reintroduced on a scale-by-scale basis, the fidelity and complexity of the model can be increased in a systematic fashion.

Weakly nonlinear theory is an expansion about the critical Reynolds number, and is therefore only formally valid at Reynolds numbers near that critical Reynolds number. In practice however, some results of WNL theory have been shown to remain accurate at Reynolds numbers significantly above the bifurcation from the laminar state (Stuart, 1960; Yahata, 1977; Jones, 1981; Gallaire et al., 2016). WNL theory fails however if the flow under investigation exhibits subcritical transition, since in such cases the critical Reynolds number predicted by LST is either inaccurate or non-existent, as for example in pipe flow which is linearly stable for arbitrary Reynolds numbers (Schmid and Henningson, 2001; Drazin and Reid, 2004; Barkley, 2016).

Quasilinear Approximation

Quasilinear (QL) and generalized quasilinear (GQL) theory are simplified models of the Navier-Stokes equations which neglect the direct effect of the nonlinear interaction between small scales on the evolution of those small scales. The flow is decomposed into large scales, defined as the Fourier modes corresponding to the N largest streamwise wavelengths, and small scales, all the remaining Fourier modes. QL refers to the limit of $N = 1$, and GQL is the general case of $N > 1$, such that a GQL solution becomes an exact representation of the equations in the limit as N approaches the spectral resolution. The interaction between the small scales is neglected from the equations governing the evolution of those same small scales, while the equation governing the large scales remains unaltered (Marston et al., 2016; Hernández and Hwang, 2020; Hernández et al., 2021). This results in a system where the equations governing the large scales is fully nonlinear, while the equation for the small scales is linear, although still coupled to the large scales.

This approach is closely related to what is been called a reduced-nonlinear (RNL) model which replaces the neglected term in the QL equations with stochastic forcing (Farrell and Ioannou, 2012; Thomas et al., 2014; Farrell et al., 2016) and the 2 dimensional, 3 component (2D/3C) model which further considers only the streamwise constant component (Gayme et al., 2010). All of these approaches have been

shown to result in flow features similar to those observed in true turbulence. In particular GQL approaches have shown that only a small amount of streamwise varying modes lead to very accurate solutions and reproduce the scaling behaviour observed in the exact equations (Marston et al., 2016; Hernández et al., 2021).

1.4 Thesis Outline

In Chapter 2, we derive the basic mathematical foundations of the resolvent framework. Chapter 3 presents an alternative formulation of resolvent analysis based on the calculus of variations. This variational definition allows for improved analytical tractability of the equations, and is used to derive a method to efficiently compute the resolvent modes of 2D/3C systems for which the direct singular value decomposition of the resolvent is computationally expensive. Chapters 4-6 explore the nonlinear aspects of resolvent modeling. In Chapter 4, we use an optimization-based approach to compute accurate models of Taylor vortex flow, a time invariant exact solution of the NSE. This approach leads to a highly truncated, yet fully nonlinear solution through which we investigate the nature of the nonlinear energy cascade. We identify the emergence of an inverse forcing cascade which sets the limits of the domain of validity of weakly nonlinear analysis. Chapter 5 extends the self-consistent mean flow technique introduced by Mantič-Lugo et al. (2014) and Beaume et al. (2015) to the cylindrical geometry of Taylor vortex flow. Finally, in Chapter 6 we suggest an algorithm based on the energy conservation of the NSE for the reconstruction of phase information from the spatio-temporal energy spectrum of turbulent flows. We conclude in Chapter 7 with a discussion of the significance of our results and the avenues for future research.

Chapter 2

RESOLVENT FRAMEWORK

2.1 Background

The resolvent formulation of the NSE introduced by McKeon and Sharma (2010) offers a natural bridge from (forced) linear to explicitly nonlinear analysis. The nonlinearity is replaced with a forcing term, but the nonlinear coupling between the forcing and velocity is formally retained. Here we present the derivation of the resolvent formulation based on the formalism described by McKeon (2017).

2.2 Mathematical Formulation: Linear Analysis

The majority of this thesis will be focused on wall-bounded shear flows, however, let us first consider a general forced linear system

$$\frac{\partial \mathbf{u}}{\partial t} - \mathbf{A}\mathbf{u} = \mathbf{f} \tag{2.1}$$

where $\mathbf{A}$ represents a spatial-linear differential operator and $\mathbf{u}(\mathbf{x}, t), \mathbf{f}(\mathbf{x}, t) \in \mathrm{C}^{\infty}$. The state variables $\mathbf{u}$ and $\mathbf{f}$ are referred to as the *'response'* and *'forcing,'* respectively. We consider the temporal Fourier transform of (2.1) and define the spatio-temporal linear operator

$$\mathbf{L}(\omega) \equiv i\omega\mathbf{I} - \mathbf{A} \tag{2.2}$$

as well as the resolvent operator

$$\mathbf{H}(\omega) \equiv \mathbf{L}(\omega)^{-1} \tag{2.3}$$

which is classically interpreted as a transfer function from the forcing to the response.

$$\hat{\mathbf{u}} = \mathbf{H}\hat{\mathbf{f}} \tag{2.4}$$

For readability, we have dropped explicit reference to the dependence on ω. An SVD of the resolvent

$$\mathbf{H} = \sum_{j=1}^{\infty} \psi_j \sigma_j \phi_j^H \tag{2.5}$$

results in a pair of distinct sets of basis functions for the response (ψ_j) and forcing (ϕ_j) and are referred to as the resolvent *'response modes'* and *'forcing modes,'* respectively. These are ordered by their gains σ_j that are ordered in descending

order, representing the jth largest linear gain possible. The optimal forcing mode, ϕ_1, represents "the most dangerous" input, in that it leads to a response with the highest possible linear gain, σ_1. The corresponding optimal response mode ψ_1 then represents the linearly most amplified structure.

The benefit of such a decomposition is that in many applications of interest the resolvent operator is very low rank, meaning that the first few singular values are much greater than the rest. This allows for highly truncated "low rank" representations of the resolvent which can lead to drastic model reduction (McKeon, 2017). Here and throughout this thesis superscript ^{H} denotes the Hermitian adjoint, or for discrete matrices the conjugate transpose. By the definition of the SVD, both the response and forcing modes are orthogonal with respect to the relevant inner products.

$$\langle \psi_i, \psi_j \rangle_u = \langle \phi_i, \phi_j \rangle_f = \delta_{ij} \tag{2.6}$$

We will see in the following chapters that the inner products $\langle\rangle_u$ and $\langle\rangle_f$ depend on the system under investigation, are generally distinct, and in any numerical implementation may generally be defined by the user. Finally, we note that if the operator $\mathbf{H}$ is normal, then the SVD is equivalent to a spectral decomposition, and the response and forcing modes will be equal to each other and (up to a complex phase) the eigenvectors of $\mathbf{H}$.

2.3 Mathematical Formulation: Nonlinear Analysis

Resolvent analysis is relevant to any type of forced linear system, however our focus is on the NSE for which the forcing $\mathbf{f}$ is a quadratic nonlinear function of the state $\mathbf{u}$ which represents the fluctuation about some known base state.

$$\frac{\partial \mathbf{u}}{\partial t} - \mathbf{A}\mathbf{u} = \mathbf{f} \equiv \mathcal{N}(\mathbf{u}, \mathbf{u}) \tag{2.7}$$

The wall-bounded shear flows considered here are statistically stationary and homogeneous in at least one spatial dimension, $\mathbf{x}$, motivating the spatio-temporal Fourier transform of the state

$$\hat{\mathbf{u}}_{\mathbf{k}}(\mathbf{y}) \equiv \int_{-\infty}^{\infty} \mathbf{u}(\mathbf{x}, \mathbf{y}, t) e^{-i(\mathbf{k}_\mathbf{x} \cdot \mathbf{x} - \omega t)} \mathbf{d}\mathbf{x} dt \tag{2.8}$$

as well as the forcing

$$\hat{\mathbf{f}}_{\mathbf{k}}(\mathbf{y}) \equiv \int_{-\infty}^{\infty} \mathbf{f}(\mathbf{x}, \mathbf{y}, t) e^{-i(\mathbf{k}_\mathbf{x} \cdot \mathbf{x} - \omega t)} \mathbf{d}\mathbf{x} dt \tag{2.9}$$

where $\mathbf{k} \equiv [\mathbf{k}_\mathbf{x}, \omega]$. The spatial variable $\mathbf{y}$ represents the non-homogeneous spatial dimension(s), which includes, but it not necessarily limited to, the wall normal

direction. The explicit Fourier transform of the nonlinear term allows us to write the NSE as a linear system

$$\hat{\mathbf{u}}_{\mathbf{k}} = \mathbf{H}_{\mathbf{k}}\hat{\mathbf{f}}_{\mathbf{k}} \tag{2.10}$$

coupled to the nonlinear definition of the forcing

$$\hat{\mathbf{f}}_{\mathbf{k}} = \int_{\mathbf{k}_a+\mathbf{k}_b=\mathbf{k}} \hat{\mathcal{N}}\left(\hat{\mathbf{u}}_{\mathbf{k}_a}, \hat{\mathbf{u}}_{\mathbf{k}_b}\right) \mathbf{d}\mathbf{k}_a \mathbf{d}\mathbf{k}_b. \tag{2.11}$$

Here the resolvent operator $\mathbf{H}_{\mathbf{k}}$ is defined at each wave number $\mathbf{k}$ as the inverse of the linear dynamics as in (2.3) and $\hat{\mathcal{N}}(\cdot,\cdot)$ is the Fourier transformed nonlinear term in (2.7). The restriction of the convolution integral over the wave number vectors $\mathbf{k}_a + \mathbf{k}_b = \mathbf{k}$ is a result of the quadratic nature of the nonlinearity and is referred to as the *"triadic compatibility"* constraint. Physically this implies that the solution at a particular spatio-temporal scale (wave number vector) is forced through the nonlinear interactions of a highly restricted subset of scales. As we will see in Chapter 4, the subset of permissible triadic interactions will be limited even further if the solution exhibits any discrete spatio-temporal symmetries such as for example a characteristic wavenumber or frequency. The SVD of the resolvent operator (2.5) provides a basis for the Fourier modes of the state as well as the forcing

$$\hat{\mathbf{u}}_{\mathbf{k}}(\mathbf{y}) = \sum_{j=1}^{\infty} \sigma_{\mathbf{k},j}\chi_{\mathbf{k},j}\psi_{\mathbf{k},j}(\mathbf{y}) \tag{2.12}$$

$$\hat{\mathbf{f}}_{\mathbf{k}}(\mathbf{y}) = \sum_{j=1}^{\infty} \chi_{\mathbf{k},j}\phi_{\mathbf{k},j}(\mathbf{y}) \tag{2.13}$$

where $\psi_{\mathbf{k},j}$, $\phi_{\mathbf{k},j}$, and $\sigma_{\mathbf{k},j}$ are the singular vectors and singular values of $\mathbf{H}_{\mathbf{k}}$. The unknown $\chi_{\mathbf{k},j}$ are the projections of the forcing modes $\phi_{\mathbf{k},j}$ onto the full forcing $\hat{\mathbf{f}}_{\mathbf{k}}$.

$$\chi_{\mathbf{k},j} \equiv \langle \phi_{\mathbf{k},j}, \hat{\mathbf{f}}_{\mathbf{k}} \rangle_f \tag{2.14}$$

Plugging the resolvent mode expansions (2.12) and (2.13) into the definition of the nonlinear forcing (2.11) results in

$$\sum_{j=1}^{\infty} \chi_{\mathbf{k},j}\phi_{\mathbf{k},j} = \sum_{\mathbf{k}_a+\mathbf{k}_b=\mathbf{k}} \sum_{j_a=1}^{\infty} \sum_{j_b=1}^{\infty} \chi_{\mathbf{k}_a,j_a}\chi_{\mathbf{k}_b,j_b}\sigma_{\mathbf{k}_a,j_a}\sigma_{\mathbf{k}_b,j_b}\hat{\mathcal{N}}\left(\psi_{\mathbf{k}_a,j_a}, \psi_{\mathbf{k}_b,j_b}\right) \tag{2.15}$$

where we have replaced the integral over the wave numbers with a summation, since in all practical applications the relevant wave numbers will be discrete. Projecting both sides of (2.15) onto each of the orthonormal forcing modes $\phi_{\mathbf{k},j}$ results in

$$\chi_{\mathbf{k},j} = \chi_{\mathbf{k}_a,j_a}\chi_{\mathbf{k}_b,j_b}N_{\mathbf{k},\mathbf{k}_a,\mathbf{k}_b,j,j_a,j_b} \tag{2.16}$$

where we have dropped the summations for clarity such that the summation over $\mathbf{k}_a, \mathbf{k}_b, j_a, j_b$ is implied. The $N_{\mathbf{k},\mathbf{k}_a,\mathbf{k}_b,j,j_a,j_b}$ are known as the *'interaction coefficients'* (Moarref et al., 2014b) and are defined as

$$N_{\mathbf{k},\mathbf{k}_a,\mathbf{k}_b,j,j_a,j_b} \equiv \sigma_{\mathbf{k}_a,j_a}\sigma_{\mathbf{k}_b,j_b}\langle \boldsymbol{\phi}_{\mathbf{k},j}, \hat{\boldsymbol{\mathcal{N}}}\left(\boldsymbol{\psi}_{\mathbf{k}_a,j_a}, \boldsymbol{\psi}_{\mathbf{k}_b,j_b}\right)\rangle_f \delta_{\mathbf{k}_a+\mathbf{k}_b,\mathbf{k}} \tag{2.17}$$

where the $\delta_{\mathbf{k}_a+\mathbf{k}_b,\mathbf{k}}$ enforces the triadic compatibility constraint. Note that these interaction coefficients depend only on the linear resolvent operator (Sharma et al., 2017). Equation (2.16) constitutes an infinite set of coupled polynomial equations for the resolvent weights $\chi_{\mathbf{k},j}$. We note that so far we have made no assumptions or simplifications and thus the solution of these polynomial equations represents an exact solution of the continuous nonlinear system (2.7).

To summarize, a resolvent analysis-based approach to solve a nonlinear system of the form (2.7) aims to express each Fourier mode of the solution as an expansion in resolvent modes as in (2.12). Generally speaking the solution involves two steps. First, a linear calculation: the singular value decomposition of the resolvent operator (2.5), which is assumed to be known a priori. Second, a nonlinear calculation: solving an appropriately truncated version of the polynomial interaction coefficient Equation (2.16). This thesis explores innovations in both the linear and nonlinear aspects of the resolvent analysis.

Chapter 3

A VARIATIONAL DEFINITION OF RESOLVENT ANALYSIS

3.1 Introduction

The majority of past resolvent analysis research has focused on the control theory interpretation of resolvent analysis and the SVD-based definition of resolvent modes introduced in Chapter 2. Here we take an alternative approach and propose an equivalent definition based on an extension of the min-max principle. The min-max principle itself and the concept of an optimal forcing and maximum gain are well understood and have been used extensively by a wide range of authors. For example, Dawson and McKeon (2019) derived analytical models of the optimal resolvent mode in wall bounded shear flows, Monokrousos et al. (2010) and Garnaud et al. (2013) investigated the optimal forcing structure in a Blasius boundary layer and incompressible jets, respectively, and Towne et al. (2015) computed data-driven resolvent modes in the context of turbulent jets. However, we present an explicit extension from the min-max principle, to what we coin "variational resolvent analysis" (VRA), which constitutes an alternative definition of the resolvent basis that includes all modes. [1]

This variational definition is based on the solutions of the Euler-Lagrange equations associated with the constrained variation of the operator norm of the linearized equations. Critically, this definition does not involve the inversion of any operator, which is useful from both a theoretical and practical sense. The inversion of large matrices is both costly and obscures the intuitive interpretation of the underlying linear differential operator. The extension of the min-max principle to include all resolvent modes was used by Sipp and Marquet (2013) who defined the resolvent forcing modes as the solutions to a generalized eigenvalue problem. The current work builds on their results by additionally avoiding the inversion of the linear operator and the need for any adjoint equations. While in general the resulting Euler-Lagrange equations remain difficult to solve exactly, this variational formulation allows for the approximation of two- or three-dimensional resolvent modes as an expansion in any convenient basis, such as for example a much cheaper one-dimensional resolvent basis, an analytical basis such as that described by Dawson

[1] The contents of this chapter have been published in *Physical Review Fluids*, 7(1): 013905.

and McKeon (2019), or a data-driven one. Further, it requires only the eigenvalue decomposition of a matrix of significantly reduced size. In this chapter, we illustrate how this variational definition is useful in both gaining physical insights by allowing for analytical progress in simplified systems, and by reducing computational cost in complex systems. To illustrate the former, we consider the case of streamwise constant fluctuations in wall bounded shear flows. To investigate the latter, we first perform RA about a 2D/3C exact coherent solution, where we find that we can accurately approximate the resolvent response modes and reduce the computational complexity by an order of magnitude. Finally, the VRA formulation is applied to a streamwise developing turbulent boundary layer, where the near wall modes can be predicted with a 97% reduction in computational cost using resolvent modes calculated using a 1D mean flow.

A Variational Definition of Resolvent Modes

As introduced in Chapter 2, we consider a forced linear system

$$\frac{\partial \mathbf{u}}{\partial t} - \mathbf{A}\mathbf{u} = \mathbf{f} \tag{3.1}$$

where $\mathbf{A}$ represents a spatial-linear differential operator and $\mathbf{u}(\mathbf{x}, t), \mathbf{f}(\mathbf{x}, t) \in \mathrm{C}^\infty$ are defined on a domain $\mathbf{x} \in \Omega$ and $t \in [0, \infty)$. We restrict our analysis to fields $\mathbf{u}(\mathbf{x}, t)$ and $\mathbf{f}(\mathbf{x}, t)$ which are infinitely differentiable and satisfy either periodic or homogeneous Dirichlet or Neumann boundary conditions on the boundary $\partial\Omega$. As in Chapter 2 we consider statistically stationary flows, and thus define the temporally Fourier transformed linear operator

$$\mathbf{L}(\omega) \equiv i\omega\mathbf{I} - \mathbf{A}. \tag{3.2}$$

A key contribution of this thesis is the observation that resolvent response modes (2.5) defined in Chapter 2 as the singular modes of the resolvent operator $\mathbf{H} \equiv \mathbf{L}^{-1}$ may be equivalently defined as the stationary points, $\mathbf{q}^*$, of the operator norm of the linear operator $\mathbf{L}$ under the condition that the argument $\mathbf{q}^*$ satisfies some norm constraint. More explicitly, the resolvent response modes are defined as the stationary points of the functional

$$J = \|\mathbf{L}\mathbf{q}\|_a^2 \tag{3.3}$$

subject to the constraint

$$\|\mathbf{q}\|_b^2 = 1, \tag{3.4}$$

where again the boundary conditions on $\mathbf{q}$ are understood to be either homogeneous or periodic. In general, the norms $||\mathbf{x}||_a \equiv \mathbf{x}^H\mathbf{Q}_a\mathbf{x}$ and $||\mathbf{x}||_b \equiv \mathbf{x}^H\mathbf{Q}_b\mathbf{x}$ need not be the same, such as for example in the Orr-Sommerfeld and Squire decomposition discussed in §3.2. In hydrodynamic analysis these norms generally represent kinetic energy, but in other context other types of norms may be of physical or practical interest. Following the notation of Herrmann et al. (2021) the Cholesky factorization may be used to decompose the weight matrix

$$\mathbf{Q}_a = \mathbf{F}_a^H\mathbf{F}_a. \tag{3.5}$$

This allows a general norm to be related to the Euclidean 2 norm. In other words, we can express any arbitrary user defined norm as

$$||\mathbf{x}||_\alpha = ||\mathbf{F}_\alpha\mathbf{x}||_2 \tag{3.6}$$

where α is simply a label used to distinguish between different norms.

The method of Lagrange multipliers allows us to combine (3.3), (3.4) and the definition (3.6) to formulate a constrained variational problem and define a Lagrangian

$$\mathcal{L}(\mathbf{q}) = ||\mathbf{F}_a\mathbf{L}\mathbf{q}||_2^2 - \sigma^{-2}||\mathbf{F}_b\mathbf{q}||_2^2 = \mathbf{q}^H\mathbf{L}^H\mathbf{Q}_a\mathbf{L}\mathbf{q} - \sigma^{-2}\mathbf{q}^H\mathbf{Q}_b\mathbf{q}. \tag{3.7}$$

Because we have restricted ourselves to homogeneous or periodic boundary conditions, the boundary terms arising in the variational analysis drop out. Therefore, $\mathbf{L}$ and $\mathbf{F}$ may be either interpreted as continuous differential operators or discrete matrices. The vanishing of the variation with respect to the conjugate state $\mathbf{q}^*$ is a necessary and sufficient condition for the stationarity of (3.7). The reader is referred to Appendix A.1 for a derivation of this property based on the work of Wirtinger (1927) and Brandwood (1983). The resolvent response modes of $\mathbf{H} = \mathbf{L}^{-1}$ are then defined as the solutions to the Euler-Lagrange equations given by

$$\frac{\delta\mathcal{L}}{\delta\mathbf{q}} = \mathbf{L}^H\mathbf{Q}_a\mathbf{L}\mathbf{q} - \sigma^{-2}\mathbf{Q}_b\mathbf{q} = 0. \tag{3.8}$$

Equation 3.8 constitutes an eigenvalue problem and thus has a countably infinite set of solutions which we index by the subscript j.

$$\mathbf{L}^H\mathbf{Q}_a\mathbf{L}\boldsymbol{\psi}_j = \sigma_j^{-2}\mathbf{Q}_b\boldsymbol{\psi}_j \tag{3.9}$$

We have denoted the eigenvalue σ_j^{-2} and the eigenfunctions $\boldsymbol{\psi}_j$, such that the singular values and resolvent response modes of $\mathbf{H}$ are given by σ_j and $\boldsymbol{\psi}_j$ respectively. The resolvent forcing modes are recovered through

$$\boldsymbol{\phi}_j = \sigma_j\mathbf{L}\boldsymbol{\psi}_j. \tag{3.10}$$

Note that the ψ_j are guaranteed to be orthogonal w.r.t $\mathbf{Q}_b$ since the matrices in (3.9) are Hermitian, and the ϕ_j are orthogonal w.r.t $\mathbf{Q}_a$ since

$$\phi_i^H \mathbf{Q}_a \phi_j = \sigma_i \sigma_j \psi_i^H \mathbf{L}^H \mathbf{Q}_a \mathbf{L} \psi_j = \sigma_i \sigma_j^{-1} \psi_i^H \mathbf{Q}_b \psi_j = \delta_{ij}. \tag{3.11}$$

These results can alternatively be derived through successive applications of the min-max principle. Therefore, this variational formulation is not novel in it's mathematical results, but rather in its philosophical interpretation of them. While we consider only quadratic norm, the variational formulation is not restricted to this choice. It thus has the potential to expand the resolvent framework to norm spaces not accessible through linear algebra based approaches, which are generally restricted to quadratic norms. However, we reiterate that such extensions are beyond the scope of this work and are not pursued in this thesis

Other researchers have used variational-based approaches to the study of forced linear dynamics and we would like to comment briefly on how Equations (3.9) and (3.10) differ from these past studies. Monokrousos et al. (2010) formulated a variational problem to identify the optimal forcing structure, which as formulated therein necessitated the introduction of an adjoint equation, which is avoided in the current formulation. Sipp and Marquet (2013) solved a generalized eigenvalue problem to compute the resolvent forcing modes and then recovered the response modes by solving the linear system in Equation 3.10. Here we avoid any operator inversion by first computing the response modes and then recovering the forcing modes afterwards. More fundamentally, we view the variational definition proposed herein as a theoretical framework rather than simply a computational strategy. In §3.1, we present one possible technique for how this framework can be used in practice.

Proof of Equivalence

We will now illustrate the equivalence of (3.9) to the standard SVD-based definition, focusing on the case where $||\mathbf{x}||_a = ||\mathbf{x}||_b$. Again, following the notation of Herrmann et al. (2021), the SVD of the properly weighted resolvent operator is given by

$$\mathbf{H}_F \equiv \mathbf{F}\mathbf{H}\mathbf{F}^{-1} = \mathbf{\Psi}_F \mathbf{\Sigma} \mathbf{\Phi}_F^H. \tag{3.12}$$

The physical resolvent forcing and response modes are then recovered by left multiplication by $\mathbf{F}^{-1}$, such that $\mathbf{\Phi} = \mathbf{F}^{-1}\mathbf{\Phi}_F$ and $\mathbf{\Psi} = \mathbf{F}^{-1}\mathbf{\Psi}_F$, whose columns give the individual modes ϕ_j and ψ_j, respectively. We focus first on the resolvent response

modes $\mathbf{\Psi}$. Beginning from the definition of the weighted resolvent, we can write

$$\mathbf{H}_F \mathbf{H}_F^H = \mathbf{\Psi}_F \mathbf{\Sigma}^2 \mathbf{\Psi}_F^H. \tag{3.13}$$

Next we use (2.3), (3.5), and (3.12) to write the above expression in terms of the linear operator $\mathbf{L}$,

$$\mathbf{F}\left(\mathbf{L}^{-1}\mathbf{Q}^{-1}\mathbf{L}^{-H}\right)\mathbf{F}^H = \mathbf{\Psi}_F \mathbf{\Sigma}^2 \mathbf{\Psi}_F^H. \tag{3.14}$$

Taking the inverse of both sides and noting the unitary nature of $\mathbf{\Psi}_F$, we find

$$\mathbf{F}^{-H}\left(\mathbf{L}^H\mathbf{Q}\mathbf{L}\right)\mathbf{F}^{-1} = \mathbf{\Psi}_F \mathbf{\Sigma}^{-2} \mathbf{\Psi}_F^H. \tag{3.15}$$

Finally, we right multiply by $\mathbf{\Psi}_F$ and left multiply by $\mathbf{F}^H$ to arrive at

$$\left(\mathbf{L}^H\mathbf{Q}\mathbf{L}\right)\mathbf{\Psi} = \mathbf{Q}\mathbf{\Psi}\mathbf{\Sigma}^{-2} \tag{3.16}$$

which is equivalent to (3.9). Again, the resolvent forcing modes are then recovered through

$$\mathbf{\Phi} = \mathbf{L}\mathbf{\Psi}\mathbf{\Sigma}. \tag{3.17}$$

This establishes the equivalence of the variational and SVD-based definitions of resolvent modes. We would like to emphasize that a consequence of this equivalence is that the completeness property of the SVD-based basis also applies to the variational computed basis.

Resolvent Mode Estimation

In general, the Euler-Lagrange Equations (3.9) are both analytically intractable and computationally intensive for complex flows with multiple non-homogeneous spatial dimensions. However, the variational definition introduced here provides a convenient way to estimate resolvent modes as an expansion in any convenient basis. Suppose we wish to estimate the resolvent response modes, $\psi(\mathbf{x})$, of some system defined on a particular domain. Then let $\mathbf{q}_j(\mathbf{x})$ with $(j = 1...r)$ be some known basis defined on that same domain. We can then write the resolvent response modes as an expansion in this basis.

$$\psi = a_j \mathbf{q}_j \tag{3.18}$$

Inserting this expansion into (3.7) transforms the continuous vector field $\mathbf{q} \in \mathrm{C}^\infty$ into a discrete field $\mathbf{a} \in \mathrm{C}^r$, where $\mathbf{a}$ is the vector of amplitudes a_j. The Euler-Lagrange Equation (3.8) then takes the form

$$\mathbf{M}\mathbf{a} - \sigma^{-2}\mathbf{Q}\mathbf{a} = 0, \tag{3.19}$$

where $\mathbf{M}, \mathbf{Q} \in \mathrm{C}^{r\times r}$, $M_{ij} \equiv \mathbf{q}_i^H \mathbf{L}^H \mathbf{Q}_a \mathbf{L} \mathbf{q}_j$, and $Q_{ij} \equiv \mathbf{q}_i^H \mathbf{Q}_b \mathbf{q}_j$. The eigenvectors $\mathbf{a}$ contain the amplitudes a_j which optimally approximate the resolvent response modes in the known basis $\mathbf{q}_j$ and the σ are the associated optimally approximated singular values. For r basis elements, we will have $\mathbf{M}, \mathbf{Q} \in \mathbb{C}^{r\times r}$ and thus we will obtain r eigenvalue/eigenvector pairs, representing r singular mode/singular value pairs. The necessary r depends on both the efficiency of the model basis and the desired level of accuracy. Since (3.19) does not include any inherent approximations, if the input basis is orthogonal the VRA approximation does converge to the exact solution computed via SVD as $r \to \infty$. However, any Galerkin type method, such as the one proposed here, is only valuable as long as the size of the basis, r, is significantly smaller than the size of the discretized system, n. If $r \sim O(n)$ it would be preferable to compute the SVD directly, since one would not be restricted to the span of the input basis, which if poorly chosen, may not accurately model the true resolvent modes. However, we show in the following examples that for large systems a reduction of order r/n of two orders of magnitude is possible.

Throughout this chapter, we use lower dimensional resolvent modes as a modeling basis. In such cases, the input basis elements $\mathbf{q}_j$ are periodic in the wall parallel direction and generally localized around a critical layer (where the wave speed c is equal to the local mean velocity) in the wall normal direction. For example, we might have $\mathbf{q}_j(x, y) \sim \mathbf{g}(y; c)e^{ikx}$ where k is the imposed wavenumber. Thus, for this type of basis, the number of retained spatial wave numbers determines the wall parallel resolution of the VRA model and the number and range of retained wave speeds determines the wall normal span of the VRA reconstruction. Numerically, the primary advantage of the proposed method is the reduction in order , $r \ll n$, and thus its application relies on the condition of having a good modeling basis, which spans the global modes of interest. In the examples discussed here, this choice is guided by physical mechanisms such as the critical layer localization, however if applied to a completely unknown flow some amount of tuning would be required to arrive at a useful basis.

However, we note that other types of modeling basis are possible, for example Towne et al. (2015) used a data driven basis to estimate global resolvent modes in turbulent jets. While the derivation of the model presented in Towne et al. (2015), based on successive applications of the min-max principle, differs from the direct variational derivation presented here, the final eigenvalue problem being solved is mathematically equivalent to (3.19). Their work, coined *empirical resolvent mode*

decomposition aims to estimate resolvent modes that are constrained to lie in the span of the input basis, computed from the full flow field data. This constraint is intended to ensure that the modes are *physical* in the sense that they reflect structures observed in the real flow (Towne et al., 2015). The variational approach described in this chapter is on the other hand an alternative mathematical definition of the resolvent modes without any reference to external data.

3.2 1D Resolvent Analysis: Turbulent Channel Flow

The Orr-Sommerfeld Squire System

As a first example, we consider the incompressible linearized NSE for streamwise constant fluctuations about a turbulent mean in a wall bounded shear flow. This example illustrates the fundamental theory and highlights the analytical manipulation enabled by the VRA framework. The equations are nondimensionalized using the channel half-height and friction velocity. A Fourier transform in the homogeneous spatial directions and time results in a system parametrized by the Reynolds number, R, and the wave number triplet, $\mathbf{k} = [k_x, k_z, \omega]$. Here k_x and k_z denote the wavenumbers in streamwise and spanwise directions, respectively, and ω again represents the temporal frequency. We focus on streamwise constant fluctuations which are useful models of the streamwise elongated structures known to play a crucial role in the sustenance of turbulence (Jiménez and Moin, 1991). Therefore, for the remainder of §3.2, we assume $k_x = 0$.

The forced linearized NSE can be written as

$$\begin{bmatrix} L_{OS} & 0 \\ \bar{U}_y & L_{SQ} \end{bmatrix} \begin{bmatrix} v(y) \\ u(y) \end{bmatrix} = \begin{bmatrix} g_v(y) \\ g_u(y) \end{bmatrix}. \tag{3.20}$$

Here $y \in [-1, 1]$ and $[v, u]$ are the wall-normal and streamwise velocity fluctuations about the streamwise, spanwise, and temporal averaged mean velocity $\bar{U}$. The spanwise velocity is recovered through the continuity equation as $w = ik_z^{-1} v_y$. The right hand side $[g_v, g_u]^T$ represents an unknown forcing. The relevant boundary conditions are thus $v(\pm 1) = v_y(\pm 1) = u(\pm 1) = 0$. Note that we write (3.20) in terms of u instead of the classical formulation in terms of the wall normal vorticity $\eta \equiv ik_z u - ik_x w$. This is because if $k_x = 0$ then $u \sim \eta$. Note that this implies that the off-diagonal term in (3.20) does not include the ik_z present in more classical formulations. The Orr-Sommerfeld and Squire operators in (3.20) simplify to

$$L_{OS} = -i\omega\nabla^2 - \frac{1}{R}\nabla^4 \tag{3.21}$$

$$L_{SQ} = -i\omega - \frac{1}{R}\nabla^2 \tag{3.22}$$

where $\nabla^2 \equiv \partial_{yy} - k_z^2$. The inner product defining the kinetic energy norm is

$$\langle \mathbf{q}_i, \mathbf{q}_j \rangle_{KE} \equiv \langle v_i^* v_j + k_z^{-2} v_{i,y}^* v_{j,y} + u_i^* u_j \rangle \tag{3.23}$$

where $\langle f(y) \rangle \equiv \int_{-1}^{1} f(y) dy$, $\mathbf{q} = [v, u]$, and $\|\mathbf{q}\|_{KE} = \sqrt{\langle \mathbf{q}, \mathbf{q} \rangle}_{KE}$. It is convenient to also define the following norm associated with the OS operator induced by

$$\langle \cdot \rangle_{OS} \equiv \langle v_i^* v_j + k_z^{-2} v_{i,y}^* v_{j,y} \rangle \tag{3.24}$$

which represents the contribution of v (and thus w) to the kinetic energy and where again the norm is defined as $\|v\|_{OS} = \sqrt{\langle v, v \rangle}_{OS}$. Lastly, it is numerically convenient to implement (3.20) as

$$\begin{bmatrix} \nabla^{-2} L_{OS} & 0 \\ \bar{U}_y & L_{SQ} \end{bmatrix} \begin{bmatrix} v \\ u \end{bmatrix} = \begin{bmatrix} \nabla^{-2} g_v \\ g_u \end{bmatrix} = \begin{bmatrix} \tilde{g}_v \\ g_u \end{bmatrix}. \tag{3.25}$$

In order to compare our variational results to the direct SVD, we use the definition (3.25) going forward.

The Orr-Sommerfeld and Squire Families

It is instructive to decompose the system into the Orr-Sommerfeld (OS) and Squire (SQ) families of modes as suggested by Rosenberg and McKeon (2019b). The OS family corresponds to the forced response due to g_v,

$$\begin{bmatrix} \nabla^{-2} L_{OS} & 0 \\ \bar{U}_y & L_{SQ} \end{bmatrix} \begin{bmatrix} v^{OS} \\ u^{OS} \end{bmatrix} = \begin{bmatrix} \tilde{g}_v \\ 0 \end{bmatrix} \tag{3.26}$$

which upon elimination of $\tilde{g}_v$ from the equation for u^{OS} results in a decoupled system reminiscent of the classical OS/SQ decomposition of linear stability theory (Drazin and Reid, 2004; Schmid and Henningson, 2001).

$$\nabla^{-2} L_{OS} v^{OS} = \tilde{g}_v \tag{3.27}$$

$$L_{SQ} u^{OS} = -\bar{U}_y v^{OS} \tag{3.28}$$

The SQ family of modes, on the other hand, is the forced response to g_u, where by construction $v^{SQ} = 0$.

$$L_{SQ} u^{SQ} = g_u \tag{3.29}$$

Since (3.29) is a normal scalar operator, the resolvent forcing and response modes are proportional to the eigenmodes of L_{SQ}, and the singular values are equal to the inverse of the norm of the eigenvalues of L_{SQ}.

$$\psi_j^{SQ}(y) = \left[0, \sin\left(\frac{j\pi}{2}(y+1)\right)\right] \tag{3.30}$$

$$\phi_j^{SQ}(y) = \left[0, e^{i\arctan\left(\frac{-4R\omega}{\pi^2 j^2 + 4k_z^2}\right)} \sin\left(\frac{j\pi}{2}(y+1)\right)\right] \tag{3.31}$$

$$\sigma_j^{SQ} = \left(\frac{1}{16R^2}\left(\pi^2 j^2 + 4k_z^2\right)^2 + \omega^2\right)^{-1/2} \tag{3.32}$$

The problem thus reduces to finding the OS family of modes associated with (3.26), which in accordance with §2.2, are defined as the stationary points of the associated Lagrangian

$$\mathcal{L}\left(\mathbf{q}^{OS}\right) = \|\nabla^{-2} L_{OS} v^{OS}\|_{OS}^2 - \sigma^{-2}\|\mathbf{q}^{OS}\|_{KE}^2 \tag{3.33}$$

where $\mathbf{q}^{OS} \equiv [v^{OS}, u^{OS}]$, and we have made use of the fact that $g_u = 0$ to simplify the operator norm. In order to eliminate the streamwise velocity u^{OS}, we expand the solution to (3.28) in eigenfunctions of L_{SQ} given by (3.30).

$$u^{OS} = -\frac{1}{\lambda_n^{SQ}} \langle v^{OS} \bar{U}_y u_n^{SQ} \rangle u_n^{SQ} \tag{3.34}$$

This allows us to write the kinetic energy constraint as

$$\|\mathbf{q}\|_{KE}^2 = \langle |v|^2 + k_z^{-2}|v_y|^2 + |u(v)|^2 \rangle = \|v\|_{KE}^2 \tag{3.35}$$

where the third term $u(v)^2$ is given by the square of (3.34). This allows us to rewrite (3.33) as

$$\mathcal{L}\left(v^{OS}\right) = \|\nabla^{-2} L_{OS} v^{OS}\|_{OS}^2 - \sigma^{-2}\|v^{OS}\|_{KE}^2 \tag{3.36}$$

with associated Euler-Lagrange equation

$$\frac{\delta}{\delta v}\left(\|\nabla^{-2} L_{OS} v^{OS}\|_{OS}^2 - \sigma^{-2}\|v^{OS}\|_{KE}^2\right) = 0. \tag{3.37}$$

For $k_x = 0$, the eigenfunctions of L_{OS} may also be derived analytically (Dolph and Lewis, 1958; Jovanović and Bamieh, 2005). Using standard methods, they are found to be

$$\begin{aligned} v_j(y; k_z) = A_j \left[\cos\left(\gamma_j\,(y+1)\right) - \cosh\left(k_z\,(y+1)\right)\right] + \\ B_j \left[\sin\left(\gamma_j\,(y+1)\right) - \gamma_j k_z^{-1} \sinh\left(k_z\,(y+1)\right)\right] \end{aligned} \tag{3.38}$$

$$\lambda_j^{OS} = \frac{1}{R}\left(\gamma_j^2 + k_z^2\right) - i\omega \tag{3.39}$$

where A_j, B_j and γ_j are defined in Appendix A.2 and satisfy $L_{OS}v_j = \lambda_j^{OS}\nabla^2 v_j$ and $\langle v_i, v_j\rangle_{OS} = \delta_{ij}$. Expanding the solution to (3.37) in the basis of OS eigenfunctions (3.38) such that

$$v^{OS} = a_m v_m \tag{3.40}$$

allows us to transform the variation into an optimization over the coefficients a_j.

$$\frac{\partial}{\partial a}\left(\|\nabla^{-2}L_{OS}a_j v_j\|_{OS}^2 - \sigma^{-2}(\|a_j v_j\|_{KE}^2 - 1)\right) = \frac{\partial}{\partial a}\left(|\lambda_j^{OS}|^2 a_j^2 - \sigma^{-2}a_i a_j(\delta_{ij} + U_{in}U_{nj}^H)\right) = 0 \tag{3.41}$$

Here the quantity U_{in} represents the projection of the OS eigenfunctions onto the SQ eigenfunctions through (3.34) such that

$$U_{in} \equiv -\frac{1}{\lambda_n^{SQ}}\langle v_i \bar{U}_y u_n^{SQ}\rangle. \tag{3.42}$$

Upon carrying out the above differentiation with respect to a, we find the eigenvalue problem

$$\|\mathbf{\Lambda}^{OS}\|^2\mathbf{a} = \sigma^{-2}\left(\mathbf{I} + \mathbf{U}\mathbf{U}^H\right)\mathbf{a} \tag{3.43}$$

where $\mathbf{\Lambda}_{ij}^{OS} = |\lambda_i^{OS}|^2\delta_{ij}$. The eigenvectors $\mathbf{a}$ correspond to the coefficients which optimally represent the resolvent response modes of the system (3.26) as a linear combination of the eigenbasis (3.38).

$$\psi_j^{OS} = [a_m^j v_m, u(a_m^j v_m)] \tag{3.44}$$

The singular values σ_j are given by the eigenvalues of (3.43) and the forcing modes are recovered through

$$\phi_j^{OS} = [\sigma_j\nabla^{-2}L_{OS}v_j^{OS}, 0] = [\sigma_j\lambda_m^{OS}a_m^j v_m, 0]. \tag{3.45}$$

Together with the Squire family of resolvent modes (3.30-3.32), the Orr-Sommerfeld family given by (3.44) and (3.45) fully describe the resolvent basis. In Figures 3.1, we plot the real part of the variationally reconstructed Orr-Sommerfeld response and forcing modes along side their numerically computed counterparts for the wave number triplet $[k_x, k_z, \omega] = [0, 6, 0.1]$ and $R = 1000$. The singular values plots are plotted in 3.2a. For this example, the VRA model uses $r = N_{OS} = 20$ basis elements, this value is chosen to show a balance between the accuracy and model

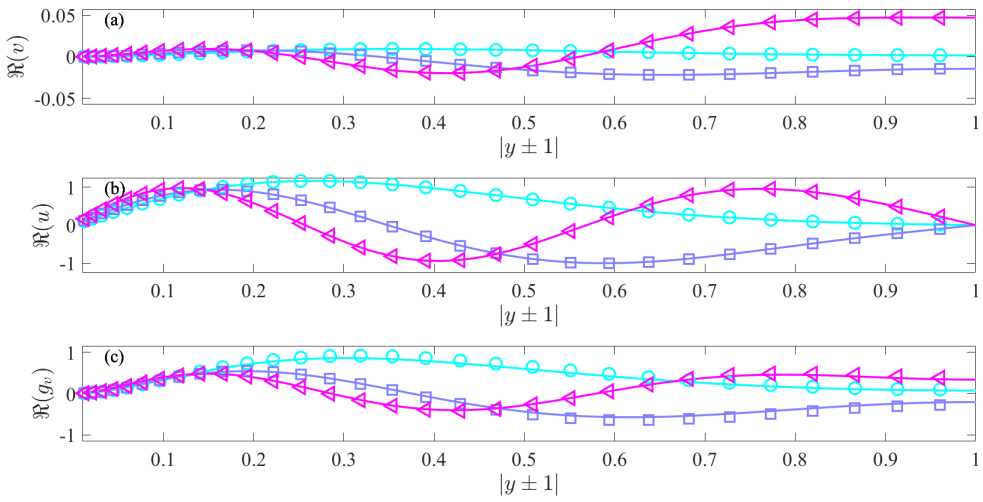

Figure 3.1: Real part of the wall normal component v (a), streamwise component u (b), and forcing g_v (c) of the 1^{st}, 3^{rd}, and 5^{th}, Orr-Sommerfeld family of resolvent modes. Reference modes computed via direct SVD are shown in solid lines, VRA reconstruction using 20 basis eigenmodes is shown in symbols. $k_z = 6$, $\omega = 0.1$, and $R = 1000$.

reduction capabilities of the method. Although for this example the computational cost is trivial, the reduction in size of the relevant matrices and avoiding the need for matrix inversion reduces the computation time by two orders of magnitude. To quantify the convergence of our method, we plot in Figure 3.2 the error in the VRA reconstruction of v, u, and σ as a function of the number of retained OS eigenfunctions ($r = N_{OS}$) included in the variational reconstruction. The error is defined as

$$e_q = \sqrt{\int_{-1}^{1} |q_{svd} - q_{vra}|^2 dy} \tag{3.46}$$

where $q = u, v$ and the subscripts $_{vra}$ and $_{svd}$ denote the quantities computed using the VRA model and direct SVD, respectively. In all cases we observe monotonic convergence. In this example the VRA model is extremely effective at reconstructing the results of the direct SVD since our model basis exactly spans the range of L_{OS}.

Analytical Approximation of ψ_1

In this section, we demonstrate how, under certain assumptions, the variational resolvent formulation allows for the analytical approximation of the leading OS

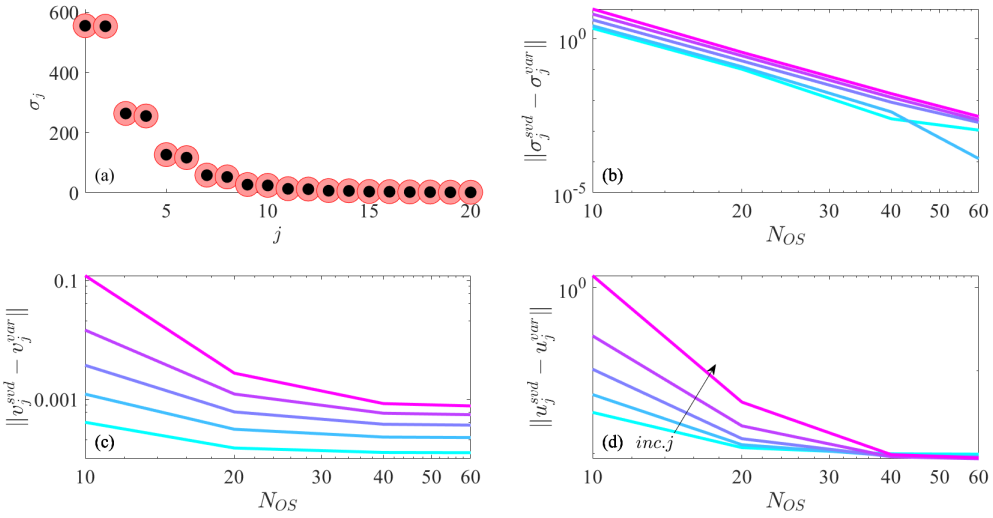

Figure 3.2: Orr-Sommerfeld family of singular values (a) with reference values computed via direct SVD in red, and variational reconstruction using 20 basis eigenmodes in black. Error in variational reconstruction as a function of basis elements in σ_j (b), v_j (c), and u_j (d) of ψ_j for $j = 1, 3, 5, 7, 9$. $k_z = 6$, $\omega = 0.1$, and $R = 1000$ as a function of the retained basis elements $r = N_{OS}$.

resolvent mode ψ_1^{OS}. Written explicitly, the Lagrangian associated with (3.20) is

$$\mathcal{L}(v) = \left(\omega^2 \left(\nabla^2 v\right)^2 + \frac{1}{R^2}\left(\nabla^4 v\right)^2\right) + \frac{1}{k_z^2}\left(\omega^2 \left(\nabla^2 v_y\right)^2 + \frac{1}{R^2}\left(\nabla^4 v_y\right)^2\right) - \frac{1}{\sigma_1^2}\left(u(v)^2 + v^2 + k_z^{-2} v_y^2\right) \quad (3.47)$$

where u is the solution to

$$-i\omega u - \frac{1}{R}\nabla^2 u = -\bar{U}_y v. \quad (3.48)$$

Here u and v are the streamwise and wall normal components of ψ_1^{OS} and σ_1 is the leading OS singular value. The associated Euler-Lagrange equation written in terms of v is then

$$\frac{1}{k_z^2}\left(\frac{1}{R^2}\nabla^{10} + \omega^2\nabla^6\right) v + \frac{1}{\sigma_1^2}\left(\left(L_{SQ}^{-1}\bar{U}_y\right)^H L_{SQ}^{-1}\bar{U}_y v - \frac{1}{k_z^2}\nabla^2 v\right) = 0 \quad (3.49)$$

with boundary conditions $v(\pm 1) = v_y(\pm 1) = u(\pm 1) = 0$. Note that we use the original definition (3.20), not the numerical implementation (3.25), to derive (3.49). This is done to avoid the analytically cumbersome treatment of the ∇^{-2} operator. The problem is now parameterized by ω, R, and k_z. Our analysis will consider the appropriate limits of each in turn.

It has been shown that for $k_x = 0$, the most linearly amplified frequency is $\omega = 0$, therefore we will consider the limit as $\omega \to 0$. Since in this limit (3.49) is regularly perturbed problem, the leading order solution may be found by simply setting $\omega = 0$. We may further simplify (3.49) by considering a high Reynolds number limit $R \to \infty$. Analysis of (3.26) reveals that for $\omega = 0$, $\sigma_1 \sim R^2$ as $R \to \infty$ (see Appendix A.3). This allows us to introduce the small parameter $\epsilon \equiv R^{-1}$ such that (3.49) and (3.48) take the form

$$\frac{1}{k_z^2}\nabla^{10} v + \frac{\epsilon^2}{\tilde{\sigma}_1^2}\left(\frac{1}{\epsilon^2}\left(\nabla^{-2}\bar{U}_y\right)^H \nabla^{-2}\bar{U}_y v - \frac{1}{k_z^2}\nabla^2 v\right) = 0 \tag{3.50}$$

$$\epsilon\nabla^2 u_0 = \bar{U}_y v \tag{3.51}$$

where $\tilde{\sigma} \neq f(R)$. We note that (3.51) implies that $v \sim \epsilon u$ and expand the solution in an asymptotic series.

$$\begin{aligned} v &= \epsilon v_1 + \epsilon^2 v_2 + O(\epsilon^3) \\ u &= u_0 + \epsilon u_1 + \epsilon^2 u_2 + O(\epsilon^3) \end{aligned} \tag{3.52}$$

The leading order solution to (3.50) and (3.51) then satisfy

$$\frac{1}{k_z^2}\nabla^{10} v_1 + \frac{1}{\tilde{\sigma}_1^2}\left(\left(\nabla^{-2}\bar{U}_y\right)^H \nabla^{-2}\bar{U}_y v_1\right) = 0 \tag{3.53}$$

$$\nabla^2 u_0 = \bar{U}_y v_1 \tag{3.54}$$

and the norm constraint takes the form

$$\|u_0\|^2 = 1. \tag{3.55}$$

Here we focus on the leading order solution, and thus to avoid notational clutter, we drop the subscripts $_0$ and $_1$ moving forward.

While we have managed to simplify the governing equations, the second term in (3.53) remains prohibitive to analytical progress. In order to proceed, we consider the $y \to -y$ symmetry of (3.20) which dictates that the resolvent modes come in pairs, one of which is even about the center of the channel, and one of which is odd. If additionally, the modes have compact support, as is generally the case, we have $\psi_1(y) = \psi_1(-y) = \psi_2(y) = -\psi_2(-y)$, and therefore it is sufficient to solve for the mode shape in one half of the domain.

We assume that v is indeed locally supported and thus introduce the scaling $Y = k_z|y \pm 1|$ under the assumption $k_z \gg 1$ and make the transformation $u(y), v(y) \to$

$U(Y), V(Y)$. We note that this scaling differs from the $k_z^{1/2}$ and $k_z^{2/3}$ scaling derived by Arratia and Chomaz (2013) in the context of inviscid transient growth. Formally taking the limit $k_z \to \infty$, allows us to transform the finite domain, $y \in [-1, 1]$, to the "semi-infinite" half channel: $Y \in [0, \infty]$. The solution in the other half of the domain is then recovered through the symmetries: $\psi_1(y) = \psi_1(-y) = \psi_2(y) = -\psi_2(-y)$.

Finally, in order to make progress, we require some suitable approximation of the mean velocity profile. Since we are working within a high Reynolds number limit, we choose to assume that the mean velocity obeys a logarithmic profile over the entirety of the semi-infinite domain. This is a reasonable assumption since in high Reynolds number channel flow the log-law applies to a large fraction of the channel. Our approach thus implicitly assumes the support of the resolvent modes is localized within this region where the log-law approximation is valid. The mean shear is then given in our scaled variables by $\bar{U}_Y = k_z(\kappa Y)^{-1}$, where κ is the Von Karman constant. We note that the mean shear diverges as like Y^{-1} as $Y \to 0$, however, since $V(0) = V_Y(0) = 0$ we have $V(Y) \sim Y^2$ as $Y \to 0$, and thus the right hand side of (3.54) remains bounded as $Y \to 0$.

Inspection of (3.54) and (3.55) reveals that the appropriate scaling of the velocity components is given by $\tilde{U}(Y) = k_z^{1/2}U(Y)$ and $\tilde{V}(Y) = k_z^{3/2}V(Y)$. Additionally, we define the scaled Laplacian $\tilde{\nabla}^2 \equiv \partial_{YY} - 1$ such that $\nabla^2 \to k_z^2\tilde{\nabla}^2$, and note that for $k_x = \omega = 0$ and $k_z \to \infty$ the singular value scales as $\tilde{\sigma}_1 \sim k_z^{-3}$ (see Appendix A.3). Thus we can write (3.53) in our scaled variables as

$$\nabla^{10}\tilde{V} + \frac{1}{\kappa^2 k_z^4 \gamma_1^2}\left(\left(\tilde{\nabla}^{-2}Y^{-1}\right)^H \tilde{\nabla}^{-2}Y^{-1}\right)\tilde{V} = 0 \tag{3.56}$$

where γ_1 is a constant. We expand $\tilde{U}$ and $\tilde{V}$ in asymptotic series

$$\begin{aligned}\tilde{V} &= \tilde{V}_0 + k_z^{-4}\tilde{V}_1 + O(k_z^{-8}) \\ \tilde{U} &= \tilde{U}_0 + k_z^{-4}\tilde{U}_1 + O(k_z^{-8})\end{aligned} \tag{3.57}$$

which upon substitution into (3.56) allows us to eliminate the norm constraint at leading order and reduce the problem of deriving the leading OS resolvent mode to

$$\tilde{\nabla}^{10}\tilde{V} = 0 \tag{3.58}$$

$$\tilde{\nabla}^2\tilde{U} = \frac{1}{\kappa Y}\tilde{V} \tag{3.59}$$

where we have again dropped the subscripts to avoid notational clutter. The relevant boundary conditions are $\tilde{V}(0) = \tilde{V}_Y(0) = \tilde{U}(0) = \tilde{V}(\infty) = \tilde{U}(\infty) = 0$. The remaining constants of integration are then chosen such that $\|\nabla^{-2}L_{OS}V\|_{OS}^2$ is minimized

and $\|U\|^2 = 1$. Here we choose to minimize $\|\nabla^{-2} L_{OS} V\|^2_{OS}$ instead of $\|L_{OS} V\|^2_{OS}$ in order to facilitate comparison with the numerically computed modes. However, minimizing the latter functional leads to a very similar solution. Using standard methods, the solutions satisfying the boundary conditions are found to be

$$V(Y) = \frac{k_z^{3/2}}{R}\left(a + bY + cY^2\right) Y^2 e^{-Y} \tag{3.60}$$

$$U(Y) = -\frac{k_z^{1/2}}{24\kappa}\left(3cY^3 + (4b + 6c)Y^2 + (6a + 6b + 9c)\,(Y + 1)\right) Y e^{-Y}. \tag{3.61}$$

The three remaining constants of integration, a, b, c, are found by minimizing $\|\nabla^{-2} L_{OS} V\|^2_{OS}$ subject to the constraint $\|U\|^2 = 1$. Straight forward integration results in

$$\|\nabla^{-2} L_{OS} V\|^2_{OS} = \frac{1}{R^2}\|\nabla^2 V\|^2_{OS} = 4\frac{k_z^6}{R^4}\left(6a^2 + 9b^2 + 36bc + 72c^2\right) \tag{3.62}$$

and

$$\|U\|^2 = \frac{1}{\kappa^2}\left(\frac{7}{32}a^2 + \frac{1}{128}(112b + 228c)a + \frac{31}{32}b^2 + \frac{351}{64}bc + \frac{1089}{128}c^2\right) = 1. \tag{3.63}$$

Minimizing (3.62) subject to (3.63) results in the eigenvalue problem

$$\begin{bmatrix} 12 & 0 & 0 \\ 0 & 18 & 36 \\ 0 & 36 & 144 \end{bmatrix} \begin{bmatrix} a \\ b \\ c \end{bmatrix} = \frac{1}{\sigma_1^2}\left(\frac{R^4}{4\kappa^2 k_z^6}\right) \begin{bmatrix} 7/16 & 7/8 & 9/4 \\ 7/8 & 31/16 & 351/64 \\ 9/4 & 351/64 & 1089/64 \end{bmatrix} \begin{bmatrix} a \\ b \\ c \end{bmatrix}. \tag{3.64}$$

Assuming $\kappa = 0.4$, the minimizing solution that satisfies the norm constraint is found to be

$$[a, b, c] = [0.1283, 0.1066, 0.0431]\sqrt{2}. \tag{3.65}$$

The leading singular value is

$$\sigma_1 = \|\nabla^{-2} L_{OS}\|^{-1}_{OS} = \frac{R^2}{2k_z^3}. \tag{3.66}$$

The wall normal component g_v of the optimal resolvent forcing mode ϕ_1^{OS} is recovered through

$$\nabla^2 g_v = \sigma_1 L_{OS} v \tag{3.67}$$

subject to the boundary conditions $g_v(\pm 1) = 0$. Using (3.66) and letting $g_v(y) \to G_V(Y)$, this takes the form

$$\tilde{\nabla}^2 G_v(Y) = \sigma_1 L_{OS} v = -\frac{R}{2k_z}\tilde{\nabla}^4 V(Y). \tag{3.68}$$

The solution satisfying the boundary condition $G_V(0) = 0$ is found to be

$$G_V(Y) = k_z^{1/2}\left(4cY^3 + (3b - 6c)Y^2 + (2a - 3b)Y\right)e^{-Y}. \tag{3.69}$$

The solutions (3.60), (3.61), and (3.69) with optimal coefficients (3.65) are plotted in Figure 3.3 alongside numerically computed resolvent modes for $R = 10,000$ and $\omega = 0$ over a range of k_z. Note that for $k_x = 0$, and $\omega \to 0$ the symmetries of (3.25) result in numerical resolvent modes with constant arbitrary phase, which for ease of comparison we set to zero. With the exception of the u component for the smallest wave number ($k_z = 6$), the derived scaling laws lead to reasonable collapse in both the numerically computed resolvent response and forcing modes. As $k_z \to 1$ the assumption of local support in y is no longer valid. In this limit ψ_1 tends to have significant support at the channel center.

For the response modes, the analytically-derived mode accurately predicts the shape, amplitude, and localization of the numerically computed modes. The analytical prediction of the wall normal velocity is most accurate for the largest wave numbers, tending to slightly over predict the amplitude of the smaller wave number modes. This is most likely due to the fact that the amplitude of v is smaller by a factor of $R = 10,000$ and is thus susceptible to some numerical uncertainty since it does not meaningfully contribute to the norm. The streamwise velocity more closely obeys the derived scaling laws, and thus the analytical model accurately predicts the shape of the numerically computed modes for all $k_z > 6$.

The prediction of the forcing mode is slightly less accurate. While we capture the location and amplitude of the peak, the model underpredicts the true mode closer to the wall. The discrepancy in the forcing despite accurate reconstruction of the response is due to the sensitivity of the action of linear operator $L_{OS}v$ to perturbations in the argument v. This is discussed in detail in §3.5.

Finally, in Figure 3.3 we also plot the numerically computed leading singular values alongside the analytical prediction (3.66). While the analytically obtained value of σ_1 slightly under-predicts the true singular values for the smaller values of k_z, the numerical singular values do converge to the analytical prediction with increasing k_z, consistent with the assumption made in our model that $k_z \gg 1$. This under-prediction is consistent with the fact that the true singular value represents the global maximum gain.

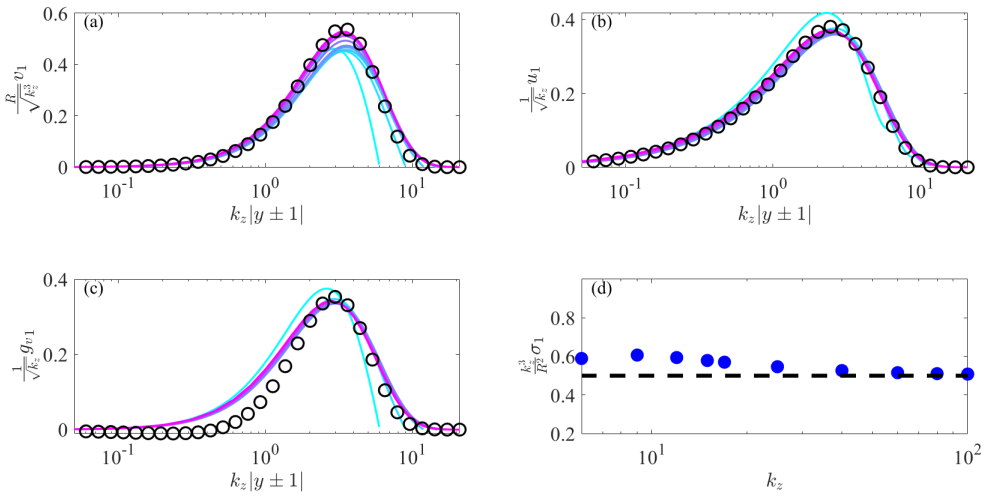

Figure 3.3: Optimal resolvent modes: v (a), u (b), g_v (c) and singular value (d) for $k_x = 0$, $\omega = 0, R = 10,000$ and a range of k_z. Numerically calculated modes/singular values are shown in colored lines/dots, analytically derived modes/singular values are shown in black open circles/dashed line. From light to dark, colors indicate increasing k_z from 6 to 100 (a-c).

3.3 2D Resolvent Analysis: Periodic Mean Flow

In this section, we use VRA to efficiently and accurately compute resolvent modes about a 2D/3C mean flow. We consider the equilibrium solution EQ1 found in plane Couette flow by Nagata (1990). The data was obtained from the open-source database *channelflow.org* (Gibson et al., 2008; Gibson, 2014). The 2D/3C resolvent calculations used to validate the VRA algorithm were performed using a code developed by Rosenberg (2018). In this example, the flow has two non-homogeneous spatial dimensions, the wall normal direction $y \in [-1, 1]$ and the spanwise direction $z \in [-L_z/2, L_z/2]$ with $L_z = 0.8\pi$. The spanwise periodic EQ1 solution is shown in Figure 3.4. The resolvent modes computed about this flow are then parameterized by the streamwise wavenumber and frequency pair, $[k_x, \omega]$. We choose as our modeling basis the local 1D resolvent modes about the mean flow $\bar{U}(y)$ given by the spanwise average of the EQ1 solution: $q_j(y, z) = \psi_j^{1D}(y; k_z, k_x, c)e^{ik_z z}$. In other words, we seek to approximate the 2D resolvent modes from the 1D resolvent basis as

$$\psi^{2D}(y, z; k_x, c) = a_j q_j(y, z). \tag{3.70}$$

The expansion coefficients a_j are found by solving the eigenvalue problem

$$\mathbf{Ma} - \sigma^{-2}\mathbf{Qa} = 0 \tag{3.71}$$

where $M_{i,j} = \langle \mathbf{L}^{2D} q_i, \mathbf{L}^{2D} q_j \rangle$, and $Q_{i,j} = \langle q_i, q_j \rangle$. The operator $\mathbf{L}^{2D}$ is the NS operator, in velocity-vorticity form, linearized about the 2D/3C mean flow, the details of which are discussed in Rosenberg and McKeon (2019a). The operator is discretized in $N_y = 33$ Chebychev points in the wall normal direction, and $N_z = 32$ linearly spaced points in the spanwise direction, for a total of $N_{2D} = 2 \times N_y \times N_z = 2112$ degrees of freedom.

The 1D resolvent modes are computed for the same k_x as the 2D modes, and a range of $N_c = 3$ linearly spaced wavespeeds $0.8c \leq c^{1D} \leq 1.2c$ where $c = \omega/k_x$. We use a range of c^{1D} since the 2D mode is expected to be localized near but not necessarily exactly at the critical layer where $c = \bar{U}(y)$. To account for the variation in z we include a range of $N_{k_z} = 11$ spanwise wavenumbers $k_z = [-5...0...5] \times 2\pi/L_z$. We found that increasing the number of retained harmonics beyond this range did not meaningfully change the results. At each wave number triplet $[k_x, k_z, c]$ we include $N_{SVD} = 8$ resolvent modes, resulting in a total of $r = N_c \times N_{k_z} \times N_{SVD} = 254$ degrees of freedom. These values were chosen to demonstrate a balance between accuracy and the cost saving potential of the proposed method. (The reader is referred to Appendix A.4 for an illustration of some representative basis elements.) Once $\mathbf{L}^{2D}$ is known, the construction of the matrices $\mathbf{M}$ and $\mathbf{Q}$ takes approximately 0.5 seconds and the associated eigendecomposition takes approximately 0.01 seconds on a personal laptop. Meanwhile, the inversion and direct truncated SVD of the original system takes approximately 5 seconds using the built in Matlab functions $mldivide()$ and $svds()$.

In Figures 3.5 and 3.6, we compare the real part of the first four resolvent response modes of the variational reconstruction and the modes computed directly through the SVD of the 2D resolvent for $k_x = 0.5$ and $c = 0.75$ and $R = 400$. The variational approach very accurately reconstructs the true response modes considering the significant reduction in computational complexity.

In Figures 3.7 and 3.8, we plot resolvent forcing modes computed from the response modes through $\boldsymbol{\phi}_j = \sigma_j \mathbf{L}^{2D} \boldsymbol{\psi}_j$. Interestingly we find that while the g_v component is reproduced accurately, the g_η component shows significant discrepancy. While the qualitative shape of the η component of the forcing mode is predicted by the VRA model, the mode is contaminated by higher harmonics. This contamination observed in the VRA reconstruction of the forcing modes, $\boldsymbol{\phi}_j$, despite the accurate reconstruction of the response modes, $\boldsymbol{\psi}_j$, is due to the directional amplification of the resolvent operator or equivalently, a sensitivity of the action of the linear

operator $\mathbf{L}^{2D}\mathbf{q}$, to perturbations in the input $\mathbf{q}$. This phenomenon is discussed in detail in §3.5.

Additionally, in Figure 3.9a we compare the variationally computed singular values with the true values computed via direct SVD. The singular values are estimated relatively accurately, with our model tending to slightly underestimate the leading singular values. As before, the true singular values represent the optimal gains and the predicted singular values are bounded above by the true values. For this combination of spanwise wavenumber and temporal frequency, there is no significant separation of singular values, in other words the resolvent operator is not low rank, and yet our method still accurately predicts the singular values and resolvent response modes.

In order to quantify the convergence properties of the proposed method, for this example we fix $c^{1D} = c^{2D}$, include $k_z = [-5...0...5] \times 2\pi/L_z$ such that $N_c = 1$ and $N_{k_z} = 11$ and compute the error as a function of the number of retained singular modes N_{SVD}. The error is based on the kinetic energy norm and is defined as

$$e \equiv \sqrt{\frac{1}{2L_z}\int_0^{L_z}\int_{-1}^{1} |\boldsymbol{\psi}_{svd}^{2D} - \boldsymbol{\psi}_{vra}^{2D}|^2 dy dz} \tag{3.72}$$

where $\boldsymbol{\psi} = [u, v, w]$. The error is plotted in Figure 3.9 alongside the relative error in singular values for two values of the wave speed, $c = 0.75$ and $c = 0$. The former corresponds to the example plotted in Figures 3.5 through 3.9a where there is no significant singular value separation. The latter case corresponds to a case where the 2D resolvent is more low rank, $(\sigma_1/\sigma_2 \approx 6)$. In both cases, our method is not only able to accurately approximate the leading singular mode and value but also a large range of suboptimal modes and singular values. Interestingly, we see that our method is more accurate in the case where there is less singular value separation. Furthermore, for the low rank case, $(c = 0)$ the largest error in singular value is for σ_1. Again, these findings are a result of the directional nature of the resolvent operator and are discussed in detail in §3.5.

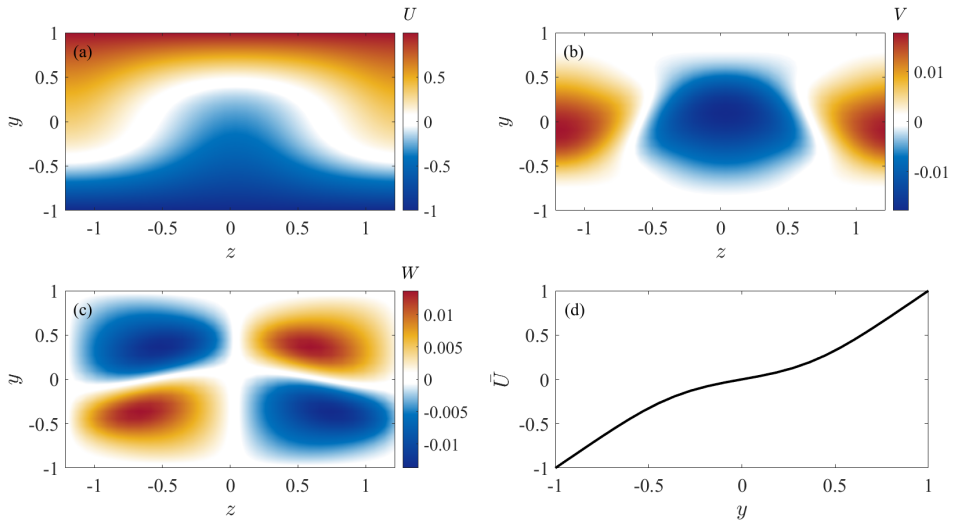

Figure 3.4: Exact coherent state EQ1 at $R = 400$ used to compute 2D resolvent modes: $U(y,z)$ (a), $V(y,z)$ (b), $W(y,z)$(c) and spanwise average $\bar{U}(y)$(d) used to compute the 1D basis modes.

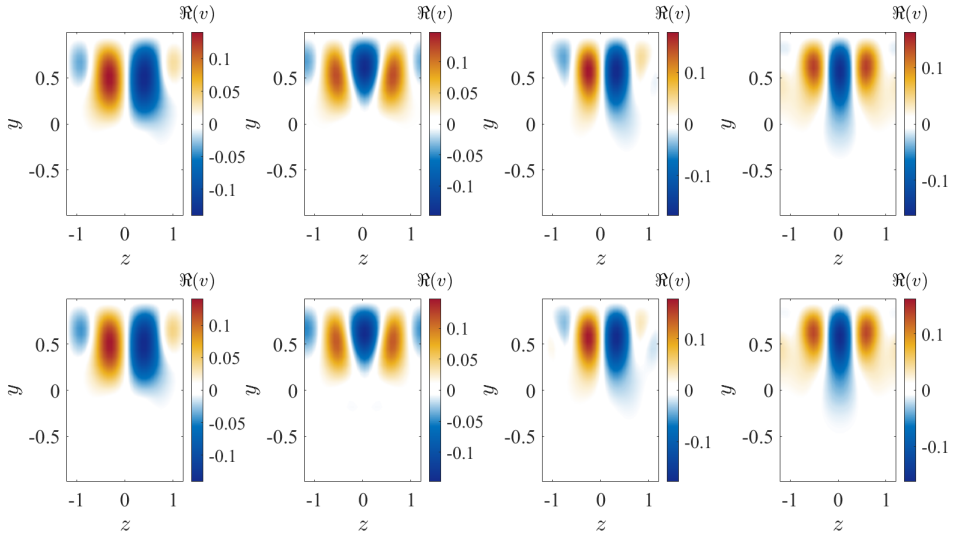

Figure 3.5: Real part of the v component of the first 4 resolvent response modes (ψ_j) for $k_x = 0.5$, $c = 0.75$, and $R = 400$. Top row: true modes, bottom row: VRA model with $N_{k_z} = 11$, $N_c = 3$, and $N_{SVD} = 8$. From left to right: $j = 1, 2, 3, 4$.

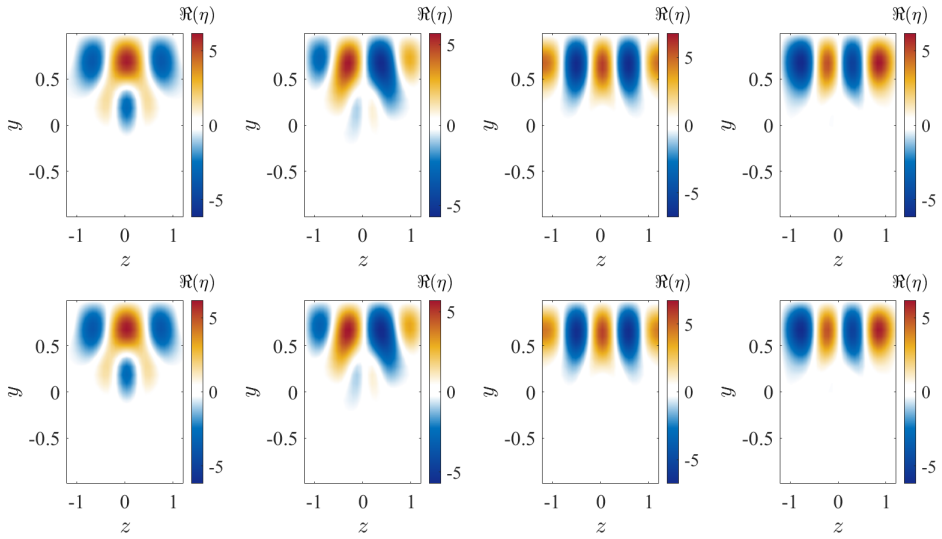

Figure 3.6: Real part of the η component of the first 4 resolvent response modes (ψ_j) for $k_x = 0.5$, $c = 0.75$, and $R = 400$. Top row: true modes, bottom row: VRA model with $N_{k_z} = 11$, $N_c = 3$, and $N_{SVD} = 8$. From left to right: $j = 1, 2, 3, 4$.

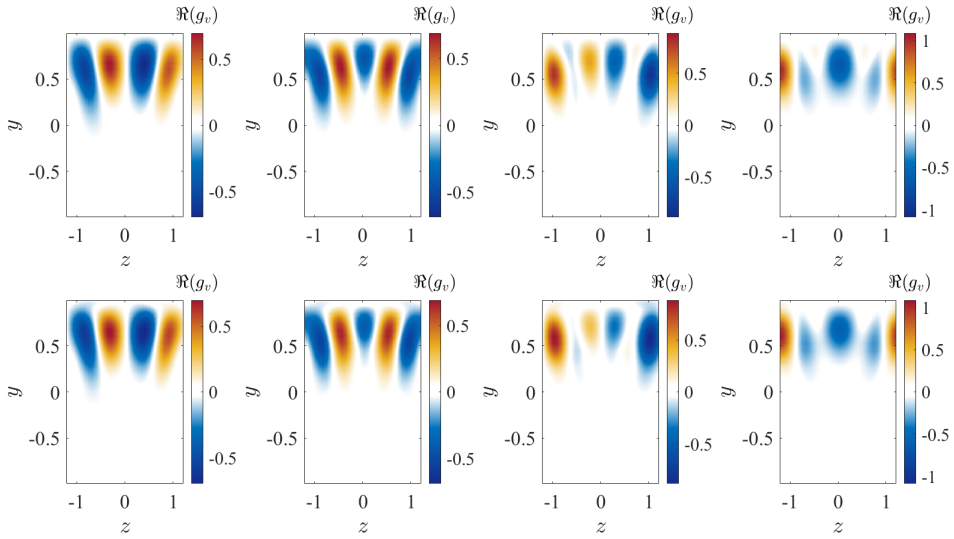

Figure 3.7: Real part of the v component of the first 4 resolvent forcing modes (ϕ_j) for $k_x = 0.5$, $c = 0.75$, and $R = 400$. Top row: true modes, bottom row: VRA model with $N_{k_z} = 11$, $N_c = 3$, and $N_{SVD} = 8$. From left to right: $j = 1, 2, 3, 4$.

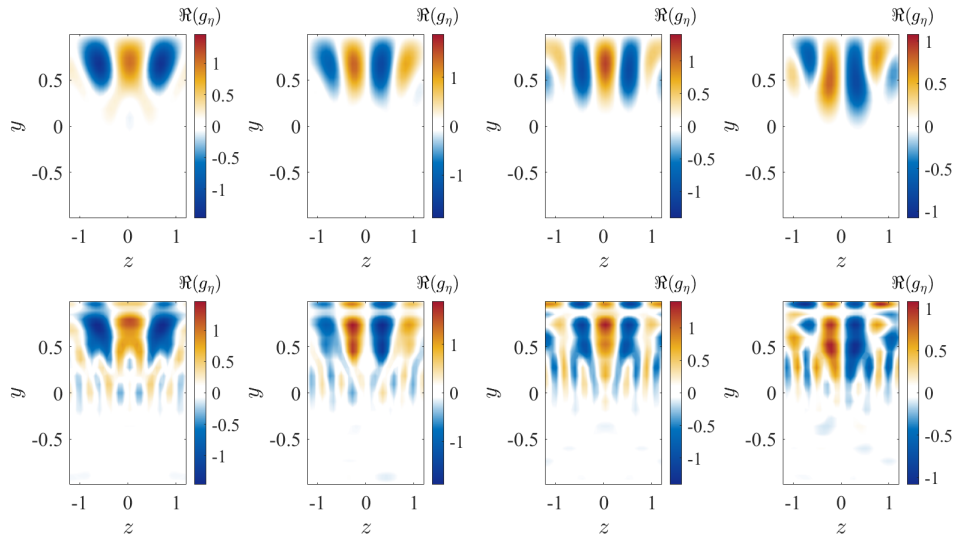

Figure 3.8: Real part of the η component of the first 4 resolvent forcing modes (ϕ_j) for $k_x = 0.5$, $c = 0.75$, and $R = 400$. Top row: true modes, bottom row: VRA model with $N_{k_z} = 11$, $N_c = 3$, and $N_{SVD} = 8$. From left to right: $j = 1, 2, 3, 4$.

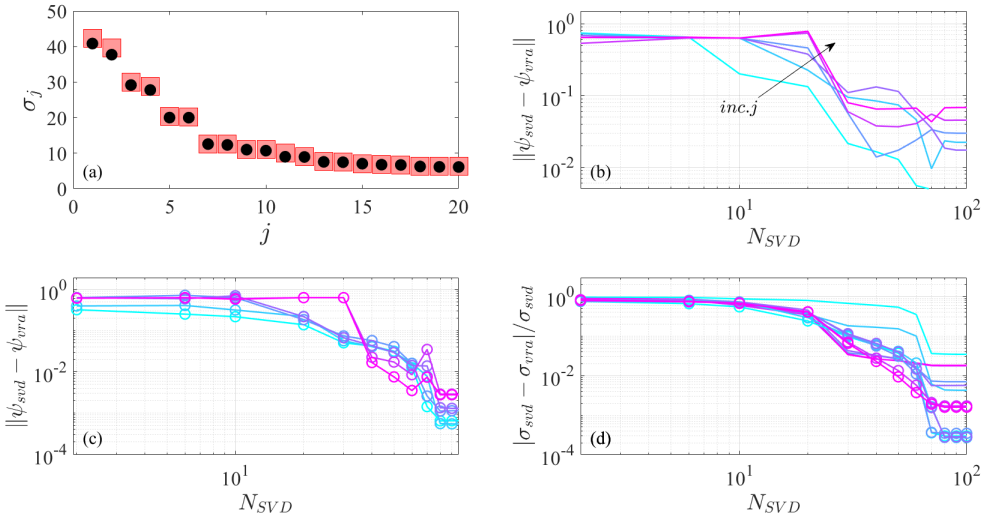

Figure 3.9: Singular values for $k_x = 0.5$, $c = 0.75$, and $R = 400$ (a). SVD reference (red squares) and VRA model(black circles), same model parameters as in Figures 3.5-3.8. Integrated error of variational reconstruction of first six resolvent response modes (b) and (c), plotted separately for clarity, and first six singular values (d) as a function of retained singular basis elements N_{SVD} for $N_c = 1$ and $N_{k_z} = 11$. Results with $c = 0.75$ are plotted in plain lines and those with $c = 0$ are plotted with lines with open circles. From light to dark, colors indicate increasing j from 1 to 6.

3.4 2D Resolvent Analysis: Streamwise Developing Mean Flow

In this section, we use VRA to approximate the resolvent modes for a streamwise developing zero pressure gradient turbulent boundary layer (ZPGTBL). The streamwise developing nature of this flow necessitates large spatial domains and requires nonreflecting boundary conditions at the inlet and outlet of the domain. In this case, the direct computation of the resolvent operator becomes impossible on a personal computer, and the size of the resulting matrices lead to memory requirements which become cumbersome even for high performance computers. Again we choose as our modeling basis 1D resolvent modes, in this case calculated using the mean flow $\bar{U}(y)$ at the inlet of the domain. Thus we have $q_j(x,y) = \psi_j^{1D}(y;k_x,k_z,c)e^{ik_x x}$.

The reference 2D resolvent modes are computed using $\mathbf{L}^{2D}$, the NS operator linearized about the mean flow, $\bar{\mathbf{U}}(x,y)$, under the assumption that the streamwise and wall normal directions are nonhomogenous.[2] The mean flow is interpolated from mean profiles of a ZPGTBL DNS dataset described in Schlatter and Örlü (2010a) with inlet $Re_\tau = u_\tau \delta_{99}/\nu \approx 700$. Variables without superscript are nondimensionalized with the velocity scale U_∞, the free stream velocity, and δ_{99}, the inlet boundary layer thickness, and variables with superscript + denote rescaling with the local friction velocity, $u_\tau(x)$, and local friction lengthscale $\ell(x) = \nu/u_\tau$. The nonhomogeneous directions are discretized using a Chebyshev-Chebyshev grid, with N_y points in $y \in [0, y_{max}]$ and N_x points in $x \in [x_i, x_i + L_x]$, where L_x is the domain length in outer units. Our state $\mathbf{q} = [u, v, w, p]^T$ assumes the following wall normal boundary conditions: $\mathbf{u}(x,0) = \mathbf{0}$, $v_y(x,y) = 0$, and $\mathbf{u}_y(x, y_{max}) = \mathbf{0}$. At the inlet and outlet, we use Dirichlet boundary conditions and extrapolation boundary conditions with an artificial sponge layer applied to damp any artificial reflections due to the boundary conditions Ran et al. (2017, 2019). The discretization was validated with the results from Ran et al. (2017). We note that using finite differences results in sparser operators that would reduce the computation times, but this was not explored in this thesis. The modes are parametrized by the spanwise wavenumber k_z and the temporal frequency, ω. Here we consider three wavenumber-frequency combinations, two inner modes: $[k_z, \omega] = [43.9, 1.8]$ and $[183, 3.6]$, and an outer mode localized in the wake region: $[k_z, \omega] = [11.0, 2.3]$. The latter is used to illustrate the current limitations of the proposed method.

Because the dimension of matrix $\mathbf{L}^{2D}$ is $4N_xN_y \times 4N_xN_y$, the matrix inversion and singular value decomposition are expensive, and scale with $O((4N_xN_y)^3)$. To avoid

[2] The code used to compute these reference modes was developed by Salvador Gomez.

such expensive calculations, an LU decomposition and Arnoldi Method is applied as in Sipp and Marquet (2013) and Schmidt et al. (2018) to compute the SVD of the resolvent by solving linear systems, as opposed to computing the matrix inverse. The most expensive computation, the LU decomposition, is handled with PARDISO, a sparse linear algebra solver which is part of the Intel math kernel library, as in Jeun et al. (2016). Because of the low rank behavior that is often exhibited by the resolvent operator, the Arnoldi Method converges to the singular values and singular vectors in a few iterations. Although this strategy is considerably faster than computing the inverse and taking the SVD, the LU decomposition is still an expensive $O((4N_xN_y)^3)$ operation.

The 1D resolvent modes used as the model basis are all calculated using the inlet mean velocity profile, the same k_z as the 2D modes, a range of N_{k_x} streamwise wavenumbers defined as integer multiples of $2\pi/L_x$, and N_c wavespeeds, c. Although the model basis is computed using knowledge at one streamwise location, the coefficients of the basis are determined using $\mathbf{L}^{2D}$, which includes the streamwise variation of the mean. The multiple wavenumbers allow for constructive and destructive interference, creating the structure seen in the true response mode. Due to the critical layer mechanism, the 1D modes are localized at the critical layer, where $\bar{U}(y) = c$. To cover the wall-normal extent where we expect the 2D mode to be localized we then include a range of N_c linearly spaced wavespeeds. At each wave number triplet $[k_x, k_z, c]$, we also include the leading N_{SVD} resolvent modes, resulting in a total of $r = N_{k_x} \times N_c \times N_{SVD}$ degrees of freedom. The modeling parameters, global mode spatial resolutions, and overall model reduction for the two examples considered here are summarized in Table 3.1. The reader is referred to Figure A.3 in Appendix A.4 for an illustration of some representative basis elements.

Inner Modes

In Figures 3.10 and 3.11, we compare the first four resolvent modes of the variational reconstruction and the modes computed directly through the classic resolvent analysis of the 2D resolvent for $[k_z, \omega] = [43.9, 1.8]$ and $[k_z, \omega] = [183, 3.6]$. The former's spanwise wavelength $\lambda_z^+ \sim 100$ is representative of near wall streaks whereas the latter's spanwise wavelength $\lambda_z^+ \sim 25$ is representative of smaller structure close to the wall (Kline et al., 1967). In both cases, we note that all modes display streamwise oscillations at wavelengths on the order of δ_{99}. Additionally, we also note the presence of a larger wavelength in the form of a modulating envelope with wavelength L_x/j where j is the rank of the mode. In both cases, the character-

istic streamwise wavelength and the modulating envelope of the modes are captured by the VRA model for both the optimal and the higher order modes. We note that this streamwise evolution in both shape and amplitude is not present in the VRA basis functions (see Appendix A.4). Because of this streamwise scale separation, the VRA model requires basis functions with a large range of streamwise wavenumbers. Despite this, the number of retained wave numbers N_{k_x} is still significantly less than the required streamwise spatial discretization, N_x, of the full system.

For the wider (smaller k_z) modes plotted in Figure 3.10, we see that the VRA model predicts the mode shape and amplitude present in the SVD-based modes and replicates many of the general features. Especially in the interior of the domain, the VRA modes capture the reference modes relatively accurately. However, near the streamwise boundaries there are some significant discrepancies. Here, the VRA modes have less support as compared to the reference modes. This difference is likely due to the basis functions not satisfying the same streamwise boundary conditions as the 2D modes. The basis has periodic boundary conditions while the 2D modes are treated with nonreflecting boundary conditions. The nonreflecting boundary conditions, through the sponge, cause the SVD modes to abruptly decay to zero near the inlet and outlet of the domain.

The narrower (larger k_z) modes plotted in Figure 3.11 show relatively good agreement between the VRA prediction and the SVD-based modes throughout the domain. This is likely because in this case the shorter domain restricts the streamwise development of the mean flow, ($700 < Re_\tau < 740$), as opposed to the case of $k_z = 43.9$ where ($700 < Re_\tau < 1040$). Additionally, the narrower modes have less streamwise extent and are localized in the near wall region $y^+ < 35$ where they are less susceptible to streamwise development of the wake (Ruan and Blanquart, 2021). Since the mean flow is nearly parallel in this region, the fact that the 1D resolvent modes used in the VRA model are periodic in x is less of an impediment. However, as seen for example in Figure 3.11c, there is still some discrepancy between the suboptimal SVD and VRA based modes with the VRA mode being slightly shifted towards the inlet relative to the reference mode.

Figure 12 shows all three components of the optimal forcing mode: ϕ_1 for both $k_z = 43.9$ and $k_z = 183$. We plot all three components of the forcing modes to illustrate the component-wise amplification present in non-normal operators. For the response modes, the streamwise component accounts for $> 95\%$ of the total norm of the leading modes investigated here, whereas for the leading forcing modes,

the streamwise components account for less than 5% of the total norm. In wall bounded flows, this discrepancy in the amplification is associated with the lift up mechanism, where disturbances with large spanwise and wall normal components lead to flow responses with large streamwise components. Physically, this is related to the counter rotating vortices that lead to streamwise velocity streaks as recently reviewed by Brandt (2014). In Figure 3.13, we compare the exact singular values and the VRA prediction. Unlike the previous examples we have analyzed, we see that in both cases the VRA model significantly underpredicts the singular values. The error is greater for $k_z = 43.9$ with errors of approximately 33% in σ_1 compared to around 15% for $k_z = 183$.

In this example, the VRA model largely fails to predict the shape of the forcing modes, most notably in the streamwise component of the forcing, and displays significant error in the prediction of the singular values. While the cross-stream components of the VRA approximations capture some of the features seen in the SVD-based forcing modes, the VRA modes exhibit a $\pi/2$ phase shift not seen in the SVD-based mode. Interestingly, the phase shift seems to be centered at different wall normal locations for all three velocity components. We note that despite the differences in the shape, the VRA forcing modes still replicate the component amplitude trends of the SVD-based forcing modes. Again the significant difference in the VRA and SVD-based singular values and forcing modes, despite the similarity in the response modes, illustrates how $\mathbf{H}$ acts as a directional amplifier. The resolvent identifies the most amplified forcing mode, however, $\mathbf{L}$ does not preferentially amplify the leading response. This is discussed in detail in §3.5.

Outer Modes

To illustrate the limits of our method, we consider a wavenumber frequency combination for which the resolvent mode is localized in the wake region of the boundary layer: $[k_z, \omega] = [11.0, 2.3]$. The model parameters, N_{k_x}, N_c, and N_j (summarized in Table 3.1) were chosen such that further increasing the degrees of freedom no longer provided a meaningful speed up over the SVD of the original system. While the range of Re_τ is the same as for the mode with $k_z = 44$, here the global resolvent mode has a much larger wall normal extent and is strongly affected by the streamwise development of the mean flow (Ruan and Blanquart, 2021). Figure 3.14 shows the comparison of the VRA reconstruction of the resolvent response mode and the true reference response mode. As is clear from the figure, the VRA model completely fails to capture the broad support of the true mode in the outer wake

region, and is instead much more localized closer to the wall and further upstream. Despite the lack of agreement between the VRA prediction and the RA mode, the VRA does reasonably predict the streamwise wavelength of the oscillations of this outer scaled mode and the relative amplitudes between u, v, and w (not shown). This example illustrates that for strongly streamwise dependent flows, local, and thus streamwise periodic resolvent modes are inadequate as a modeling basis for even qualitative reconstructions of the global resolvent modes. More generally, if the boundary conditions of the modelling basis differ too much from those of the system being investigated the results of the VRA reconstruction may be inaccurate. Better agreement could potentially be obtained by artificially altering the streamwise variation of the input basis to more closely match the desired result. While such basis optimization is beyond the scope of this thesis, it is a focus of ongoing and future research.

Computational Complexity

Finally, in Table 3.2 we compare the wall time and memory usage of the VRA model to the SVD of the original system for the modes in §3.4. We do not include the outer mode since this case the VRA method failed to even qualitatively replicate the true mode. The computations were all carried out on the Richardson computing cluster at Caltech using the same discretization and mode parameters as summarized in Table 3.1. The direct SVD computations include the inversion and SVD of $\mathbf{L}^{2D}$ using the LU decomposition and Arnoldi method described above. For the VRA model the computation includes the computation of the local resolvent mode basis as well as the construction and spectral decomposition of the variational matrices (3.19). Both methods require the construction of $\mathbf{L}^{2D}$ and thus we do not include it in this comparison. The construction of $\mathbf{L}^{2D}$ takes approximately 90 and 20 seconds for $k_z = 43.9$ and $k_z = 183$, respectively. For both cases, we see a roughly 97% reduction in wall time. The memory savings are significant but less drastic at 42% and 76%, respectively. While the VRA model does not require any inversion, it still requires knowledge of the full size $4N_xN_y \times 4N_xN_y$ matrix $\mathbf{L}^{2D}$ leading to these more modest gains in memory usage. We acknowledge that in this case, the VRA method does not reproduce the SVD modes exactly and so this comparison should be viewed in the context of a trade-off in cost and accuracy. However, considering that the VRA model replicates all the characteristic features of the SVD modes, we believe our method alleviates a significant computational bottleneck in the computation of resolvent modes of non-periodic 2D systems such as the ZPGTBL considered here.

k_z	ω	N_x	N_y	N_{k_x}	N_c	N_{SVD}	c_{min}	c_{max}	$\frac{N_{k_x}N_cN_{SVD}}{4N_xN_y}$
43.9	1.8	192	81	26	3	6	$0.2U_\infty$	$0.65U_\infty$	1/133
183	3.6	96	81	16	3	1	$0.05U_\infty$	$0.25U_\infty$	1/648
11.0	2.3	192	81	32	6	10	$0.6U_\infty$	$0.99U_\infty$	1/33

Table 3.1: Global parameters (k_z, ω), spatial discretization of the full system (N_x, N_y), modeling parameters of the VRA model $(N_{k_x}, N_c, N_{SVD}, c_{min}, c_{max})$, and model reduction from full system to VRA model.

Method	Wall time	RAM used
LU/Arnoldi SVD ($k_z = 43.9$)	72 min	5.98 GB
VRA ($k_z = 43.9$)	2 min	3.47 GB
LU/Arnoldi SVD ($k_z = 183$)	14 min	5.34 GB
VRA ($k_z = 183$)	<1 min	1.26 GB

Table 3.2: Wall time and memory requirements for the LU/Arnoldi-based SVD and the VRA model with the parameters in Table 3.1. The construction of linear operator $\mathbf{L}^{2D}$ is required for both methods and is thus not included in this comparison.

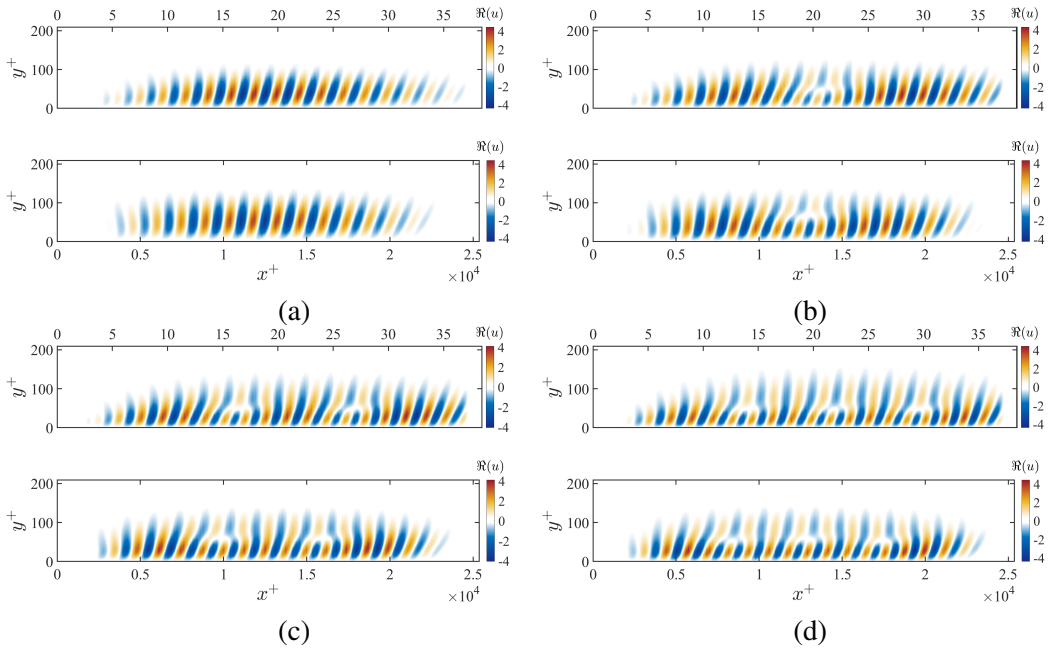

Figure 3.10: First four resolvent response modes (ψ_j): real part of the streamwise component u. $j = 1, 2, 3, 4$ (a - d) for $Re_\tau \approx 700$ and $[k_z, \omega] = [43.9, 1.8]$. Top panels: true global modes, bottom panels: VRA model. Upper x-axis: represents outer units x, lower x-axis represents inner units x^+. Model basis parameters are: $N_{k_x} = 26$, $N_c = 3$, $N_{SVD} = 6$.

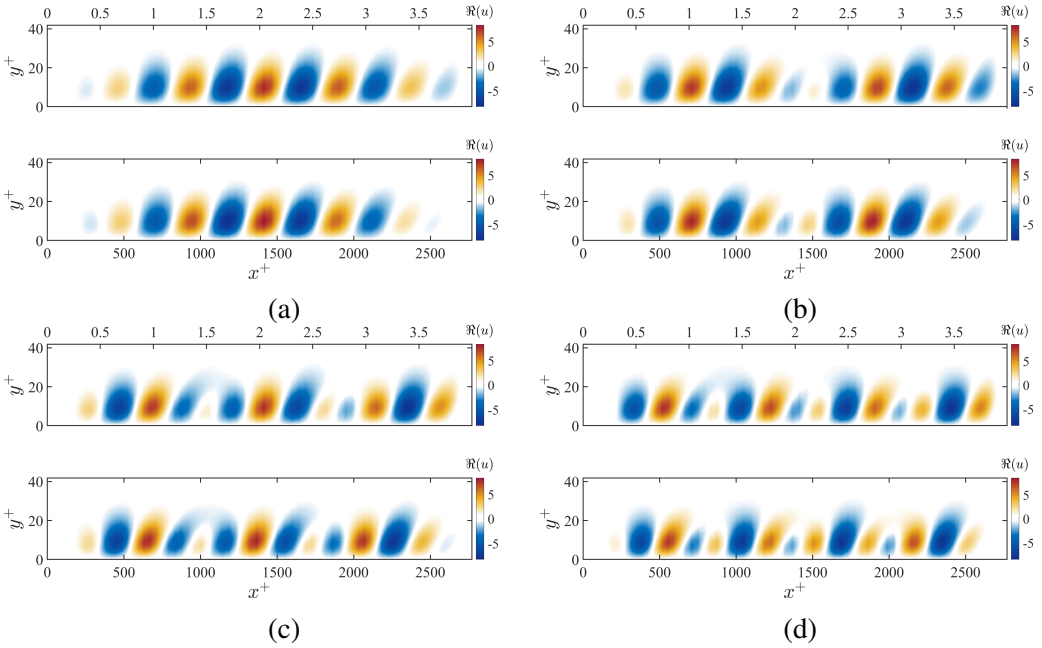

Figure 3.11: First four resolvent response modes (ψ_j): real part of the streamwise component u. $j = 1, 2, 3, 4$ (a - d) $Re_\tau \approx 700$ and $[k_z, \omega] = [183, 3.6]$. Top panels: true global modes, bottom panels: VRA model. Upper x-axis: represents outer units x, lower x-axis represents inner units x^+. Model basis parameters are: $N_{k_x} = 16$, $N_c = 3$, $N_{SVD} = 1$.

3.5 Sensitivity Analysis: The Influence of Rank and Condition Number

In both §3.3 and §3.4, we observed that even when the resolvent response modes, $\boldsymbol{\psi}_j$, were modeled accurately by the VRA method, the singular values, σ_j, and the forcing modes, $\boldsymbol{\phi}_j = \sigma_j \mathbf{L}\boldsymbol{\psi}_j$, may be susceptible to significant error. This is due to the directional amplification of the resolvent operator $\mathbf{H}$ which in the classical CT view of RA minimizes error in the response to errors in the forcing, but in this VRA framework amplifies errors in the predicted forcing due to errors in the response. This phenomenon can be demonstrated using the definition of the SVD (2.5). We note that similar analysis has been performed by Schmid and Brandt (2014), who considered the sensitivity of the eigenvalues and eigenvectors of the linearized NS operator to wide range of types of perturbations.

Consider the action of $\mathbf{H}$ and $\mathbf{L}$ on arbitrary inputs $\tilde{\boldsymbol{\phi}}$ and $\tilde{\boldsymbol{\psi}}$, respectively:

$$\mathbf{H}\tilde{\boldsymbol{\phi}} = \sum_j \sigma_j \boldsymbol{\psi}_j \left\langle \boldsymbol{\phi}_j, \tilde{\boldsymbol{\phi}} \right\rangle \tag{3.73}$$

$$\mathbf{L}\tilde{\boldsymbol{\psi}} = \sum_j \sigma_j^{-1} \boldsymbol{\phi}_j \left\langle \boldsymbol{\psi}_j, \tilde{\boldsymbol{\psi}} \right\rangle . \tag{3.74}$$

where $\tilde{\boldsymbol{\phi}}$ and $\tilde{\boldsymbol{\psi}}$ have unit norm. Suppose we chose $\tilde{\boldsymbol{\phi}} = a\boldsymbol{\phi}_1 + b\mathbf{f}$ and $\tilde{\boldsymbol{\psi}} = a\boldsymbol{\psi}_1 + b\mathbf{q}$ such that $\langle \boldsymbol{\phi}_1, \mathbf{f} \rangle = 0$ and $\langle \boldsymbol{\psi}_1, \mathbf{q} \rangle = 0$ as separate approximations for $\boldsymbol{\phi}_1$ and $\boldsymbol{\psi}_1$, respectively. Equation 3.73 demonstrates that the higher order response modes are weighted by $\sigma_j < \sigma_1$ for $j > 1$, indicating that the component of $\tilde{\boldsymbol{\phi}}_1$ along $\boldsymbol{\phi}_1$ is weighed more heavily than the error $\mathbf{f}$ when approximating the leading response mode. On the contrary, (3.74) demonstrates that the output in the direction of $\boldsymbol{\phi}_1$ is weighted by the smallest singular value of $\mathbf{L}$, σ_1^{-1}, whereas the higher order components are weighted by the larger singular values, σ_j^{-1} with $j > 1$. When using (3.10) to predict $\boldsymbol{\phi}_1$ based on an approximation of $\boldsymbol{\psi}_1$, this projection of the error onto higher order modes corrupts the prediction by weighing the output onto higher order forcing modes.

The differences between the error in approximating the gain in $\mathbf{H}$ and $\mathbf{L}$ can be quantified through a perturbation analysis of the singular values. The singular values are related to the resolvent response and forcing modes by

$$\sigma_j^2 = \left(\mathbf{H}\boldsymbol{\phi}_j\right)^H \mathbf{Q} \left(\mathbf{H}\boldsymbol{\phi}_j\right) = \left(\left(\mathbf{L}\boldsymbol{\psi}_j\right)^H \mathbf{Q} \left(\mathbf{L}\boldsymbol{\psi}_j\right) \right)^{-1} . \tag{3.75}$$

We consider the sensitivity of σ_j to perturbation in either the resolvent forcing or response modes: $\boldsymbol{\psi}_{j,\epsilon} = \boldsymbol{\psi}_j + \epsilon\mathbf{r}$ and $\boldsymbol{\phi}_{j,\epsilon} = \boldsymbol{\phi}_j + \epsilon\mathbf{g}$, where $\epsilon \ll 1$ and $||\boldsymbol{\psi}_j|| =$

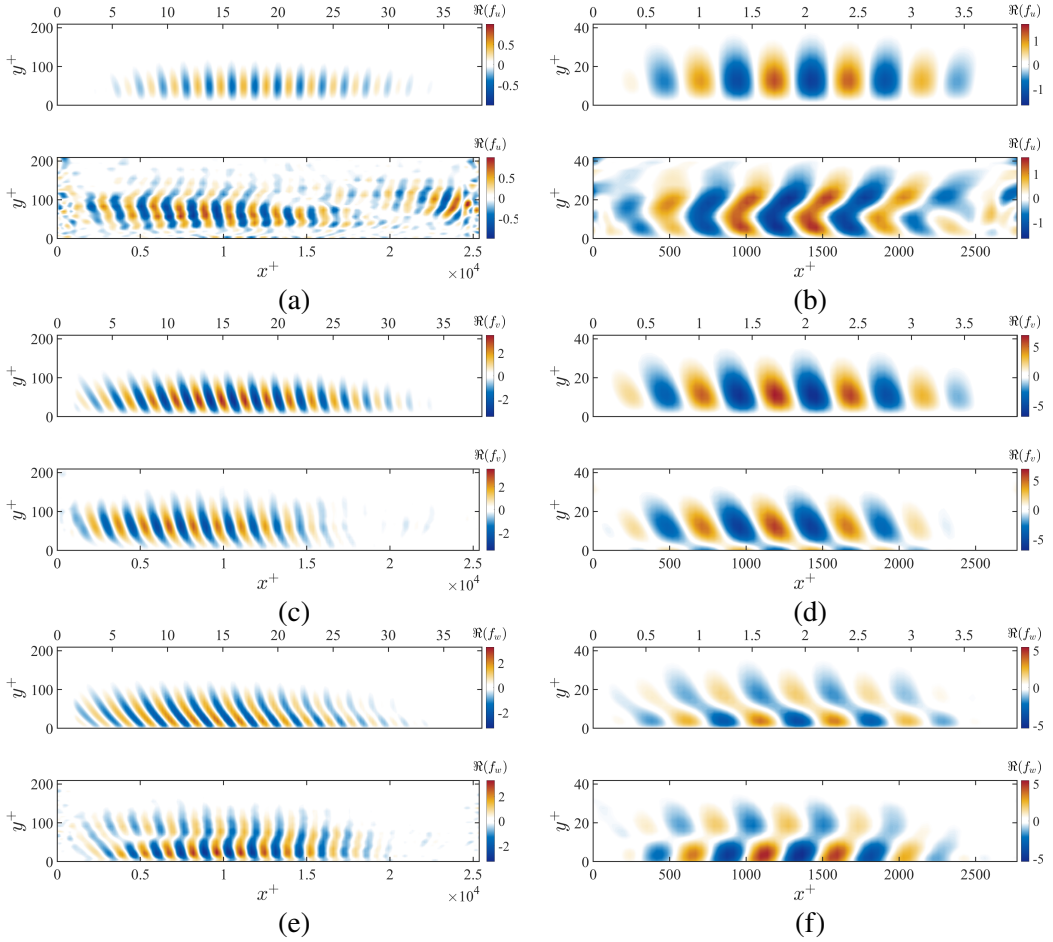

Figure 3.12: Leading resolvent forcing mode (ϕ_1) for $Re_\tau \approx 700$. $[k_z, \omega] = [43.9, 1.8]$, f_u(a), f_v(c), f_w(e). $[k_z, \omega] = [183, 3.6]$, f_u(b), f_v(d), f_w(f). In each subplot, top panels: true global modes, bottom panels: VRA model.Upper x-axis: represents outer units x, lower x-axis represents inner units x^+. Model basis parameters are the same as in Table 3.1.

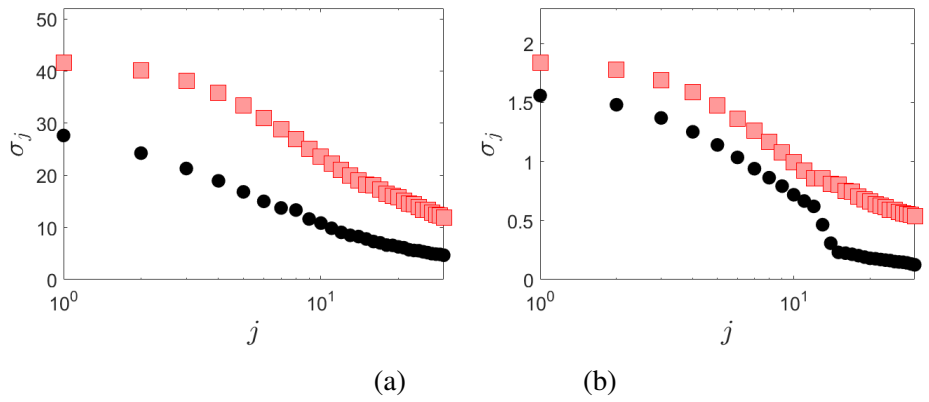

Figure 3.13: Singular values from the direct SVD (red squares) and variational reconstruction (black circles) at $Re_\tau \approx 700$. $[k_z, \omega] = [43.9, 1.8]$ (a), $[k_z, \omega] = [183, 3.6]$ (b).

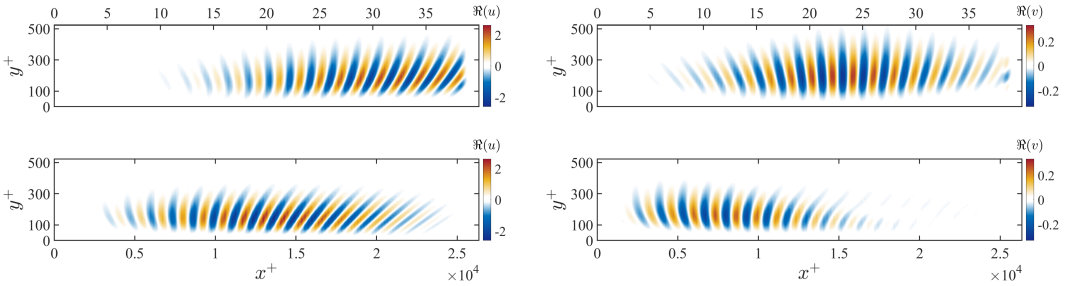

(a) (b)

Figure 3.14: Real part of optimal resolvent response mode (ψ_1) for $[k_z, \omega] = [11.0, 2.3]$: u (a) and v (b). Top panels: true global modes, bottom panels: VRA model. Upper x-axis: represents outer units x, lower x-axis represents inner units x^+.

$||\phi_j|| = ||\mathbf{r}|| = ||\mathbf{g}|| = 1$. We define the perturbed singular value: $\sigma_{j,\epsilon,L} \equiv \sigma_j\left(\psi_{j,\epsilon}\right)$ and $\sigma_{j,\epsilon,H} \equiv \sigma_j\left(\phi_{j,\epsilon}\right)$. We may then derive the bounds on the error induced by the ϵ small perturbation in the singular modes:

$$\frac{|\sigma_{j,\epsilon,L} - \sigma_j|}{\sigma_j} \leq \epsilon\sigma_j||\mathbf{L}|| \tag{3.76}$$

$$\frac{|\sigma_{j,\epsilon,H} - \sigma_j|}{\sigma_j} \leq \epsilon\frac{\sigma_1}{\sigma_j}. \tag{3.77}$$

The details of the derivation are included in Appendix A.5. We can perform a similar analysis to investigate the sensitivity of the predicted forcing modes to perturbations in the response modes and vice versa.

$$\phi_{j,\epsilon,\psi} \equiv \sigma_{j,\epsilon,L}\mathbf{L}\left(\psi_j + \epsilon\mathbf{r}\right) \tag{3.78}$$

$$\psi_{j,\epsilon,\phi} \equiv \sigma_{j,\epsilon,H}\mathbf{H}\left(\phi_j + \epsilon\mathbf{g}\right) \tag{3.79}$$

Here the $\sigma_{j,\epsilon,L}$ and $\sigma_{j,\epsilon,H}$ are the same as defined above. The error in the resolvent modes may be bounded as follows

$$\|\phi_{j,\epsilon,\psi} - \phi_j\| \leq \epsilon\left(\sigma_j\|\mathbf{L}\| + 1\right)\sigma_j\|\mathbf{L}\| \tag{3.80}$$

$$\|\psi_{j,\epsilon,\phi} - \psi_j\| \leq \epsilon\left(\frac{\sigma_1}{\sigma_j} + 1\right)\frac{\sigma_1}{\sigma_j} \tag{3.81}$$

where again we relegate the details to Appendix A.6. These results imply that as long as σ_j/σ_1 is not too large an $O(\epsilon)$ perturbation to ϕ leads to an error of $O(\epsilon)$ in σ and ϕ; however, an $O(\epsilon)$ perturbation in ψ leads to an error in σ and ϕ that is expected to be larger by a factor of $\sigma_j\|\mathbf{L}\|$. To analyze how large the factor

is expected to be, we follow the analysis of Symon et al. (2018) and consider the spectral decomposition of $\mathbf{L} = \mathbf{V}\mathbf{\Lambda}\mathbf{V}^{-1}$ which allows us to rewrite (3.76) as

$$\frac{|\sigma_{j,\epsilon,L} - \sigma_j|}{\sigma_j} \leq \epsilon\kappa\frac{\sigma_j}{\sigma_{min}} \leq \epsilon\kappa\frac{\sigma_1}{\sigma_{min}} \tag{3.82}$$

where

$$\sigma_{min} \equiv \min_{\sigma_j \in \mathbf{\Sigma H}} \sigma_j = \left(\max_{\lambda_j \in \mathbf{\Lambda}(\mathbf{L})} (\lambda_j)\right)^{-1} \tag{3.83}$$

is the minimum singular value of the resolvent and $\kappa \equiv \|\mathbf{V}\|\|\mathbf{V}^{-1}\|$ is the condition number. The latter is always greater than one and quantifies the non-orthogonality of the eigenvectors, and thus the non-normality of the operator. This non-normality leads to the phenomenon of pseudo-resonance, where small perturbations to the operator lead to large perturbations to the eigenvalues (Trefethen and Embree, 2005). Thus, there are two mechanisms which lead to an increased sensitivity of singular values and forcing modes to perturbations in the response modes. First, the relative resonant amplification of the mode quantified by σ_j/σ_{min}, and second, the pseudo-resonant amplification of the linear dynamics quantified by κ.

Perturbation Analysis of a Simplified Example

To illustrate the effects of resonant and pseudo-resonant amplification on the error in singular values and singular modes, we compute $|\sigma_{1,\epsilon,L} - \sigma_1|$, $|\sigma_{1,\epsilon,H} - \sigma_1|$, $|\phi_{1,\epsilon,L} - \phi_1|$, and $|\psi_{1,\epsilon,H} - \psi_1|$ for the model operator

$$\mathbf{L} = \begin{bmatrix} a & c \\ 0 & b \end{bmatrix} \tag{3.84}$$

for a range of ϵ. To test the resonant amplification, we compare the error in singular values for normal operators $\mathbf{L}$ with the parameters set to $[a, b, c] = [1, 1.5, 0]$ and $[a, b, c] = [1, 50, 0]$. To test the pseudo-resonant effects, we introduce and vary the off-diagonal term c that makes $\mathbf{L}$ non-normal. We compare $[a, b, c] = [1, 1.5, 0.1]$ and $[a, b, c] = [1, 1.5, 5]$. In each case, we set the perturbation vectors $\mathbf{r}$ and $\mathbf{g}$ to be orthogonal to ψ_1 and ϕ_1, respectively. The error in singular values is plotted in the top row of Figure 3.15 and the error in the singular modes is plotted in the bottom row of Figure 3.15. These plots reveal that, as expected, the error grows with ϵ, but, when the resonant or pseudo-resonant effects are increased, the error due to a perturbation in $\boldsymbol{\psi}$ is greater by several orders of magnitude than the error due to perturbations in $\boldsymbol{\phi}$. The error in singular modes is proportional to ϵ as predicted by the derived error bounds, while for small ϵ the error in singular values actually

grows as ϵ^2. This is due to the fact that for this toy problem the perturbation is chosen to be orthogonal to the singular vectors which causes the $O(\epsilon^2)$ contribution to dominate.

Implications and Limitations

This analysis illustrates an inherent drawback of the proposed VRA-based method. The benefits of circumventing the inversion of the linear dynamics come at the cost of losing the directional amplification of the resolvent operator. Since $\mathbf{H} = \mathbf{L}^{-1}$, the largest singular values of $\mathbf{H}$ correspond to the smallest singular values of $\mathbf{L}$ and vice versa. Thus, the action of $\mathbf{L}$ on the response modes, as in (3.10), amplifies the higher order forcing modes. Furthermore, the greater the singular value separation of $\mathbf{H}$, the more difficult it becomes for spectral decomposition algorithms to disambiguate the desired modes from numerical artifacts and other spurious modes. This marks a difference between VRA and RA algorithms that approximate the SVD with matrix sketching where the convergence is improved when $\mathbf{H}$ is low rank (Ribeiro et al., 2020). From a practical point of view these issues are compounded by the fact that it is difficult to accurately compute the smallest eigenvalues of a matrix. Even if the order reduction $r/n \ll 1$ is significant, the reduced matrix of size $r \times r$ may still be

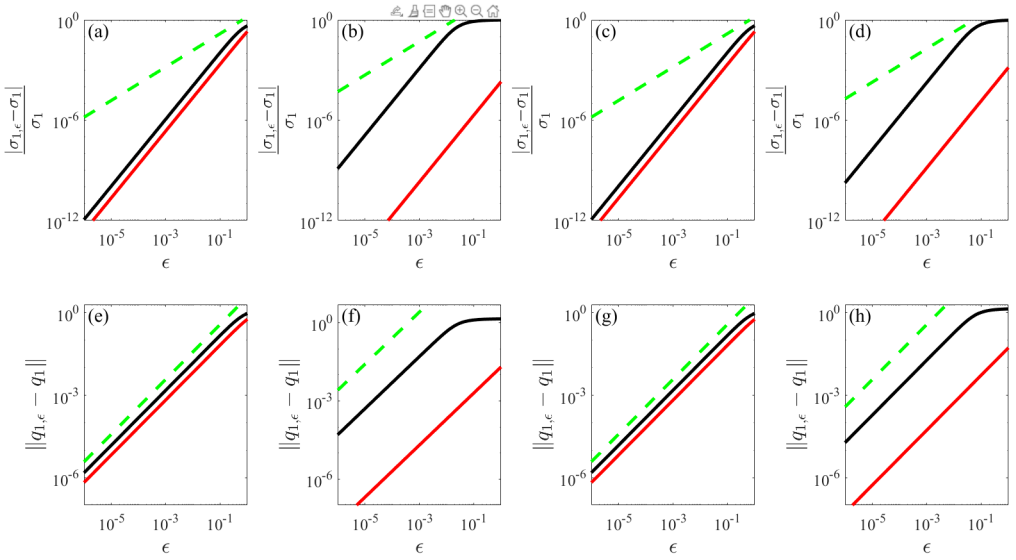

Figure 3.15: Top row: relative error in singular value, normal($c = 0$): $b/a = 1.5$ (a), $b/a = 50$ (b), non-normal: $c/a = 0.1$ (c), $c/a = 5$ (d). Bottom row: relative error in singular modes, normal($c = 0$): $b/a = 1.5$ (e), $b/a = 50$ (f), non-normal: $c/a = 0.1$ (g), $c/a = 5$ (h). Color code: error due to perturbation to ψ (solid black), error due to perturbation to ϕ (solid red), and derived upper bound (dashed green).

sufficiently large such numerical issues may be a limiting factor. However, the focus of this thesis is the theoretical framework, and not the optimization of the numerical algorithms involved, and thus a detailed analysis of the numerical error is beyond the scope of this work.

Furthermore, since our method relies on multiplication by the generally non-normal linear operator $\mathbf{L}$ to recover the forcing modes through (3.10), the VRA approximation of these forcing modes is susceptible to errors if $\kappa(\mathbf{L})$ is large. Although we note that since the matrices in (3.19) are normal, the VRA-based estimation of the resolvent response modes is robust to the non-normality of the linear dynamics.

Another factor leading to the increased error in the singular values and forcing modes we have observed is that the continuous linear differential operators being analyzed have unbounded spectra. Therefore, the maximum eigenvalue of the discretized operator $\mathbf{L} \in \mathbb{C}^{n\times n}$ grows with its size n. In particular, we expect the maximum eigenvalue of second order differential equations like the ones considered here to scale with n^2. However, depending on the numerical discretization used, the largest eigenvalues may be spurious, as in the case of Chebyshev differentiation matrices, where the largest eigenvalue scales with n^4 for these second order differential equations (Trefethen, 2000). This implies that the VRA reconstruction of the singular values and forcing modes becomes increasingly sensitive to errors in the response modes as the number of basis elements grows.

These are noteworthy limitations of our proposed method since the cost saving potential of the proposed method is greatest for larger systems and, in many flows of interest, the resolvent operator is, in fact, low rank. Nonetheless, in most cases the aim of equation-driven modal analysis techniques such as resolvent analysis is to identify coherent structures or obtain an efficient modeling basis (Rosenberg and McKeon, 2019b; Nogueira et al., 2019; Barthel et al., 2021). In these cases, the resolvent response modes, which our method can predict independent of condition number or singular value separation, are of primary interest. In the resolvent formulation of the nonlinear NSE, the forcing modes arise through their projection onto the nonlinear interaction of the response modes: $\langle \phi, \psi \cdot \nabla \psi \rangle$ (McKeon, 2017; Barthel et al., 2021). As discussed in §3.5, the error in the forcing modes arises due to higher order ($j \gg 1$) response modes with very small σ_j being amplified through the action of $\mathbf{L}$. However, since these higher order modes are not expected to be dynamically relevant (Morra et al., 2021), especially if the resolvent is low rank, they generally will not have significant projection onto the actual nonlinear interaction

of the response. This may, in some cases, ameliorate the practical implications of the error in forcing modes since even if there is significant error in ϕ, the error in the relevant metric, $\langle \phi, \psi \cdot \nabla \psi \rangle$, is expected to be small.

3.6 Discussion

The examples presented in this chapter illustrate the avenues of progress enabled by the VRA formulation of resolvent analysis. First, circumventing the inversion of the linear operator in the definition of the resolvent modes allows for analytical manipulation. This facilitates the derivation of scaling laws and parametric dependencies as we have done in §3.2. Second, from a numerical point of view, the VRA method avoids the calculation of a matrix inverse and applying expensive linear algebra decompositions to the matrices. Figure 3.16 outlines the matrix operations and computational complexity of the VRA method presented herein and the direct SVD. For a matrix of dimension $n \times n$, calculating the inverse, performing an LU decomposition, and applying an SVD are each $O(n^3)$ operations. The resolvent matrix, calculated as the inverse of a matrix, is in general, a dense matrix which leads to large memory costs in terms of storage. Even avoiding the inverse by applying the LU decomposition as explained in §3.4 would require storage of large dense triangular matrices. Typically when the Linearized NS (LNS) operator is discretized, the resulting matrix is sparse. Sparse matrices have the advantage that only their nonzero elements are stored and sparse matrix operations can be computed more efficiently. Even though the discretizations described herein use spectral methods, the discretized LNS operator described in §3.4, $\mathbf{L}^{2D}$, boasts sparsity of less than 1%. In the VRA method, the sparse discretized LNS operators are only used for matrix multiplication with the basis to create the $r \times r$ matrices $\mathbf{M}$ and $\mathbf{Q}$ for the eigenvalue problem in (3.19). Since the analytical form of the LNS operator is known, the matrix multiplications can be avoided altogether if the basis is defined with analytic functions, as demonstrated in §3.2. Although the resulting matrices $\mathbf{M}$ and $\mathbf{Q}$ are dense, the eigenvalue problem can be solved almost trivially with standard methods as it scaled with $O(r^3)$ where $r \ll n$. Even if the number of basis elements, r, becomes large, the eigenvalue problem could be solved with approximate methods like the Arnoldi Algorithm with the Shift and Invert method.

We acknowledge that the the computational cost comparison we have made may not reflect the exact speed up enabled by our method, since these sparsity promoting strategies could of course also be applied to the SVD based techniques. Utilizing the shift and Invert method for example can lead to operation counts which are of order

$n^{1.5}$, or n^2 rather than the n^3 of more straightforward approaches. One example of a direct method for the computation of global resolvent modes is the one way Navier Stokes equations (OWNS) proposed by Towne et al. (2021) which addresses the computation of resolvent modes for slowly varying base flows such as the ZPGTBL considered here. The OWNS framework splits the action of the linear operator into upstream- and downstream-traveling components and is thus of particular use in compressible flows, which are beyond the scope of this work. This thesis is primarily concerned with the fundamental variational framework of resolvent analysis. We view the VRA based computation of global modes described here as simply one potential application of this framework, and therefore the algorithmic optimization thereof is beyond the scope of this thesis.

As discussed in §3.5, the VRA method is prone to error in predicting the singular values and forcing modes when there is strong non-normality or the operator is very low rank. In this sense, the herein proposed VRA method provides a natural compliment to the recently developed randomized resolvent analysis method proposed by Ribeiro et al. (2020), which is particularly effective when the resolvent is low rank. However, we reiterate that response modes can be modeled accurately regardless of these properties and at a fraction of the cost of a direct SVD. Furthermore, it is these response modes that are generally of primary interest. They have been shown to be an efficient basis for a variety of flows including turbulent jets (Schmidt et al., 2018; Pickering et al., 2021), boundary layers (Sipp and Marquet, 2013; Rigas et al., 2021), exact coherent states, (Sharma et al., 2016; Rosenberg and McKeon, 2019b) and others. Notably, Sharma et al. (2016) showed that using five response modes per Fourier mode for the N3L lower branch solution in a pipe, fluctuations were reconstructed retaining 98% of the fluctuation energy. Using only one response mode per Fourier mode, they were able to reconstruct 95% of the fluctuation energy. Towne et al. (2018) also studied the similarities between RA and SPOD. They found that the response modes and the data driven SPOD modes are equivalent when there is uncorrelated, white-noise forcing. This implies that in certain conditions RA could be used as a predictive tool to model near wall structures in the simulation of high Reynolds number wall bounded flows, where large numerical resolution is needed to resolve the near wall structures. Furthermore, since the proposed method is derived directly from the definition of the forced linear system, the method is not fundamentally limited to linear systems or a certain type of input basis.

The primary limitation is that the spatial support of the input basis needs to overlap

with the spatial support of the resolvent modes being estimated. In particular we saw in §3.4 that a sufficiently strong mismatch between the boundary conditions of the input basis and the linear operator can lead to significant errors in the VRA reconstruction. In general, a critical layer mechanism (as in §3.3) or scaling laws (as in §3.4) dictate the spatial localization and length scale of resolvent modes and thus one can reliably predict this region of support a priori. However, for flows where the general region of spatial support can not be predicted, a larger input basis with a broader range of wave numbers and spatial support may be necessary. We found the most important parameter is the number of retained spatial wavenumbers, N_{k_z} or N_{k_x}, and if the largest relevant wavenumber is not known a priori it may be necessary to progressively increase these parameters until convergence is obtained. Additionally, unlike some recent equation-free methods such as Herrmann et al. (2021), our method relies on knowledge of the linearized dynamics of the system, which in some cases may not be known a priori. In this regard the primary challenge is generally lack of knowledge of the mean flow. However, recently several authors have developed methods to efficiently estimate the mean dynamics for a range of flows (Mantič-Lugo et al., 2014, 2015; Rosenberg and McKeon, 2019a). Such techniques could be combined with the method presented in this chapter to efficiently compute resolvent modes in situations were the mean dynamics are unknown, or would be costly to compute directly, although this is beyond the scope of this thesis.

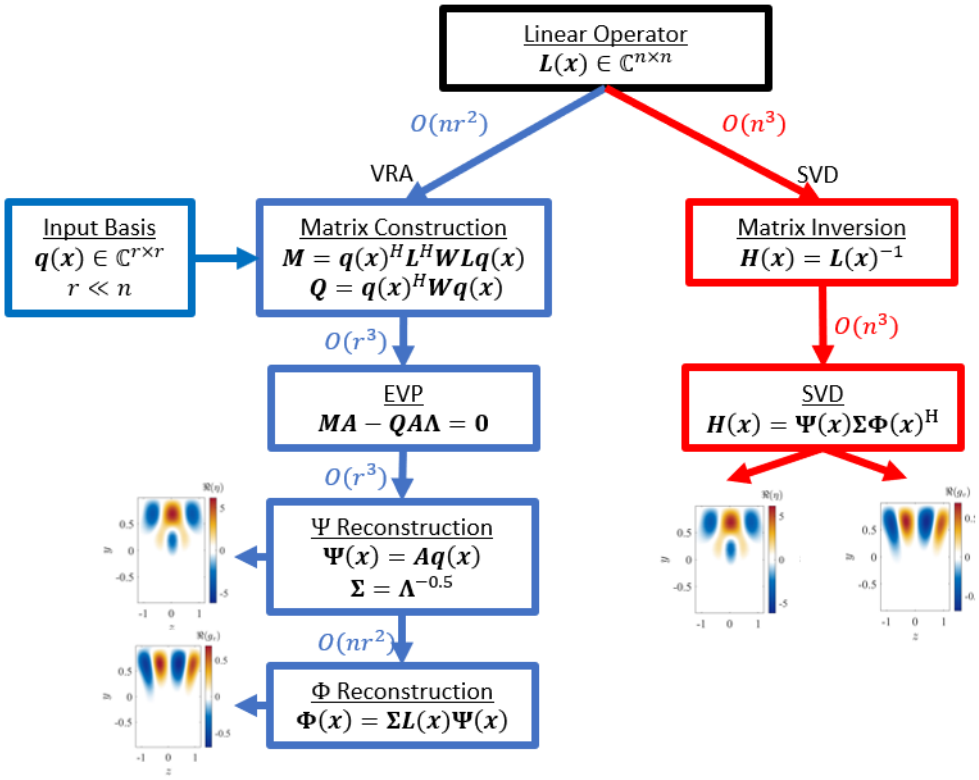

Figure 3.16: Comparison of the matrix operations and computational complexity involved in the VRA and SVD-based computations of resolvent modes. VRA operations are shown in blue, SVD operations are shown in red.

3.7 Summary

In this chapter, we have suggested an alternative conceptual framework based on the calculus of variations from which to view resolvent analysis. In this variational framework, the resolvent response modes are defined as the stationary points of an operator norm subject to a relevant norm constraint. We proved that this variational formulation is equivalent to the standard SVD-based definition, and introduced a method to estimate the resolvent modes of complex systems as expansions in lower dimensional basis functions. This formulation is a contrast to the traditional control theory inspired framework. The crucial advantage of this formulation and the method presented herein is the lack of reliance on the inversion of the linear operator, which from a theoretical point of view allows for easier analytical manipulation, and from a practical point of view, enables drastic model reduction and leads to a significant reduction in computational complexity.

The analytical advantages were illustrated on the example of streamwise constant structures in a turbulent channel flow, where we derived a closed form solution

to the Euler-Lagrange equations governing the optimal resolvent mode. Resolvent modes have shown to encode physically relevant features of turbulence (McKeon, 2017), and therefore we believe the improved analytical tractability of the variational formulation will open the door to the further understanding and discovery of the underlying physics.

The numerical advantages were illustrated first for both a 2D/3C equilibrium solution in plane Couette flow and a streamwise developing turbulent boundary layer. In the first example, we showed that if the model basis satisfies the same boundary conditions as the full system, the VRA model converges to the true modes as more basis are included in the VRA model. In the second case, we showed that even if the basis does not satisfy the correct boundary conditions, and the streamwise development of the mean flow is not too strong, the VRA model is able to reproduce the characteristic features of the SVD-based modes with a reduction of order of over two orders of magnitude resulting in an order of magnitude reduction in computation time and a $40-75\%$ reduction in RAM usage. As formulated here, the current method fails for flows with very strong streamwise development. In such cases, a more carefully chosen modeling basis, which already encodes some of the anticipated streamwise development, is likely needed for our method to be viable. This is a focus of ongoing research.

For the examples considered here the proposed method accurately modeled the resolvent response modes, however we observe significant error in the reconstruction of the forcing modes. We performed a sensitivity analysis and demonstrated that the error in the VRA estimate of the forcing modes is due to the directional amplification of the resolvent and is enhanced in situations were the resolvent operator is very low rank or highly non-normal. Nonetheless, we believe that this conceptual approach to resolvent analysis can open the door for further analysis of the NSE and the discovery of new physics, as well as enabling the real time computation of resolvent modes in applications such as experiments and simulations where the cost of the standard SVD-based approach is prohibitive.

Chapter 4

NONLINEAR MODELING OF TAYLOR VORTEX FLOW

4.1 Introduction

This chapter addresses the nonlinear aspects of resolvent modeling.[1] Here the resolvent basis is assumed to be known a priori, computed either through a direct SVD, or through other means, such as the VRA algorithm discussed in chapter 3. This chapter focuses on approximating solutions to the nonlinear interaction coefficient Equation (2.17) defined in Chapter 2. As a test case, we seek a flow configuration which gives rise to stable nonlinear (non-laminar) yet relatively low dimensional solutions. Lower dimensional (non-turbulent) solutions allow us to study the nonlinear dynamics in a systematic manner at relatively low computational cost. One such configuration is Taylor-Couette flow (TCF), the flow between two concentric and independently rotating cylinders.

Taylor-Couette flow is one of the canonical problems in fluid mechanics, and a paradigm for the study of linear stability, pattern formation, and rotationally driven turbulence. From the original investigations of Taylor (1923) to the pioneering experiments of Coles (1965), recent theoretical analyses (Gebhardt and Grossmann, 1993; Jones, 1981; Maretzke et al., 2014), high Reynolds number simulations (Ostilla et al., 2013; Ostilla-Mónico et al., 2014a; Grossmann et al., 2016; Sacco et al., 2019), and experimental investigation (van Gils et al., 2011; Huisman et al., 2014; van Gils et al., 2012), TCF has remained a problem of interest for most of the last century. Perhaps the most well-known characteristic of TCF is the incredibly rich array of stable flow states that exist over a range of geometries and relative rotation rates of the inner and outer cylinders (Coles, 1965; Andereck et al., 1986). We consider the case of pure inner cylinder rotation, for which the problem is parameterized by the ratio of the inner and outer radii, $\eta \equiv r_i/r_o$, and a single Reynolds number: R. In this case the laminar velocity profile becomes linearly unstable at a critical Reynolds number: $R_c \sim O(10^2)$. A centrifugal instability leads to the formation of a periodic array of toroidal vortex structures known as Taylor vortices or Taylor rolls. For a given geometry, these steady, axisymmetric Taylor vortices are stable and exist for some range of Reynolds number in what is known as the Taylor vortex flow (TVF)

[1] The contents of this chapter have been published in the *Journal of Fluid Mechanics*, 924:A9.

regime. As the rotation rate of the inner cylinder is increased further, the Taylor vortices experience a secondary instability giving rise to azimuthally traveling waves whose phase speed is determined by the geometry but whose azimuthal periodicity is not unique (Coles, 1965). This regime is known as wavy vortex flow (WVF) and is characterized by being time periodic in a stationary reference frame but steady in a frame corotating with the traveling wave (Marcus, 1984). WVF is again stable for some range of Reynolds numbers before the traveling waves themselves become unstable, and a second temporal frequency arises causing the traveling waves to become modulated in space and time in what is known as modulated wavy vortex flow (MWVF). As the driving of the inner cylinder is increased further still, the flow becomes disordered and begins to transition to turbulence. However, while the main sequence of transitions from laminar flow to the bifurcation to TVF at $R_c \approx 100$, to WVF, to MWVF, and finally on to turbulence at $R \approx 1000$ occurs over a relatively narrow range of Reynolds numbers, the large scale Taylor vortices are present up to $R \sim O(10^5)$ (Grossmann et al., 2016).

In recent years, there has been renewed interest (Dessup et al., 2018; Sacco et al., 2019) in the dynamics of TVF and WVF as a model system to study the self-sustaining process (SSP) proposed by Waleffe (1997). The SSP consists of streamwise rolls which advect the mean shear giving rise to streaks of streamwise velocity, which become unstable to wave-like disturbances, which in turn nonlinearly interact to sustain the rolls (Waleffe, 1997; Hamilton et al., 1995). Dessup et al. (2018) performed direct numerical simulations (DNS) to show that the mechanism of transition from TVF to WVF follows the same path as described in the SSP: the traveling waves of WVF arise due to an instability of the streamwise velocity component (streaks) of TVF with the cross-stream velocity (rolls) playing a negligible role in the instability mechanism. Sacco et al. (2019) extended this line of study to higher Reynolds numbers and showed that despite their origin as a centrifugal instability, turbulent Taylor vortices are preserved in the limit of vanishing curvature and are thus not dependent on rotational effects, but rather are sustained through a nonlinear feedback loop between the rolls and streaks.

The SSP is believed to be one of the building blocks of turbulence and thus the study of self sustaining solutions of the Navier-Stokes equations (NSE), known as *exact coherent states* (ECS) has been of great interest to researchers since they were first discovered by Nagata (1990). The field has grown immensely since in the intervening years and we make no attempt to summarize it all here. Of primary interest is the

observation that many of these solutions resemble streamwise elongated vortices and streaks, and thus resemble structures observed in experiments and simulations of turbulent flows (Beaume et al., 2015). This has led to the idea that ECS make up the phase space skeleton of turbulence, and that the observation of these structures indicates the turbulent trajectory passing by one of these ECS solutions.

Due to the significant mathematical simplification, it is useful to model these elongated structures as being infinitely long in their streamwise extent. Illingworth (2020) studied the linear amplification mechanism of such streamwise invariant structures to identify the most amplified spanwise length scales in both channel and plane Couette flow (PCF), and found that the latter was far more efficient in amplifying these structures. However, no structures actually observed in channel or plane Couette flow are truly invariant in the streamwise direction. Additionally, ECS are generally unstable; while the turbulent trajectory may visit these states, they do not actually persist in nature. TVF is thus a valuable test case to study the nonlinear dynamics sustaining ECS in general since it is in fact a stable solution observed in experiment and due to the cylindrical geometry is exactly streamwise constant.

In this chapter, we use optimization-based methods to explicitly model the self-sustaining nonlinear system. This helps us bridge the gap between linear stability theory, which accurately predicts the genesis of Taylor vortices, and higher Reynolds numbers where Taylor vortices are sustained by fully nonlinear mechanisms as shown by Sacco et al. (2019).

4.2 Mathematical Description

In Chapter 3, we considered a variety of flow configurations and geometries, with the focus of deriving the resolvent modes of general linear operators. Here we focus specifically on the flow of an incompressible Newtonian fluid with kinematic viscosity ν between two concentric cylinders. Such a flow is governed by the NSE in cylindrical coordinates,

$$\frac{\partial \tilde{\boldsymbol{u}}}{\partial t} + \tilde{\boldsymbol{u}} \cdot \nabla \tilde{\boldsymbol{u}} - \frac{1}{R}\nabla^2 \tilde{\boldsymbol{u}} - \nabla \tilde{p} = 0 \tag{4.1}$$

$$\nabla \cdot \tilde{\boldsymbol{u}} = 0 \tag{4.2}$$

on the domain $r \in [r_i, r_o]$, $\theta \in [0, 2\pi]$, $z \in [-L_z/2, L_z/2]$. We will consider the case where the outer cylinder is held fixed while the inner cylinder rotates with a prescribed azimuthal speed U_i. The equations are nondimensionalized using the gap width $d \equiv r_o - r_i$ and the azimuthal velocity of the inner cylinder U_i. The Reynolds

number is defined as $R \equiv U_i d/\nu$. In these nondimensional variables the limits of the radial domain are given as a function of the radius ratio η by $r_i = \eta/(1-\eta)$ and $r_o = 1/(1-\eta)$. Throughout this chapter we fix $\eta = 0.714$, for which the critical Reynolds number $R_c = 81$. This η was chosen to allow for comparison to past studies such as Ostilla et al. (2013) and since it allows for a larger range of Reynolds numbers for which TVF is a stable solution of (4.1).

We decompose the state $[\tilde{\mathbf{u}}, \tilde{p}] = [\tilde{u}_r, \tilde{u}_\theta, \tilde{u}_z, p]$ into a mean and fluctuating component,

$$[\tilde{\mathbf{u}}(r,z,\theta,t), \tilde{p}(r,z,\theta,t)] = [\overline{\mathbf{U}}(r), \overline{P}(r)] + [\mathbf{u}(r,z,\theta,t), p(r,z,\theta,t)] \tag{4.3}$$

with

$$\overline{(\cdot)} \equiv \lim_{T,L\to\infty} \frac{1}{2\pi TL} \int_0^T \int_0^{2\pi} \int_0^L (\cdot)\, dz\, d\theta\, dt, \tag{4.4}$$

which, upon substitution into (4.1) and averaging over z, θ, and t, results in the mean momentum equation

$$\overline{\mathbf{U}} \cdot \nabla \overline{\mathbf{U}} - \frac{1}{R}\nabla^2 \overline{\mathbf{U}} - \nabla \overline{P} = -\overline{\mathbf{u} \cdot \nabla \mathbf{u}} \tag{4.5}$$

$$\nabla \cdot \overline{\mathbf{U}} = 0. \tag{4.6}$$

Subtracting (4.5) from the full NSE then results in a governing equation for the fluctuations, where we have grouped those terms which are nonlinear in the fluctuations on the right hand side in anticipation of the following analysis.

$$\frac{\partial \mathbf{u}}{\partial t} + \overline{\mathbf{U}} \cdot \nabla \mathbf{u} + \mathbf{u} \cdot \nabla \overline{\mathbf{U}} - \frac{1}{R}\nabla^2 \mathbf{u} - \nabla p = -\left(\mathbf{u} \cdot \nabla \mathbf{u} - \overline{\mathbf{u} \cdot \nabla \mathbf{u}}\right) \tag{4.7}$$

$$\nabla \cdot \mathbf{u} = 0 \tag{4.8}$$

$$\overline{\mathbf{U}}|_{r_i} = \hat{e}_\theta, \quad \overline{\mathbf{U}}|_{r_o} = \mathbf{u}|_{r_i} = \mathbf{u}|_{r_o} = \mathbf{0} \tag{4.9}$$

Direct Numerical Simulation

In order to validate our model solution, we perform DNS of TCF for a range of Reynolds number, $100 < R < 2000$, for a radius ratio $\eta = 0.714$ and an aspect ratio $L_z/d = 12$. However, our analysis is focused primarily on the cases $R = 100, 200$, and 400. The details of the numerical method can be found in Verzicco and Orlandi (1996); van der Poel et al. (2015); Zhu et al. (2018), and the details of the simulations performed in the context of the work presented here are summarized in Table 4.1. Since the DNS is intended as a reference, and not a result of this research, the numerical details of the simulation were not necessarily optimized for maximum efficiency.[2]

[2]The numerical simulations were performed by our collaborator Xiaojue Zhu.

R	N_r	N_θ	N_z	DOF ($N_r \times N_\theta \times N_z$)
100	101	768	512	39,714,816
200	101	768	512	39,714,816
400	129	768	512	50,724,864
650	129	768	512	50,724,864
1000	193	1024	640	126,484,480
2000	193	1024	640	126,484,480

Table 4.1: Numerical details of DNS

Resolvent Modeling

Here we apply the resolvent framework introduced in Chapter 2 to the set of Equations (4.7-4.9) under the assumption that the one dimensional mean velocity profile $\overline{\mathbf{U}}(r)$ is known. Chapter 5 discuss how the mean flow may be predicted from the laminar profile, without relying on data. We briefly review the derivation presented in Chapter 2, and go into detail of the specific case of the NSE in a cylindrical geometry. We begin by writing (4.7) and (4.8) as a balance between the linear dynamics and the nonlinear term which we group into a forcing term denoted by $\mathbf{f}$ as introduced in (2.7). For notational simplicity we define the state $\mathbf{u}$ to include both the three components of velocity, $[u_r, u_\theta, u_z]$ as well as the pressure p. We then Fourier transform the state $\mathbf{u}(r, z, \theta, t)$ and the nonlinear forcing $\mathbf{f}(r, z, \theta, t)$ in time as well as the homogeneous spatial directions, z and θ. For a function $\boldsymbol{q}(r, z, \theta, t)$ the Fourier transform is defined as

$$\hat{\boldsymbol{q}}(r, k_z, n, \omega) \equiv \int_{-\infty}^{\infty} \int_{\infty}^{\infty} \int_{0}^{2\pi} \boldsymbol{q}(r, z, \theta, t) e^{-i(k_z z + n\theta - \omega t)} \, d\theta \, dz \, dt. \tag{4.10}$$

Because the domain is periodic in the azimuthal direction and we formally consider the case $L_z = \infty$, we have $n \in \mathbb{Z}$ and $k_z, \omega \in \mathbb{R}$. This results in system of coupled ordinary differential equations (ODEs) for the Fourier modes $\hat{\mathbf{u}}_{\mathbf{k}}(r)$ and $\hat{\mathbf{f}}_{\mathbf{k}}(r)$ parameterized by the wavenumber triplet $\mathbf{k} \equiv [k_z, n, \omega]$.

$$(\mathbf{L}_{\mathbf{k}} - i\omega \mathbf{M}) \, \hat{\mathbf{u}}_{\mathbf{k}} = \hat{\mathbf{f}}_{\mathbf{k}} \tag{4.11}$$

The explicit expressions for the Fourier transformed linear operator $\mathbf{L}_{\mathbf{k}}$ and the weight matrix M are given in Appendix B.1. As introduced in Chapter 2, a singular value decomposition (SVD) of the resolvent provides an orthonormal basis for the velocity as well as the forcing. In this geometry the resolvent modes $\boldsymbol{\psi}_{\mathbf{k},j}$ and $\boldsymbol{\phi}_{\mathbf{k},j}$ are vector fields over r which are orthonormal with respect to an L_2 inner product over the three velocity components

$$\langle \mathbf{a}, \mathbf{b} \rangle \equiv \int_{r_i}^{r_o} a_m^*(r) b_m(r)\, r\, dr \tag{4.12}$$

with associated norm

$$\|\mathbf{a}\| \equiv \langle \mathbf{a}, \mathbf{a} \rangle^{1/2} \tag{4.13}$$

where summation over m is implied, such that

$$\langle \psi_{\mathbf{k},i}, \psi_{\mathbf{k},j} \rangle = \langle \phi_{\mathbf{k},i}, \phi_{\mathbf{k},j} \rangle = \delta_{ij}. \tag{4.14}$$

In this basis, each Fourier mode of the velocity and forcing may be written as

$$\hat{\mathbf{u}}_{\mathbf{k}} = \sum_{j=1}^{\infty} \sigma_{\mathbf{k},j} \chi_{\mathbf{k},j} \psi_{\mathbf{k},j} \tag{4.15}$$

$$\hat{\mathbf{f}}_{\mathbf{k}} = \sum_{j=1}^{\infty} \chi_{\mathbf{k},j} \phi_{\mathbf{k},j} \tag{4.16}$$

where $\chi_{\mathbf{k},j} \equiv \langle \phi_{\mathbf{k},j}, \hat{\mathbf{f}}_{\mathbf{k}} \rangle$ represents the projection of the (unknown) forcing onto the forcing modes.

Symmetries of Taylor Vortex Flow

The various flow states observed in TCF (TVF, WVF, and MWVF) may be defined by their spatio-temporal symmetries (Rand, 1982). We define TVF, the focus of this study, as a solution to (4.1) which is steady, axisymmetric, and axially periodic with fundamental wavenumber β_z, meaning we restrict ourselves to wavenumber vectors of the form $\mathbf{k} = [k_z, n, \omega] = [k\beta_z, 0, 0]$ where $k \in \mathbb{Z}$. This fundamental wavenumber β_z is related to the axial height of the Taylor vortices and is generally constrained by the experimental apparatus or computational box since the domain must contain an integer number of vortices. The resolvent formulation assumes an infinite axial domain so the choice of β_z is not immediately obvious. However, we found that the results shown in here are robust to changes in β_z as long as $\pi/2 \lesssim \beta_z \lesssim 4\pi/3$. Therefore, we choose the axial periodicity of our model to match that observed in our DNS, allowing for a direct comparison between our model and the DNS. The specific values of β_z are listed in Table 4.2. Given these symmetries, our model solution will consist of an expansion in Fourier modes

$$\mathbf{u}(r, z) = \sum_{k=1}^{N_k} \hat{\mathbf{u}}_k(r) e^{ik\beta_z z} + c.c. \tag{4.17}$$

where each Fourier mode $\hat{\mathbf{u}}_k$ is itself an expansion in resolvent modes given by (4.15) and $c.c.$ denotes the complex conjugate. We truncate the model at N_k Fourier

modes, each of which is expanded in N^k_{SVD} resolvent modes such that the final form of the TVF solution is given by

$$\mathbf{u}(r,z) = \sum_{k=1}^{N_k} \sum_{j=1}^{N^k_{SVD}} \sigma_{k,j}\chi_{k,j}\psi_{k,j}(r)e^{ik\beta_z z} + c.c. \tag{4.18}$$

Treatment of the Nonlinearity

At any given wavenumber, the forcing $\hat{\mathbf{f}}_k$ is given by a convolution sum of the interactions of all triadically compatible velocity modes.

$$\hat{\mathbf{f}}_k = -\sum_{m\neq 0}\sum_{n\neq 0} (\hat{\mathbf{u}}_m \cdot \nabla\hat{\mathbf{u}}_n)\, \delta_{m+n,k} \tag{4.19}$$

Here $\delta_{a,b}$ is the Kronecker delta which implies that the forcing at a given wave number k contains only interactions between Fourier modes whose wavenumbers sum to k. Throughout this chapter, we use the terminology *"$k_1 = k_2 + k_3$"* to refer to a single (resonant) triad involving the nonlinear interaction between Fourier modes with wavenumbers k_2 and k_3 forcing the Fourier mode with wavenumber k_1.

Equating the two expressions for the forcing mode given by (4.16) and (4.19) and substituting (4.15) for the velocity modes gives

$$\sum_{j=1}^{\infty} \chi_{k,j}\phi_{k,j} = \sum_{m\neq 0}\sum_{n\neq 0}\sum_{p=1}^{\infty}\sum_{q=1}^{\infty} -\chi_{m,p}\chi_{n,q}\sigma_{m,p}\sigma_{n,q}\left(\psi_{m,p}\cdot\nabla\psi_{n,q}\right)\delta_{m+n,k}. \tag{4.20}$$

Projecting both sides of (4.20) onto each forcing $\phi_{k,i}$ and dropping the summation symbols for simplicity gives

$$\chi_{k,i} = \chi_{m,p}\chi_{n,q}N_{kmn,ipq} \tag{4.21}$$

where the complex scalars $N_{kmn,ipq}$ are called the interaction coefficients and are given by

$$N_{kmn,ipq} \equiv -\sigma_{m,p}\sigma_{n,q}\langle\phi_{k,i}, \left(\psi_{m,p}\cdot\nabla\psi_{n,q}\right)\rangle\delta_{m+n,k} \tag{4.22}$$

which, critically, can be computed solely from knowledge of the linear operator $\mathbf{H}$.

Nonlinear interactions between the velocity fluctuations also appear in the divergence of the Reynolds stress on the right hand side of (4.5). This term is referred to as the "mean forcing" and is given by the sum of nonlinear interactions of all the $\hat{\mathbf{u}}_k$ and their complex conjugates $\hat{\mathbf{u}}_{-k}$, which can be directly interpreted as (4.19) evaluated at $k = \mathbf{0}$:

$$\overline{\mathbf{u}\cdot\nabla\mathbf{u}} = \sum_{k\neq\mathbf{0}} \left(\hat{\mathbf{u}}_k\cdot\nabla\hat{\mathbf{u}}_{-k} + \hat{\mathbf{u}}_{-k}\cdot\nabla\hat{\mathbf{u}}_k\right). \tag{4.23}$$

At this point, we would like to reiterate that the mean velocity profile is assumed to be known a priori. Thus the left hand side of (4.5), and therefore the Reynolds stress divergence on left hand side of (4.23), is also known.

We have thus reduced the NSE (under the assumption of a known mean velocity) to the infinite system of coupled polynomial equations (4.21) for the complex coefficients $\chi_{\mathbf{k},j}$ with the auxiliary condition that (4.23) is satisfied. While deriving an exact (nontrivial) solution to (4.20) may be a daunting task, we will demonstrate that approximate solutions can be efficiently computed by minimizing the residuals associated with (4.21) and (4.23).

Optimization Problem

We have recast the NSE in the language of resolvent analysis as

$$\chi_{k,j} - \chi_{m,p}\chi_{n,q}N_{kmn,jpq} = 0, \quad \forall\, k, j \tag{4.24}$$

$$\overline{\mathbf{u}\cdot\nabla\mathbf{u}} - \mathbf{f}_{0,k',pq}\chi_{k',p}\chi^*_{k',q} = \mathbf{0}, \tag{4.25}$$

$$\mathbf{f}_{0,k,pq} \equiv \sigma_{k,p}\sigma_{k,q}\left(\hat{\boldsymbol{\psi}}_{k,p}\cdot\nabla\hat{\boldsymbol{\psi}}^*_{k,q} + \hat{\boldsymbol{\psi}}^*_{k,q}\cdot\nabla\hat{\boldsymbol{\psi}}_{k,p}\right), \tag{4.26}$$

where we have expanded the velocity Fourier modes in their resolvent basis according to (4.15), and summation over m, n, and k' is implied. We truncate the expansion at some number of harmonics, N_k, of the fundamental wavenumber, and at each retained harmonic we truncate the singular mode expansion at N^k_{SVD} such that the total number of retained modes is $N = \sum_{k=1}^{N_k} N^k_{SVD}$. We seek to minimize the residuals (in the sense of the L_2 norm) associated with (4.24) and (4.25), and thus formulate the following optimization problem:

$$\min_{\chi_{k,j}} g^2(\chi_{k,j}) = a g_0^2(\chi_{k,j}) + (1-a) g^2_{triad}(\chi_{k,j}). \tag{4.27}$$

The first and second terms on the right hand side in (4.27) are defined as the mean constraint,

$$g_0(\chi_{k,j}) \equiv \frac{\|\overline{\mathbf{u}\cdot\nabla\mathbf{u}} - \mathbf{f}_{0,k',pq}\chi_{k',p}\chi^*_{k',q}\|}{\|\overline{\mathbf{u}\cdot\nabla\mathbf{u}}\|}, \tag{4.28}$$

and the triadic constraint,

$$g_{triad}(\chi_{k,j}) \equiv |\chi_{k,j} - \chi_{m,p}\chi_{n,q}N_{kmn,jpq}|. \tag{4.29}$$

The former represents the residual in the mean momentum equation (4.5), while the latter represents the residual in the equation for the fluctuations (4.7). The user

defined weighting parameter $a \in (0, 1)$ determines the relative penalization of each of these two constraints in the residual. This optimization problem differs in two main ways from a harmonic balance (HB) approach such as described in Rigas et al. (2021), where the NSE are solved directly in the frequency domain. First, the current approach assumes the mean velocity is known a priori, where as in the HB framework the mean velocity is computed online in a self consistent manner. Second, unlike the HB approach which minimizes the residual of the equations governing each Fourier mode in parallel, the current approach minimizes the sum of the integrated error in the mean and fluctuation equations.

At this point, we would like to highlight several important aspects of problem (4.27). First, we reiterate that the left hand term in the mean constraint (4.28) is a known function since the mean velocity profile is assumed to be known a priori. Second, we emphasize that we have assumed no closure model and made no modeling assumptions regarding the form of the nonlinear forcing in the derivation of (4.27). Lastly, while in general the amplitudes $\chi_{k,j} \in \mathbb{C}$, for the special case of steady, axially periodic, and axisymmetric solutions considered here, evaluating (4.11) and (B.1) for $\pm k$ reveals that $\chi_{k,j} \in \mathbb{R} \ \ \forall \ \ j, k$ meaning the optimization need only be carried out over a real valued domain. Note that if this method were applied to non-axially periodic solutions, one would have to consider complex coefficients.

Finally, we note that while the reformulation of the NSE (4.7) in the resolvent framework (4.24) is reminiscent of a Galerkin method (GM) where the governing equations are projected onto some predetermined set of basis functions, the current approach is appreciably different. Since we consider a steady process, we can not integrate the equations forward in time as would be generally done in a GM. Furthermore, since the resolvent framework provides a basis for both the velocity and the nonlinearity, (4.24) is an exact representation of (4.7) whereas a GM represents the governing equations only in an integral sense.

Solution Methodology

We solve the optimization problem (4.27) using a trust-region algorithm built into Matlab's $fminunc$ function for $R = 100,\ \ 200$, and 400. For each Reynolds number, the mean velocity profile used in constructing the linear operator is taken from the DNS described in §4.2. We note that various authors such as Mantič-Lugo et al. (2014, 2015); Rosenberg and McKeon (2019a); Bengana and Tuckerman (2021) have computed approximate mean velocity profiles from the laminar base flow

for a range of flows. These methods approximate the Reynolds stress as the self interaction of a single eigen- or resolvent mode. However, we note that Bengana and Tuckerman (2021) have described conditions under which such approximation are expected to fail. We do not employ such methods here, choosing instead to focus on the prediction of the velocity fluctuations about a known mean flow.

The gradient and Hessian of (4.27) may be derived explicitly and are input to the algorithm to improve accuracy. The weighting parameter a in (4.27) is set to 0.01 which means that the triadic constraint is penalized 99 times more heavily than the mean constraint. This reflects the observation that the triadic constraint which encodes the fully nonlinear governing equation for the fluctuations is far more complex than the mean constraint which, given the fact that the mean profile is known, is simply a least squares fit to a curve.

While this value of a was found to lead to the most consistent and accurate results, the results are qualitatively robust to changes in a as long as $0.0005 \lesssim a \lesssim 0.8$. If $a \lesssim 0.0005$, i.e. the triadic constraint is weighted too heavily, the optimization converges to the laminar state since the triadic constraint admits a trivial solution. If $a \gtrsim 0.8$, the mean constraint is weighted too heavily and the optimization tends to over fit to the input mean. Since the triadic constraint is simply a least squares fit to a known curve, the error can in principle be reduced arbitrarily with increased degrees of freedom. However, this does not guarantee that the resulting local minimum will represent a realistic solution.

The optimization also requires an initial guess. For this, we solve the rank 1 formulation of (4.27) using just one wavenumber, the fundamental, and one resolvent mode, in which case the minimum can be found analytically, resulting in an amplitude $\sigma_{1,1}\chi_{1,1} \approx 0.13$. We then initialize the full optimization such that $\sigma_{1,1}\chi_{1,1} = 0.13$ and the remaining $\sigma_{k,j}\chi_{k,j}$ are assigned random values between -0.01 and 0.01. This range of initial values was chosen to roughly reflect the expected roll off in the amplitudes $\sigma_{k,j}\chi_{k_j}$. However, we did not find any dependence on these initial values as long as these amplitudes were not all set to zero, in which case the optimization tends to converge to the trivial solution.

We assess the convergence and accuracy of our model solution using three metrics. First, we compute the final minimum residual of the cost function in (4.27) denoted g^*. Second, we compute the error of the model solution compared to the temporal average of the DNS solution

$$e_{dns} \equiv \sqrt{\sum_{k=1}^{N_k} \|\hat{\boldsymbol{u}}_k - \hat{\boldsymbol{u}}_{k,dns}\|^2} \tag{4.30}$$

where the norm is defined in (4.13). Third, we quantify the error of our model solution in solving the underlying governing equations (4.7), the details of which are discussed in §4.3.

We note that the error metric comparing our model to the DNS should be viewed with some caution since the Fourier decomposition of the DNS involves some inherent uncertainty. While our model is formulated in Fourier space, the DNS to which we compare our model utilizes a finite difference method in the axial direction. This means that the five or six Taylor vortices in the computational domain are not necessarily exactly the same size and the fundamental wavenumber β_z can only be defined in an average sense,

$$\beta_z = 2\pi \frac{n_{roll}}{L_z} \tag{4.31}$$

where n_{roll} is the number of Taylor vortices contained in the domain and L_z is the axial domain size. We use this average β_z in the construction of our model. To compute the DNS Fourier modes used in (4.30), we extract a single Taylor vortex whose size is closest to the average and perform a Fourier decomposition on this reduced domain. The largest difference between this best fit wavenumber and the average we observed was 0.5%. Since the radial shape of the Taylor vortices is expected to differ slightly with axial size it is unclear whether minor differences between our results and the DNS are due to errors in our model or uncertainties in the Fourier decomposition of the DNS.

At $R = 400$, which will be the main focus in this work, it was found that $N_k = 9$ axial wavenumbers with $N^k_{SVD} = 22$ for $k \leq 4$ and $N^k_{SVD} = 10$ for $k > 4$ resolvent modes were sufficient such that we did not observe any further meaningful decrease in the residual g^* with increased N. A detailed discussion of the choice of these particular truncation values is presented in §4.3. These truncation values, the total degrees of freedom, the axial wavenumber β_z, as well as the error metrics for all three Reynolds numbers are summarized in Table 4.2.

4.3 Results

Velocity Field Reconstruction

The final result of the model is shown in Figures 4.1 and 4.2 where we compare the model result and the DNS. We plot the mean-subtracted azimuthal velocity u_θ,

R	100	200	400
β_z	3.67	3.67	2.62
N_k	4	8	9
N^k_{SVD}	$12 \ \forall \ k$	$12(k \leq 4), \ 8(k > 4)$	$22(k \leq 4), \ 10(k > 4)$
N	48	80	138
g^*	2.3×10^{-3}	3.5×10^{-3}	5.5×10^{-3}
e_{dns}	2.5×10^{-3}	4.8×10^{-3}	1.5×10^{-2}
e_0	1.8×10^{-3}	1.3×10^{-3}	6.0×10^{-3}
e_{nse}	1.2×10^{-3}	2.7×10^{-3}	1.5×10^{-3}

Table 4.2: Reynolds numbers, fundamental wavenumber β_z, truncation values, degrees of freedom: N, final residuals: g^*, and error metrics defined by (4.30), (4.33), and (4.35) for the three model solutions presented.

and the azimuthal vorticity $\omega_\theta = \frac{\partial u_r}{\partial z} - \frac{\partial u_z}{\partial r}$ for $R = 100, \ 200$ and 400. The model solution is axisymmetric and steady by construction, and thus the radial and axial velocity are linked through continuity; no information is omitted by plotting ω_θ. As a comparison we show the azimuthal average of the mean subtracted DNS, however at this Reynolds number the flow is axisymmetric and steady, so the average field shown is representative of the flow at any azimuthal location and at any instance in time. There is good agreement between the resolvent model (top rows) and the DNS (bottom rows). The model accurately captures the dominant structure of the flow including the strong plumes of azimuthal velocity. The azimuthal vorticity exhibits a checkerboard pattern of regions of roughly constant vorticity of opposing signs. Regions of higher vorticity are concentrated near the walls, while the larger segments in the bulk of the domain have comparatively lower levels of vorticity. These results are in agreement with the DNS of Sacco et al. (2019), who found that as the Reynolds number increases this concentration of vorticity at the walls is enhanced and the bulk becomes increasingly "empty" of vorticity.

A more quantitative assessment of the model's accuracy is shown in figure 4.3 where we compare the individual Fourier modes of the model solution to the Fourier modes computed from the DNS. For clarity of presentation we focus on $R = 400$ and show only $(k \leq 4)$. However an analysis of the accuracy of all retained Fourier modes for all Reynolds numbers is presented in Figure 4.4 in §4.3. Compared to the DNS, the model slightly over-predicts the amplitude of the radial velocity for the fundamental Fourier mode, but the wall parallel components of the fundamental are captured almost exactly. Most striking is the good agreement of the higher harmonics. The largest scale dominates the contribution to the Reynolds stress

divergence and is thus determined primarily by the mean constraint, which as mentioned previously is relatively "easy" to solve. However the smaller scales require accurately approximating the solutions to the nonlinear triadic constraint, a much less trivial task. Furthermore, small deviations between the Fourier modes of the model and DNS are not necessarily indicative of errors in our model, since for the reasons discussed above, a Fourier decomposition of the DNS incurs some inherent uncertainty. A more rigorous assessment of how accurately our model solves the governing equations is presented in §4.3. Additionally, Figure 4.3a compares the DNS mean velocity profile, used as an input to the model, to the mean velocity profile computed by solving (4.5) with Reynolds stress term replaced by the mean forcing computed from the model itself.

$$\frac{1}{R}\nabla^2\bar{U}_{model} = \sum_{k\neq\mathbf{0}} (\hat{\mathbf{u}}_k \cdot \nabla\hat{\mathbf{u}}_{-k} + \hat{\mathbf{u}}_{-k} \cdot \nabla\hat{\mathbf{u}}_k) \tag{4.32}$$

The input and output mean velocity profile show very good agreement, with only some mild discrepancy at the edge of the inner boundary layer. The error in mean velocity may be computed as

$$e_0 \equiv \|\bar{U}_{DNS} - \bar{U}_{model}\| \tag{4.33}$$

which is associated with residual of the mean constraint (4.28) in (4.27). However, note that while (4.33) is written in terms of the mean velocity, (4.28) is written in terms of the Reynolds stress divergence. The values of e_0 for all three Reynolds numbers are tabulated in Table 4.2. We generally do not use (4.33) as one of the measures of convergence since very few modes are required to accurately capture the mean, and thus e_0 reaches a minimum long before the full nonlinear flow is converged. This is consistent with past studies which have shown that the mean velocity profile of various flows may be accurately modeled using the Reynolds stress divergence of a single resolvent or eigenmode (Mantič-Lugo et al., 2014, 2015; Rosenberg and McKeon, 2019a).

Overall, the success of the model in capturing this fully developed TVF indicates that, despite its fully nonlinear nature, the full solution remains relatively low dimensional. Nevertheless, given the relative simplicity of the flow, the model reduction is not as drastic as one might expect from an analysis purely of the energetic content of the flow. At $R = 400$, the velocity associated with the third harmonic ($k = 4$) is two orders of magnitude less than the fundamental, and yet nine wavenumbers must be retained in order to achieve the convergence shown here. The dynamic importance of these energetically weak harmonics is discussed in §4.3.

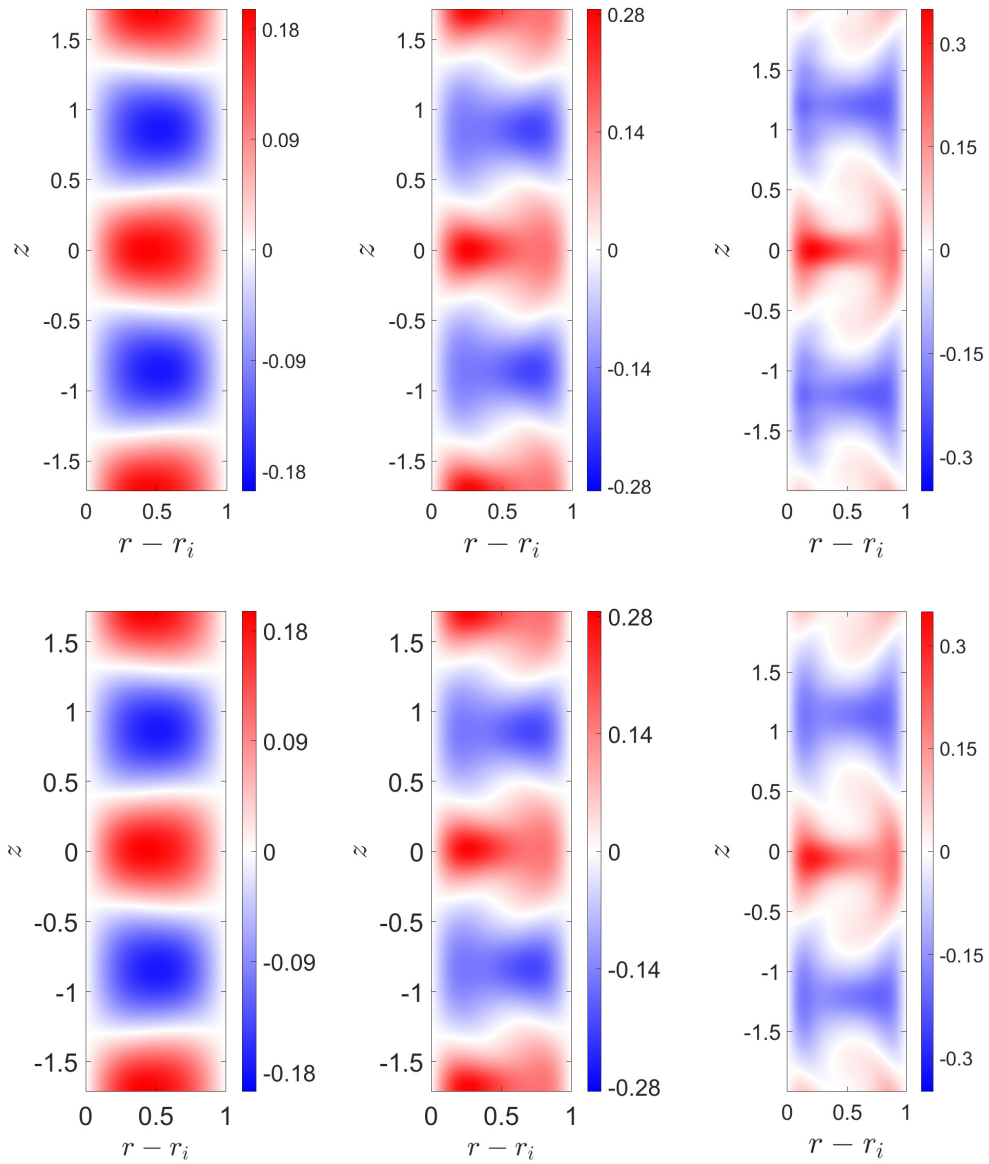

Figure 4.1: Mean subtracted azimuthal velocity u_θ computed from our model (top row) and DNS (bottom row) at (from left to right) $R = 100,\ \ 200$, and 400.

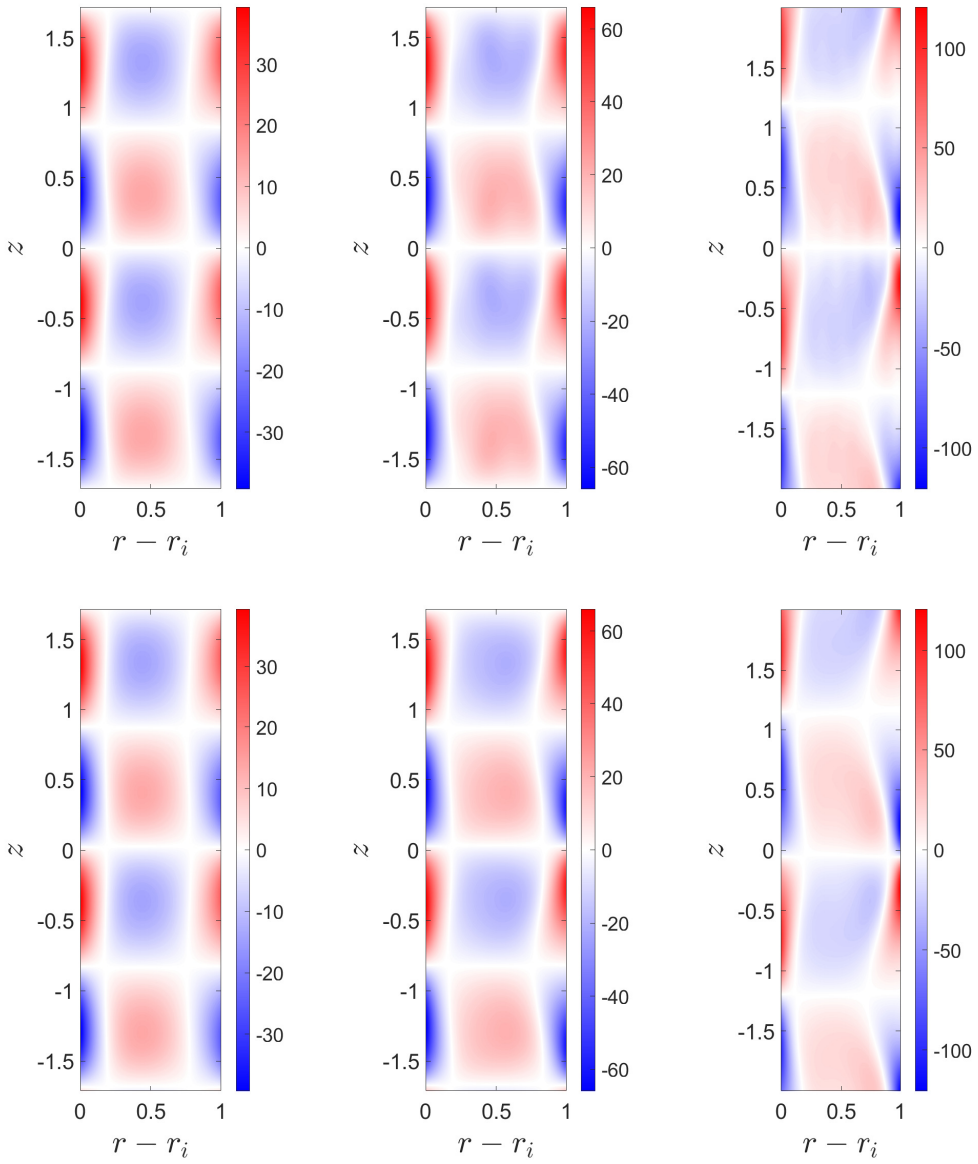

Figure 4.2: Azimuthal vorticity $\omega_\theta = \frac{\partial u_r}{\partial z} - \frac{\partial u_z}{\partial r}$ computed from our model (top row) and DNS (bottom row) at (from left to right) $R = 100,\ \ 200$, and 400.

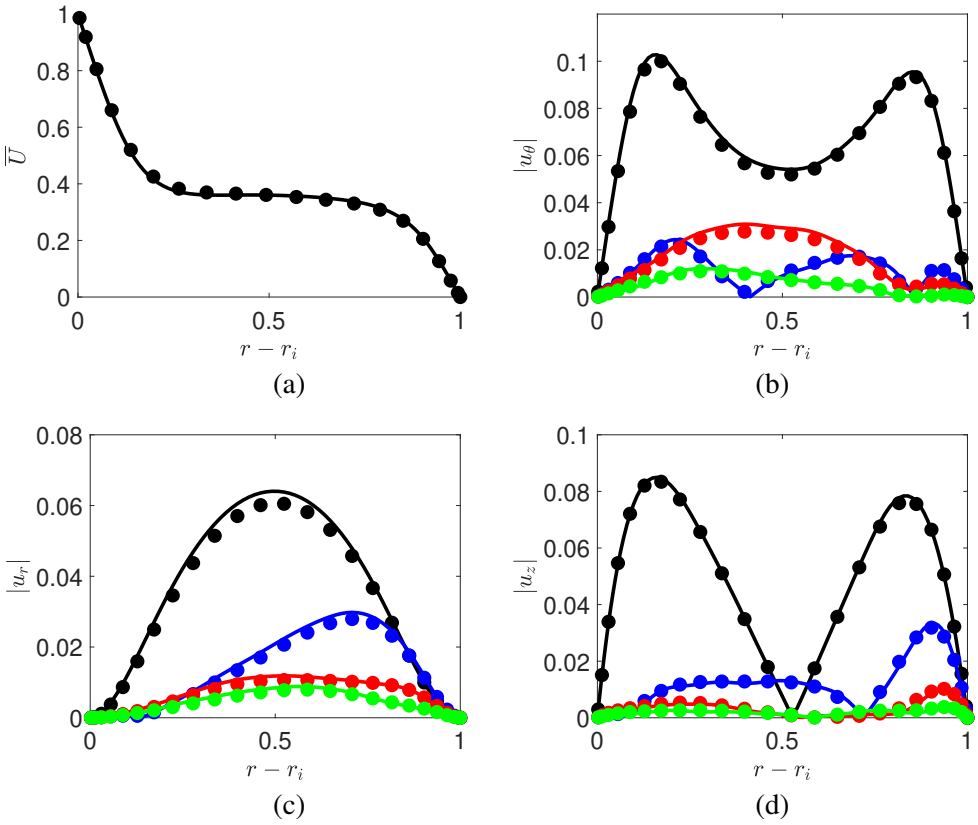

Figure 4.3: Model solution (lines) compared to the DNS (symbols) at $R = 400$. Mean velocity profile, $\bar{U}$, computed from Reynolds stress divergence of model compared to input mean velocity from DNS (a). First five Fourier modes of model solution, $\hat{u}_\theta$, $\hat{u}_r$, $\hat{u}_z$ (b-d), $k = 1$ (black), $k = 2$ (blue), $k = 3$ (red), $k = 4$ (green).

Self Sustaining Solutions: Closing the Resolvent Loop

We have shown that our model accurately captures the structure of the TVF observed in the DNS. Now we analyze the accuracy of our model viewed from the perspective of a self sustaining process. In other words, we assess how accurately our model approximates a solution to the governing equations (4.7). In the resolvent framework, the nonlinear term is interpreted as a forcing to the linear dynamics. As such, a solution is self-sustaining if the sum of all triadic interactions at a particular wavenumber provide the correct forcing for the response at that wavenumber. This means that we must have

$$\hat{\mathbf{u}}_k = \mathbf{H}_k \sum_{m\neq 0} \sum_{n\neq 0} -(\hat{\mathbf{u}}_m \cdot \nabla \hat{\mathbf{u}}_n)\, \delta_{m+n,k} \quad \forall \quad k. \tag{4.34}$$

Note that (4.34) is simply a restatement of (4.11) with the nonlinear forcing written explicitly in terms of $\hat{\boldsymbol{u}}_k$ and that our model will generally not satisfy (4.34) exactly.

Here we refer to the direct result of our model, i.e. the quantity on the left hand side of (4.34), as the *"primary"* velocity, and we denote the right hand side of (4.34), computed from that model solution, as the *"forced"* velocity. In Figure 4.4 we plot the azimuthal component of both the primary and forced Fourier modes for all the wavenumbers and for all three Reynolds numbers. For all Reynolds numbers and wavenumbers agreement between the primary (open circles) and forced mode (lines) is very good indicating that our model is indeed a close approximation of a solution to (4.7). Figure 4.4 also shows the Fourier modes computed from the DNS for comparison (open squares). We see that there is growing discrepancy between the model result and the DNS modes with increasing wavenumber. However note that the discrepancy between the model and the DNS, which is only present in the higher harmonics, is two orders of magnitude smaller than the amplitude of the fundamental. This discrepancy is due to the structure of the nonlinear forcing and is discussed further in §4.3. Additionally, we note that for both the model and DNS the mode shapes of the higher harmonics, $k \gtrsim 3$ do not seem to differ significantly with increasing k indicating some level of universality as the length scale decreases.

We quantify the total error in nonlinear compatibility as

$$e_{nse} = \sqrt{\sum_{k=1}^{N_k} \|\hat{\mathbf{u}}_k - \mathbf{H}_k \sum_{m\neq 0} \sum_{n\neq 0} -\left(\hat{\mathbf{u}}_m \cdot \nabla \hat{\mathbf{u}}_n\right) \delta_{m+n,k}\|^2}. \tag{4.35}$$

This may be thought of as the total residual associated with how accurately our model solution approximates a solution to (4.7), or in other words it represents the final residual associated with the triadic constraint (4.29). For all three Reynolds numbers considered, the error is $O(10^{-3})$, with the exact values listed in Table 4.2.

Analysis of the Forcing Structure

Here we investigate which individual triadic interactions are most important in sustaining the flow and how these vary with Reynolds number. As previously noted, for $R = 200, 400$, the higher harmonics: $k \gtrsim 5$, do not contribute significantly to the energy content of the flow yet still play a crucial role in the nonlinear forcing of the larger structures and are necessary to achieve the convergence shown in Figures 4.1 and 4.2. To identify the mechanics underlying the forcing structure, we compute the individual terms in the summation on the right hand side of (4.34). These individual contributions of the forced velocity, defined as

$$\hat{\boldsymbol{v}}_{k,k'} \equiv -\mathbf{H}_k \left(\hat{\mathbf{u}}_{k'} \cdot \nabla \hat{\mathbf{u}}_{k-k'} + \hat{\mathbf{u}}_{k-k'} \cdot \nabla \hat{\mathbf{u}}_{k'} (1 - \delta_{k,2k'})\right) \tag{4.36}$$

represent the contribution of each individual triadic interaction in (4.34) and are shown in Figures 4.5 and 4.6 for $R = 100$ and $R = 400$, respectively. The individual contributions (4.36) are plotted with colored symbols and the full Fourier mode is plotted in black. By definition the individual contributions (symbols) sum to the full Fourier mode (solid black). To clarify the following discussion, we define a *"(forward) forcing cascade"* as the forcing of mode k_0 by interactions involving strictly modes $k \leq k_0$ and an *"inverse forcing cascade"* as the forcing of mode k_0 by interactions involving at least one $k > k_0$.

At $R = 100 \approx 1.25R_c$, we observe a forcing mechanism reminiscent of a weakly nonlinear theory where the harmonics are all driven exclusively by a forward forcing cascade. The $k = 2$ mode is driven primarily by the self interaction of the $k = 1$ mode, the $k = 3$ mode is driven by the interaction of the $k = 1$ and $k = 2$ modes, and so on. In other words, modes with wavenumber k_0 do not contribute to the forcing of modes with wavenumber $k < k_0$.

The higher Reynolds number model solutions do not exhibit the same unidirectional forcing cascade observed close to the bifurcation from laminar flow. We plot the same individual triadic contributions (4.36) for $R = 400 \approx 5R_c$ in Figure 4.6. For the harmonics ($k > 1$), the pair of contributions due to triadic interactions involving the fundamental ($k = \pm 1$), i.e. $k = (k+1) - 1$ and $k = (k-1) + 1$, have large, almost equal amplitudes but are of opposite sign and almost cancel. The same phenomenon is observed for the triads involving the $k = \pm 2$ mode, albeit it is not as pronounced as for the triads involving the fundamental. This raises the question of whether or not these components exactly cancel, and thus do not play a significant role in the dynamics, or whether the small differences in shape and amplitude dictate the structure of the resulting mode. To investigate this, we compute the projection of the individual triadic contributions onto the full mode

$$\Gamma_{k,k-k',k'} \equiv \frac{\langle \hat{\boldsymbol{v}}_{k,k'}, \hat{\mathbf{u}}_k \rangle}{\langle \hat{\mathbf{u}}_k, \hat{\mathbf{u}}_k \rangle}. \tag{4.37}$$

These projections are plotted in Figures 4.7 and 4.8 for $R = 100$, and $R = 400$, respectively. Each sub-figure corresponds to one Fourier mode, k_1, and the color in each tile represents the magnitude and sign of the contribution to that k_1 Fourier mode from the triadic interaction between k_2 and k_3. As expected from Figure 4.6, we observe pairs of strong negative and positive correlations from the two triads involving the fundamental, $k = 1$, with less pronounced, but still evident, pairing between triads involving $k = \pm 2$. Since the Γ_{k1,k_2,k_3} represent a relative fractional

contribution, the sum over k_2 and k_3 of the entries in each sub-figure is equal to unity for all k_1. Note that to improve readability the sub-figures in Figure 4.8 each have individual color scales.

In order to quantify the importance of all triadic combinations involving a certain wavenumber k_2 to the shape of the Fourier mode with wavenumber k_1, we compute sum of the Γ_{k1,k_2,k_3} over k_3 for all k_1 and for all three Reynolds numbers, This metric is plotted in 4.9. Practically this can be thought of as a summation over the columns in each sub-figure of Figures 4.7 and 4.8 as well as the equivalent case for $R = 200$ (not shown). Figure 4.9 makes it clear that, for a given k, it is the two pairs of triads $k = (k + 1) - 1$ and $k = (k - 1) + 1$ as well as $k = (k+2) - 2$ and $k = (k-2) + 2$ which provide the dominant share of the forcing. We note that similar instances of destructive interference have been observed by other authors such as Nogueira et al. (2021) in their analysis of forcing statistics in plane Couette flow and Rosenberg and McKeon (2019b) in their interpretation of the Orr-Sommerfeld/Squire decomposition of the resolvent operator.

The large scales at $R = 200$ are driven almost entirely by the pair of triads involving $k = \pm 1$ with the pair involving $k = \pm 2$ only becoming active for $k \geq 4$. At $R = 400$ the forcing is more distributed among the various triadic interactions indicating a higher degree of nonlinearity. However, the triads involving $k = \pm 1$ and $k = \pm 2$ are clearly still dominant. In fact the contribution of the triads involving $k = \pm 2$ is comparable and sometimes greater than the contributions from those involving $k = \pm 1$. Nevertheless, it is the triads involving the fundamental which have the largest amplitude contributions and display the largest degree of destructive interference.

At this point, we would like to revisit the discrepancy between the Fourier modes of the model solution and the DNS observed in Figure 4.4. Recall that due to the structure of the forcing, an accurate reconstruction of a particular Fourier mode with wavenumber k_0 requires accurate knowledge of its harmonic, $k_0 + 1$. Practically, the model must be truncated at some point, so there will always be a maximum wavenumber k_m whose harmonic $k_m + 1$ is unknown. Therefore there will be some error in the reconstruction of $\hat{\boldsymbol{u}}_{k_m}$ since $\hat{\boldsymbol{u}}_{k_m+1}$ is unavailable to participate in the inverse forcing cascade described above. This error will then "back propagate" through Fourier space until it is outweighed by the influence of the large scales and the constraint imposed on those large scales by the input mean flow. A detailed analysis of how the Fourier space truncation affects the convergence of the optimization

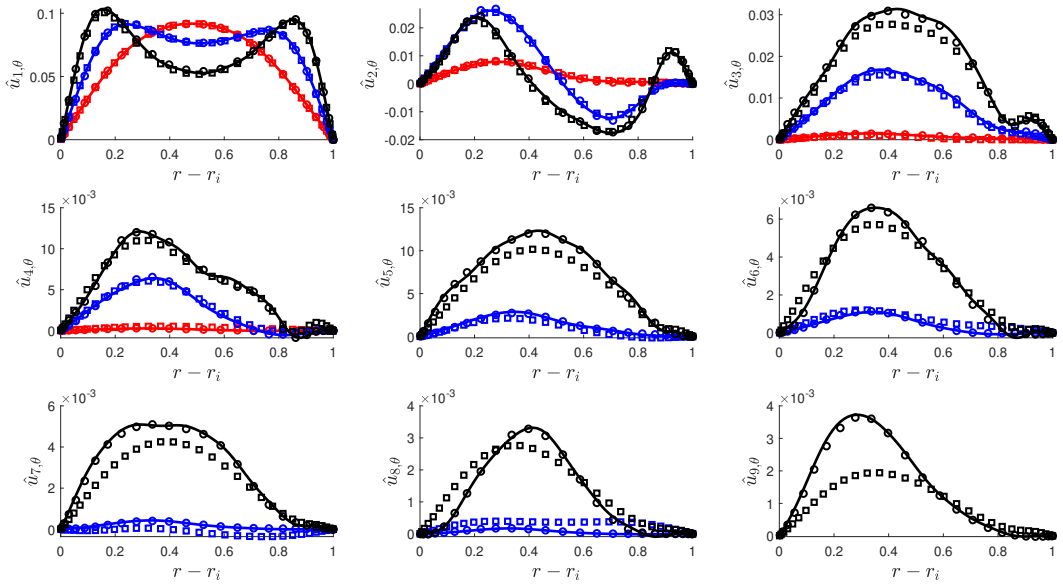

Figure 4.4: Azimuthal velocity component of the model solution's primary Fourier mode (open circles) and forced Fourier mode (lines) as well as the Fourier modes from DNS (open squares) for $R = 100$ (red), $R = 200$ (blue), and $R = 400$ (black). Top row $k = 1 - 3$, middle row $k = 4 - 6$, bottom row: $k = 7 - 9$.

is beyond the scope of this work, however it is interesting to note that, while the higher harmonics of our model solution deviate slightly from the DNS, they remain nonlinearly compatible to a very good approximation. In other words, the primary and forced Fourier modes of the model solution in Figure 4.4 agree very well as quantified by the small residuals as defined by (4.35) and listed in Table 4.2.

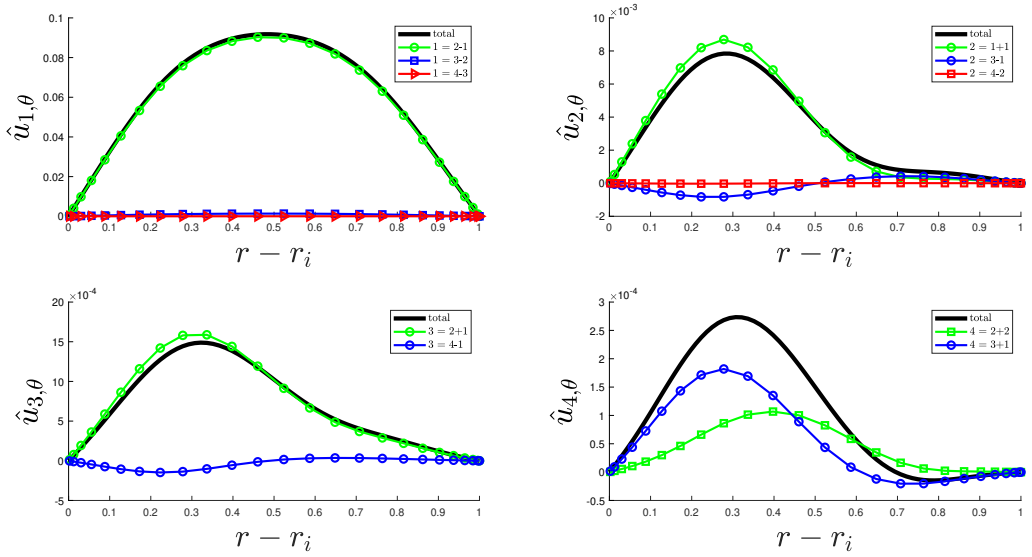

Figure 4.5: Azimuthal velocity component of the forced Fourier modes at $R = 100$. The individual triadic contributions, $\hat{\boldsymbol{v}}_{k,k'}$, are shown in colored symbols and the full Fourier mode, $\hat{u}_{k,\theta}$, is plotted in solid black. The sum of the individual triad components, (symbols) add up to the total forced mode (solid black). Top row $k = 1 - 2$, bottom row: $k = 3 - 4$.

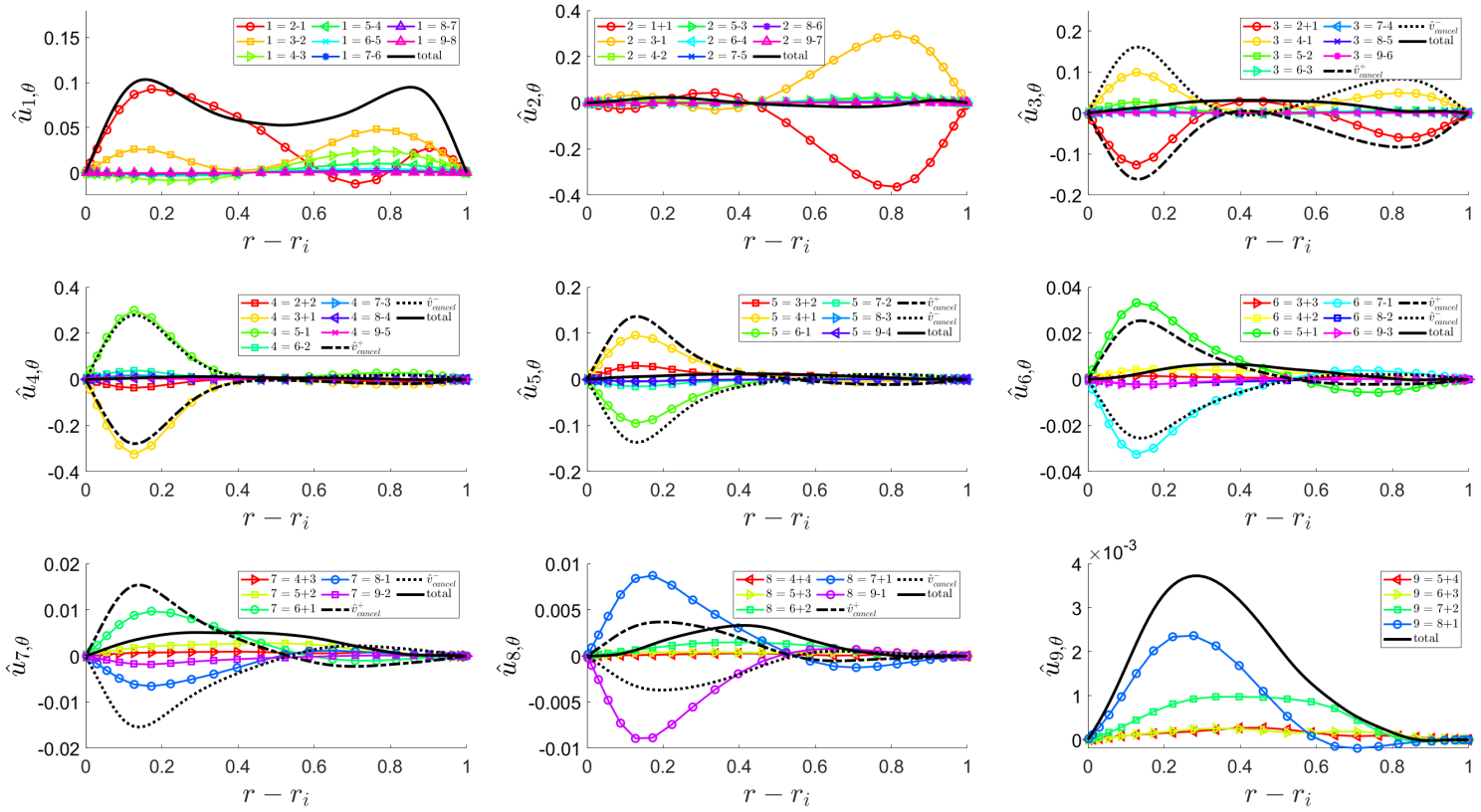

Figure 4.6: Azimuthal velocity component of the forced Fourier modes at $R = 400$. The individual triadic contributions, $\hat{\boldsymbol{v}}_{k,k'}$, are shown in colored symbols and the full Fourier mode, $\hat{u}_{k,\theta}$, is plotted in solid black. The sum of the individual triad components, (symbols) add up to the total forced mode (solid black). The predicted canceling azimuthal velocity contributions, $\hat{v}^{\pm}_{k,cancel,\theta}$, derived in §4.3 are plotted in dashed and dotted black lines. Top row $k = 1 - 3$, middle row $k = 4 - 6$, bottom row: $k = 7 - 9$.

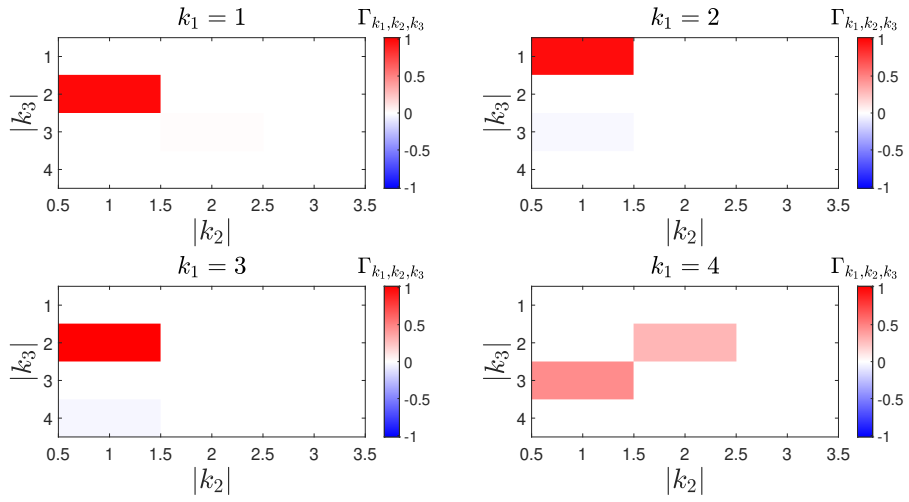

Figure 4.7: Projections of the velocity due to individual triadic interactions onto the full Fourier mode, Γ_{k_1,k_2,k_3}, at $R = 100$. Top row $k = 1 - 2$, bottom row: $k = 3 - 4$.

The Transition from Weakly to Fully Nonlinear Taylor Vortices

Many studies have approached the nonlinear modeling of TVF through weakly nonlinear (WNL) theory, where the general premise is that the structure of the largest scale is given by the critical eigenmode and that the higher harmonics are all derived from that fundamental mode (Stuart, 1960; Yahata, 1977; Jones, 1981; Gallaire et al., 2016). Despite being formally valid for only a small range of Reynolds numbers close to R_c, the mathematical difficulties associated with the nonlinearity of the NSE often necessitate the use of WNL methods outside this domain of validity (Gallaire et al., 2016). Our results illuminate the physical mechanisms which lead to the eventual failure of WNL theory as the Reynolds number increases. WNL theory proceeds by expanding the solution in an asymptotic series about the bifurcation point such that the leading order solution u_0 is the laminar base flow and the $O(\epsilon)$ solution u_1 is given by the critical eigenmode. The $O(\epsilon^2)$ solution u_2 as well as the mean flow correction is then found by solving the linear system forced by the nonlinear self interaction of u_1. The higher order terms may then be similarly computed sequentially by solving a forced linear system of the form $\mathbf{L}_k u_k = f(u_1, u_2, ..., u_{k-1})$. At the lowest Reynolds number considered here, $R = 100$, this formulation is valid since as shown in Figures 4.5 and 4.7 the forcing for a certain $\hat{\boldsymbol{u}}_k$ depends only on interactions between larger scales. However, as discussed in §4.3, at higher Reynolds numbers the forcing is dominated by pairs of triads, one of which involves $\hat{\boldsymbol{u}}_{k+1}$, a mechanism which is impossible in the WNL formulation.

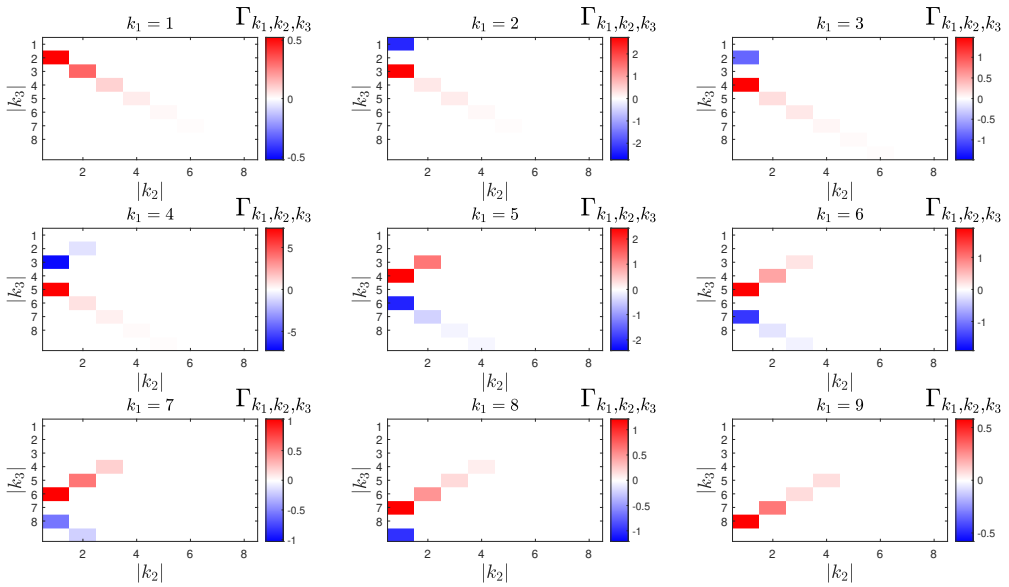

Figure 4.8: Projections of the velocity due to individual triadic interactions onto the full Fourier mode, Γ_{k_1,k_2,k_3}, at $R = 400$. Top row $k = 1-3$, middle row $k = 4-6$, bottom row: $k = 7-9$.

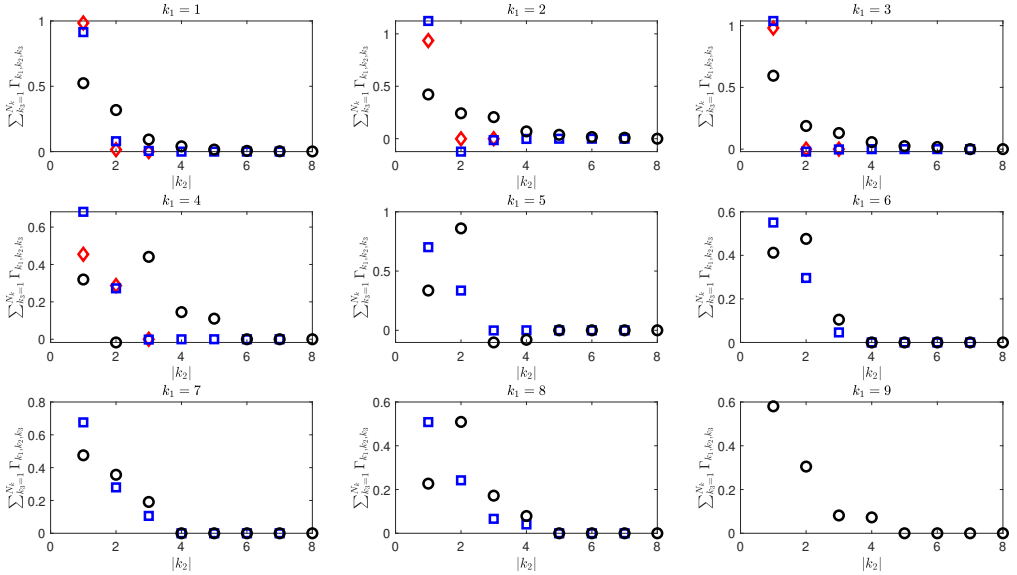

Figure 4.9: Projections of the velocity due to individual triadic interactions onto the full Fourier mode summed over common wavenumbers. $R = 100$ in red, $R = 200$ in blue squares, and $R = 400$ in black circles. Top row $k = 1-3$, middle row $k = 4-6$, bottom row: $k = 7-9$.

This means that near the bifurcation from the laminar state a model solution of the nonlinear flow may be truncated at the highest wavenumber of interest since a given wavenumber depends only on its sub-harmonics. We define such a flow to be in the *"weakly nonlinear"* (WNL) regime. As the Reynolds number increases the forcing cascade is no longer only from large to small scales and an equally important inverse cascade mechanism emerges. In this case, we define the flow to be in the *"fully nonlinear"* (FNL) regime. For the case of $\eta = 0.714$ considered here, this transition occurs around some $100 < R < 200$. These findings indicate that if one desires to model a certain number of harmonics of a given flow, the expansion must be carried out to significantly higher order than the highest harmonic of interest.

Sacco et al. (2019) noted a similar transition in the dynamics of turbulent Taylor vortices. They note that while Taylor vortices first arise due to a supercritical centrifugal instability of the laminar base flow, for $R \sim O(10^4)$ they persist in the limit of zero curvature i.e. in the absence of centrifugal effects Nagata (1990); Sacco et al. (2019). At sufficiently high Reynolds numbers, they find that the temporal evolution of the r.m.s. velocity associated with the Taylor vortex and the mean shear are perfectly out of phase and fluctuate with a common characteristic frequency. Their results build on the work of Dessup et al. (2018) who show that the traveling waves in WVF arise due to an instability of the streaks and that the rolls are sustained by the nonlinear interaction of these traveling waves. Together these findings indicate a regenerative self sustaining process similar to the framework suggested by Waleffe (1997); Hamilton et al. (1995). Since we consider steady TVF, it is difficult to make a direct comparison between either of these studies and ours. However, it is possible that the transition from weakly to fully nonlinear Taylor vortices that we observe is the genesis of the type of self-sustaining Taylor vortices described by Sacco et al. (2019) and Dessup et al. (2018)

Destructive Interference Forcing Structure

As described in §4.3, we observe that in the FNL regime a crucial component of the forcing at a given wavenumber k is the destructive interference of the two triads $k = (k-1)+1$ and $k = (k+1)-1$. This pair of triads leads to velocity contributions with large amplitudes but with opposite sign. This means that an accurate reconstruction of a Fourier mode with wavenumber k requires knowledge of both its subharmonic $k-1$ and its harmonic $k+1$. In this section, we show that for streamwise constant and spanwise periodic solutions, as considered in this work, this large amplitude destructive interference is a direct consequence of the structure

of the Fourier representation of the nonlinear term $\boldsymbol{u}\cdot\nabla\boldsymbol{u}$. In cylindrical coordinates, the nonlinear interaction between two axisymmetric Fourier modes $\boldsymbol{a} = [a_r, a_\theta, a_z]$ and $\boldsymbol{b} = [b_r, b_\theta, b_z]$ with axial wavenumbers k_a and k_b is given by

$$\boldsymbol{f}_{a,b} \equiv \boldsymbol{a}\cdot\nabla\boldsymbol{b} + \boldsymbol{b}\cdot\nabla\boldsymbol{a} \tag{4.38}$$

where the axial derivative in the gradient operator is replaced by multiplication by ik_b and ik_a, respectively. For clarity of exposition, we limit the following analysis to the azimuthal component of the forcing and note that analogous arguments hold for the remaining two components. The forcing at wavenumber k due to the interactions of $k-1$ and 1 is given by

$$\hat{\boldsymbol{f}}^{+} \equiv \hat{\boldsymbol{u}}_1\cdot\nabla\hat{\boldsymbol{u}}_{k-1} + \hat{\boldsymbol{u}}_{k-1}\cdot\nabla\hat{\boldsymbol{u}}_1. \tag{4.39}$$

Using the continuity equation to eliminate the axial velocity, the azimuthal component takes the form

$$f_\theta^{+} = \left(\hat{u}_{1,r}\hat{u}'_{k-1,\theta} + \hat{u}_{k-1,r}\hat{u}'_{1,\theta} + \frac{\hat{u}_{1,\theta}\hat{u}_{k-1,r}}{r} + \frac{\hat{u}_{k-1,\theta}\hat{u}_{1,r}}{r}\right) - (k-1)\frac{(r\hat{u}_{1,r})'\hat{u}_{k-1,\theta}}{r} - \frac{(r\hat{u}_{k-1,r})'\hat{u}_{1,\theta}}{r(k-1)}. \tag{4.40}$$

Similarly, forcing due to the interactions of $k+1$ and -1 is given by

$$\hat{\boldsymbol{f}}^{-} \equiv \hat{\boldsymbol{u}}_{-1}\cdot\nabla\hat{\boldsymbol{u}}_{k+1} + \hat{\boldsymbol{u}}_{k+1}\cdot\nabla\hat{\boldsymbol{u}}_{-1}, \tag{4.41}$$

with the azimuthal component taking the form

$$f_\theta^{-} = \left(\hat{u}_{1,r}\hat{u}'_{k+1,\theta} + \hat{u}_{k+1,r}\hat{u}'_{1,\theta} + \frac{\hat{u}_{1,\theta}\hat{u}_{k+1,r}}{r} + \frac{\hat{u}_{k+1,\theta}\hat{u}_{1,r}}{r}\right) + (k+1)\frac{(r\hat{u}_{1,r})'\hat{u}_{k+1,\theta}}{r} + \frac{(r\hat{u}_{k+1,r})'\hat{u}_{1,\theta}}{r(k+1)}. \tag{4.42}$$

Here the superscript $'$ denotes partial derivatives with respect to r, and we have made use of the fact that for the streamwise constant fluctuations considered here $\hat{\boldsymbol{u}}_{-1} = \hat{\boldsymbol{u}}_1^* = [\hat{u}_{1,r}, \hat{u}_{1,\theta}, -\hat{u}_{1,z}]$.

For some integer wavenumber $k > 1$, the Fourier modes associated with the nearest neighbor wavenumbers $k \pm 1$ are defined as

$$\hat{\boldsymbol{u}}(r)_{k\pm1} \equiv \int_{-\infty}^{\infty} \boldsymbol{u}(r,z)e^{i\beta_z(k\pm1)z}dz = \int_{-\infty}^{\infty} \boldsymbol{u}(r,z)e^{i\beta_z k(1\pm\frac{1}{k})z}dz. \tag{4.43}$$

Since the destructive interference is most pronounced for small scales, we formally consider the case of $k \gg 1$, for which we can expand (4.43) in a Taylor series about $k^{-1} = 0$.

$$\hat{\boldsymbol{u}}_{k\pm1} = \int_{-\infty}^{\infty} \boldsymbol{u} \left(e^{i\beta_z kz} \pm i\beta_z k^{-1} e^{i\beta_z kz} + O(k^{-2}) \right) dz = \hat{\boldsymbol{u}}_k + O(k^{-1}). \tag{4.44}$$

This indicates that for $k \gg 1$, $\hat{\boldsymbol{u}}_k$ and $\hat{\boldsymbol{u}}_{k\pm1}$ differ by a quantity which is $O(k^{-1})$, meaning that for large values of k the shape of the Fourier modes does not change drastically with increasing k. Figure 4.4 shows that this is indeed the case. Substituting $\hat{\boldsymbol{u}}_{k\pm1} = \hat{\boldsymbol{u}}_k + O(k^{-1})$ into (4.40) and (4.42), we find at leading order

$$f_\theta^+ = f_{\theta,eq} - k\frac{(r\hat{u}_{1,r})'\hat{u}_{k,\theta}}{r} + O(k^{-1}) \tag{4.45}$$

$$f_\theta^- = f_{\theta,eq} + k\frac{(r\hat{u}_{1,r})'\hat{u}_{k,\theta}}{r} + O(k^{-1}) \tag{4.46}$$

where $f_{\theta,eq}$ is the same for both triads and is given by

$$f_{\theta,eq} = \left[\hat{u}_{1,r}\hat{u}'_{k,\theta} + \hat{u}_{k,r}\hat{u}'_{1,\theta} + \frac{\hat{u}_{1,\theta}\hat{u}_{k,r}}{r} + \frac{\hat{u}_{k,\theta}\hat{u}_{1,r}}{r} + \frac{(r\hat{u}_{1,r})'\hat{u}_{k,\theta}}{r} \right]. \tag{4.47}$$

The only remaining terms are equal in magnitude but of opposite sign. Furthermore, since both $\hat{u}_{1,r}$ and $\hat{u}_{k,\theta}$ are bounded and nonzero, these remaining terms will scale proportionally with k and therefore are expected to have large amplitudes since we have assumed $k \gg 1$. Expressions (4.45) and (4.46) predict that the large amplitude destructive interference observed in Figures 4.6 and 4.8 occurs through the terms $\pm k\frac{(r\hat{u}_{1,r})'\hat{u}_{k,\theta}}{r}$.

Similar expressions can be derived for the other two components such that the two vector forcing terms proportional to k which are expected to cancel are given by

$$\hat{\boldsymbol{f}}^{\pm}_{k,cancel} \equiv \mp k\frac{(r\hat{u}_{1,r})'}{r}\hat{\boldsymbol{u}}_k \quad (k \gg 1). \tag{4.48}$$

This prediction may be tested by computing the corresponding velocity contributions to the Fourier mode with wavenumber k, given by

$$\hat{\boldsymbol{v}}^{\pm}_{k,cancel} = -\mathbf{H}_k \hat{\boldsymbol{f}}^{\pm}_{k,cancel}, \quad (k \gg 1), \tag{4.49}$$

and comparing its shape to that of the total velocity contributions $\hat{\boldsymbol{v}}_{k,\pm1}$ defined in (4.36). In Figure 4.6, we plot the $\hat{\boldsymbol{v}}^{\pm}_{k,cancel}$ alongside the individual $\hat{\boldsymbol{v}}_{k,\pm1}$ for $2 < k < 9$. We do not plot these approximations for $k = 1$ and 2 since they violate

the assumption that $k \gg 1$ nor the highest retained wavenumber, $k = 9$, since $k = 10$ is not included in our model. We find that $\hat{\boldsymbol{v}}^{\pm}_{k,cancel}$ is a quite accurate approximation of $\hat{\boldsymbol{v}}_{k,\pm 1}$ in this intermediate range of k despite the derivation having assumed that $k \gg 1$. These findings establish that $\hat{\boldsymbol{f}}^{\pm}_{k,cancel}$ is indeed responsible for the large amplitude destructive interference characteristic of the fully nonlinear regime.

Inspection of the spectral dynamics of the flow corroborate this finding. If we assume that the Fourier modes $\hat{\boldsymbol{u}}_k$ obey a power law

$$\|\hat{\boldsymbol{u}}_k\| \sim k^{-p}, \tag{4.50}$$

then, from (4.48), the forcing component $\hat{\boldsymbol{f}}^{\pm}_{k,cancel}$ must obey the power law

$$\|\hat{\boldsymbol{f}}^{\pm}_{k,cancel}\| \sim k^{1-p}. \tag{4.51}$$

Thus the flow will be in the WNL regime as long as $p \gg 1$, and we expect the flow to have transitioned to the FNL regime if $p \lesssim 1$. In Figure 4.10, we plot the norm of the Fourier modes computed from the DNS data for a range of Reynolds numbers. For all cases, the Fourier modes decay in Fourier space faster than k^{-1} which is depicted by the dashed black line. However, the decay rate at $R = 100$ is significantly faster than for the higher Reynolds number cases which seem to converge to a decay rate which is roughly independent of Reynolds number. The inset of Figure 4.10 shows the exponent of the best fit power law for all Reynolds numbers. For $R = 100$, we fit the power law only to $k \leq 5$ since for $5 < k \leq 10$ the norm of the Fourier components remains roughly constant. At $R = 100$, in the WNL regime, the best fit exponent is approximately 5 while the higher Reynolds numbers, which are in the FNL regime, all exhibit an exponent which seems to approach an asymptote close to 1. These findings are in agreement with the analysis presented above which predicts that in the WNL regime the decay rate of the Fourier modes is much faster than k^{-1} and the transition to the fully nonlinear regime is associated with the decay rate approaching k^{-1}.

Model Reduction

Here we address how the particular truncation values N^k_{SVD} were chosen, and how the number of retained wavenumbers and resolvent modes at each wavenumber affects the accuracy of the model. At $R = 100$, the flow is in the weakly nonlinear regime and thus the flow may be arbitrarily truncated in Fourier space without appreciably impacting the accuracy of the retained harmonics. Additionally, in this case the optimal resolvent mode is a good approximation of the flow and thus retaining only

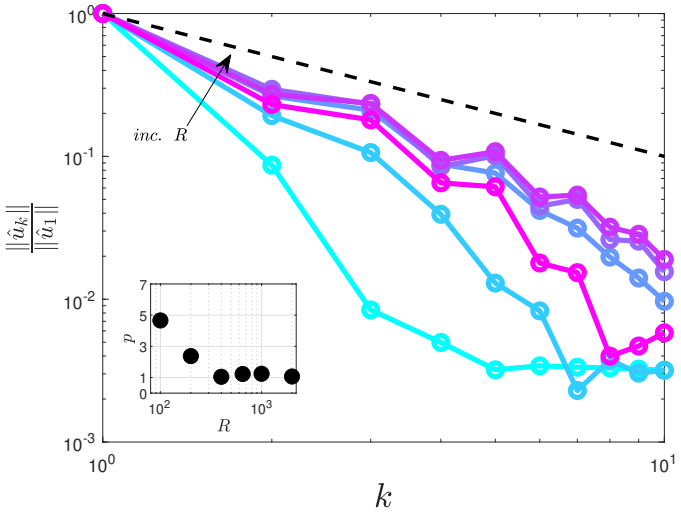

Figure 4.10: Norm of the Fourier modes computed from DNS at $R = 100$, 200, 400, 650, 1000, 2000. Dashed black line is $\sim k^{-1}$. Inset shows exponent of best fit power law as in (4.50). Power law fit performed over the range $1 < k < 5$ for $R = 100$ and $1 < k < 10$ for all $R > 100$.

a single harmonic with $N^1_{SVD} = 2$ and $N^2_{SVD} = 5$ is sufficient to converge to a result whose 2D representation (Figures 4.1 and 4.2) is visually indistinguishable from the DNS. However, we retain more wavenumbers and resolvent modes than this in the results discussed in §4.3 in order to highlight the structure of the nonlinear forcing. At this Reynolds number, the increase in computational cost to do so is trivial.

For the results in the fully nonlinear regime, we focus the discussion here on $R = 400$, with analogous arguments relevant to $R = 200$. To establish a sufficiently converged baseline case from which to reduce the model complexity, we increased N_k and N^k_{SVD} uniformly until the residual no longer decreased appreciably with added degrees of freedom. For $R = 400$, this "full" convergence was achieved with $N_k = 9$ and $N^k_{SVD} = 22$. In Figure 4.11, we plot the expansion coefficients $\sigma_{k,j}\chi_{k,j}$ in (4.15) and the $\chi_{k,j}$ in (4.16). The $\sigma_{k,j}\chi_{k,j}$ and $\chi_{k,j}$ represent the projection of the velocity and nonlinear forcing on to their respective resolvent basis $\psi_{k,j}$ and $\phi_{k,j}$, respectively. We also plot the singular values $\sigma_{k,j}$ on the right y-axis.

Notably, Figure 4.11 indicates that for $k < 5$ the nonlinear forcing has a significant projection onto all of the retained suboptimal modes. This finding is in agreement with Symon et al. (2021) and Morra et al. (2021) who show that the nonlinear forcing has significant projection onto the sub-optimal resolvent forcing modes for a variety of flows even if the resolvent operator is low rank. The former considered both ECS

as well as flow in a minimal channel while the latter focused entirely on turbulent channel flow. In fact, as also observed by Morra et al. (2021), the projection onto the first two forcing modes, $\chi_{k,1}$ and $\chi_{k,2}$, is much lower than the projection onto many of the suboptimal modes.

Furthermore Figure 4.11 reveals that for $k = 1$ the $\sigma_{k,j}\chi_{k,j}$ decrease rapidly with j, while for $k > 1$ there is not only significant projection onto suboptimal modes, up to approximately $j = 10$, but that some of these suboptimal modes have amplitudes of comparable magnitude to the optimal mode, $j = 1$. A lack of roll off in the $\sigma_{k,j}\chi_{k,j}$ despite a steep roll off in $\sigma_{k,j}$ indicates that there is significant structure to the nonlinear forcing. In other words, this means that modes with low linear amplification are amplified by the nonlinear dynamics. If the forcing were unstructured 'white noise,' there would be equal projection onto each $\chi_{k,j}$ and thus the $\sigma_{k,j}\chi_{k,j}$ would decay at the same rate as the singular values $\sigma_{k,j}$, which clearly we do not observe in Figure 4.11. This observation is consistent with the results of §4.3 where it was found that for the higher harmonics, $k \gg 1$, the structure of the nonlinear forcing is paramount to the accurate reconstruction of the velocity field.

Taken together, these results reveal where the basis determined from approximation of the resolvent (rank truncation) leads to an efficient representation of the flow and where approximation of the forcing could lead to further efficiency in the modeling (see also Rosenberg et al. (2019)).

From a practical point of view, we see that for $2 \leq k \leq 4$ the model solution has significant projection onto the majority of the retained singular response modes. The projections of the fundamental ($k = 1$) and the higher harmonics, $k > 4$ generally have decayed to negligible levels for $j \gtrsim 10$. Neglecting these suboptimal modes for the higher harmonics does not affect the accuracy of the solution and the associated 30% reduction in degrees of freedom results in a 90% reduction in computational complexity since cost of computing the 6^{th} order tensors in (4.27) scale as N^6. Neglecting these negligible sub-optimal modes in the higher harmonics we arrive at the final truncation values cited in §4.2, $N^k_{SVD} = 22 \ \forall k \leq 4$, $N^k_{SVD} = 10 \ \forall k > 4$. With this reduction in degrees of freedom the computational complexity has decreased to a point where the optimization may be carried out cheaply on a personal computer. We would like to reiterate that the results presented in §4.3 use these reduced values of N^k_{SVD}. However, if only the large scales are desired or lower levels of convergence are acceptable, the solution is robust to significantly more truncation in both Fourier space and the SVD.

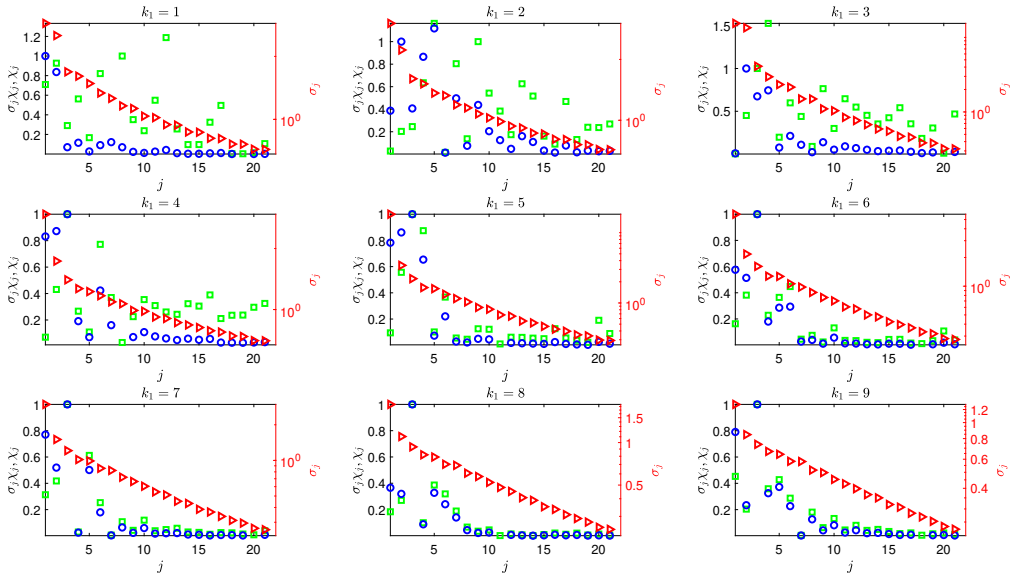

Figure 4.11: Expansion coefficients of the velocity $\sigma_{k,j}\chi_{k,j}$ (blue circles) and nonlinear forcing $\chi_{k,j}$(green squares), and singular values $\sigma_{k,j}$ (red triangles) for $R = 400$. Expansion coefficients are normalized by their maximum value at a given wavenumber and plotted against the left y-axis. Singular values are plotted against the right y-axis. Top row $k = 1 - 3$, middle row $k = 4 - 6$, bottom row: $k = 7 - 9$.

4.4 Efficient Initial Conditions for DNS

It is well known, if not entirely understood, that Taylor vortices persist well into the turbulent regime (Grossmann et al., 2016). While the nature of the Taylor vortices does evolve with increasing Reynolds number as discussed here and Sacco et al. (2019), the general structure does not deviate significantly from the form at $R = 400$ shown in Figures 4.1 and 4.2. Given the significant model reduction achieved by our model, we now investigate whether the large scale Taylor vortex structure can be precomputed using our approach and then used to initialize a DNS at a higher Reynolds number to reduce the time to converge to a statistically stationary state. Similar ideas have been investigated by Rosales and Meneveau (2006), who initialized DNS and LES of isotropic decaying turbulence with both standard Gaussian and more realistic non-Gaussian vector fields. They found that the latter, which displayed some of the physical features associated with turbulence, led to shorter transition times before realistic decay rates were observed.

We performed two sets of DNS of Taylor Couette flow for a range of Reynolds numbers from 400 to 2000: the first using a random perturbation as an initial condition, and a second one using the $R = 400$ model solution as an initial condition. The simulations were run until the torque at the inner and outer cylinder agreed

R	400	650	1000	1500	2000
P	82%	80%	75%	72%	65%

Table 4.3: Percentage reduction in convergence time using model TVF solution as initial condition compared to random perturbation as a function of Reynolds number. All cases use the $R = 400$ model result as an initial condition.

to within 1%. The simulation was then continued for an additional 200 non-dimensional time units at which point the simulation was deemed to be converged. We define the percent reduction in time to convergence between the two cases

$$P \equiv \frac{T_0 - T_m}{T_0} \times 100\% \tag{4.52}$$

where T_0 and T_m are the time required to reach convergence with the random and model initial conditions, respectively. Table 4.3 summarizes the savings for all the Reynolds numbers we considered. As expected the percentage of run time saved decreases as the Reynolds number increases because the Taylor vortices change slightly and, more crucially, because the flow becomes more three-dimensional and time dependent. However, it is remarkable that even at the highest Reynolds number, $R = 2000$, which is five times the Reynolds number of the model used as an initial condition, the run time is reduced by 65%. Physically, this finding speaks to the robustness of the Taylor vortices, a phenomenon which has been observed by a host of authors (Grossmann et al., 2016). However, we acknowledge that the practical relevance of this finding may be limited. When computing a flow for a range of Reynolds numbers, one would only need to initialize the lowest Reynolds number case with a random perturbation and then simply initialize subsequent cases with the final state of the previous simulation.

4.5 Summary

In this chapter, we have presented a fully nonlinear reduced order model of Taylor vortex flow for Reynolds numbers up to five times greater than the critical value. The resolvent formulation allows the governing equations for the fluctuations about a known mean velocity to be transformed into a set of polynomial equations. We approximate the solution to these equations by minimizing their associated residual in conjunction with a constraint which ensures the model generates Reynolds stresses compatible with the input mean velocity profile. We are able to generate model solutions which solve the NSE to a very good approximation and replicate the flow field computed through DNS at a tiny fraction of the computational cost. We believe this is the first explicit example of "closing the resolvent loop" published

in the literature, although Rosenberg (2018) presented a similar analysis applied to ECS in a channel in his doctoral thesis which inspired this work.

We analyzed the nonlinear interactions driving the flow for a range of Reynolds numbers and identified the transition from a weakly nonlinear regime close to the bifurcation from the laminar state where the structure of the flow is accurately modeled by the linear dynamics and the forcing cascade is purely from large scales to small scales. At higher Reynolds numbers, we define a fully nonlinear regime where an inverse forcing cascade from small to large scales emerges to counter the cascade from large to small scales. In this regime, the dominant nonlinear interactions at a given wavenumber k involve the pair of triadic interactions $k = (k \pm 1) \mp 1$, with the pair of triads $k = (k \pm 2) \mp 2$ also emerging as a dominant forcing mechanism for the highest Reynolds number case. The velocity contributions from these pairs of triads have opposite sign and almost equal amplitudes which are much larger than the full Fourier mode. Their sum results in significant destructive interference with the small differences in shape giving rise to the shape of the full Fourier mode. We demonstrated that this destructive interference is a direct consequence of the structure of the nonlinear term of the NSE formulated in Fourier space. Furthermore, this bidirectional forcing cascade implies that in order to accurately model a flow up to a certain order in Fourier space significantly more harmonics than desired must be retained in order to capture this inverse forcing cascade. We postulated that this shift from linear/weakly nonlinear to fully nonlinear dynamics is related to a similar transition in the physics of Taylor vortices observed by Sacco et al. (2019). Finally, we used our model solution as an initial condition to DNS of TCF at higher Reynolds numbers and were able to significantly reduce the time to convergence compared to initializing the simulation with a random perturbation.

Chapter 5

MEAN VELOCITY PREDICTION IN SUPERCRITICAL TAYLOR COUETTE FLOW

5.1 Introduction

One inherent limitation of resolvent-based models is the reliance on the a priori knowledge of the mean velocity profile from DNS or experimental data. Here we present a method to predict the shape of the mean velocity profile in supercritical Taylor Couette flow in order to circumvent this reliance for the model described in Chapter 4. The main idea is to iteratively converge to a mean flow generated by the Reynolds stress divergence of its own leading resolvent mode. Such iterative methods have been used previously in computing exact coherent states by Beaume et al. (2015) and Rosenberg and McKeon (2019a) as well as by Mantič-Lugo et al. (2014, 2015) abd Gallaire et al. (2016) who used such methods to accurately model the shedding frequency and mean flow of super-critical cylinder flow. One caveat of such methods is that they require the amplitude of the leading resolvent or eigen mode as an input. Mantič-Lugo et al. (2015) circumvent this requirement by actively adjusting this amplitude throughout the iteration by noting that in physical flows the mean profile tends to a state of neutral stability. Here we take a different approach, and instead use a weakly nonlinear analysis to derive the equilibrium amplitude of the dominant flow structure (in this case the Taylor vortex) as a function of Reynolds number.

5.2 Derivation of the Stuart Landau Equation

The prediction of the mean flow requires knowledge of the amplitude of the Taylor vortex at the bifurcation from the laminar state. This amplitude is given by the equilibrium solution of the Stuart-Landau equation, which governs the slowly varying amplitude of a weakly supercritical disturbance (Stuart, 1958; Watson, 1960). Related methods have been applied to Taylor Couette flow by several authors such as Stuart (1960); Davey (1962); Yahata (1977); Zuccoli and Auteri (2019) to name just a few. We briefly outline the derivation here, and refer the reader to the references cited above for a more comprehensive discussion.

We begin with the incompressible Navier Stokes equations.

$$\frac{\partial \mathbf{u}}{\partial t} + \mathbf{u} \cdot \nabla \mathbf{u} - \frac{1}{R}\nabla^2 \mathbf{u} - \nabla p = 0 \tag{5.1}$$

$$\nabla \cdot \mathbf{u} = 0. \tag{5.2}$$

The flow undergoes a super-critical bifurcation from the laminar state to the steady, axisymmetric, and axially periodic Taylor vortex state at a critical Reynolds number R_c. We aim to derive the amplitude of these Taylor vortices for Reynolds numbers near this critical point. To this end, we add and subtract $\frac{1}{R_c}\nabla^2 \mathbf{u}$ from (5.1).

$$\frac{\partial \mathbf{u}}{\partial t} + \mathbf{u} \cdot \nabla \mathbf{u} - \frac{1}{R_c}\nabla^2 \mathbf{u} + \left(\frac{1}{R_c} - \frac{1}{R}\right)\nabla^2 \mathbf{u} - \nabla p = 0 \tag{5.3}$$

We are interested in Reynolds numbers close to the critical point, i.e. R such that $\frac{1}{R_c} - \frac{1}{R} \ll 1$. We will employ the method of multiple scales and thus we introduce the small parameter $\epsilon^2 \equiv \frac{1}{R_c} - \frac{1}{R}$, and a long time scale $T = \epsilon^2 t$. This particular choice of bifurcation parameter ϵ is natural given the form of the equations and was also shown by Gallaire et al. (2016) to extend the range of validity of the resulting asymptotic expansions over those found using the more traditional $\epsilon'^2 = (R - R_c)R_c^{-2}$, which is actually an approximation of the former. The governing equations then take the form

$$\frac{\partial \mathbf{u}}{\partial t} + \epsilon^2 \frac{\partial \mathbf{u}}{\partial T} + \mathbf{u} \cdot \nabla \mathbf{u} - \frac{1}{R_c}\nabla^2 \mathbf{u} + \epsilon^2 \nabla^2 \mathbf{u} - \nabla p = 0. \tag{5.4}$$

We expand the state $\mathbf{q} \equiv [\mathbf{u}, p]$ in an asymptotic series

$$\mathbf{q} = \mathbf{q}_0 + \epsilon \mathbf{q}_1 + \epsilon^2 \mathbf{q}_2 + \epsilon^3 \mathbf{q}_3 + O(\epsilon^4). \tag{5.5}$$

Plugging the expansion (5.5) into (5.4) and gathering terms of $O(1)$, we find

$$\frac{\partial \mathbf{u}_0}{\partial t} + \mathbf{u}_0 \cdot \nabla \mathbf{u}_0 - \frac{1}{R_c}\nabla^2 \mathbf{u}_0 - \nabla p_0 = 0. \tag{5.6}$$

This is simply the NSE at the critical Reynolds number and thus we identify the solution $\mathbf{u}_0$ as the laminar solution.

$$\mathbf{u}_0 = A(\eta) r + \frac{B(\eta)}{r} \tag{5.7}$$

At $O(\epsilon)$, we find

$$\frac{\partial \mathbf{u}_1}{\partial t} + \mathbf{u}_0 \cdot \nabla \mathbf{u}_1 + \mathbf{u}_1 \cdot \nabla \mathbf{u}_0 - \frac{1}{R_c}\nabla^2 \mathbf{u}_1 - \nabla p_1 = 0, \tag{5.8}$$

which we identify as the NSE linearized about the laminar base flow $\mathbf{u}_0$. In order to simplify the notation going forward, we denote this operator as L defined as

$$\mathbf{L}() = \begin{bmatrix} \frac{\partial}{\partial t} + \mathbf{u}_0 \cdot \nabla() + () \cdot \nabla \mathbf{u}_0 - \frac{1}{R_c}\nabla^2() - \nabla p_1 & 0 \\ 0 & \nabla() \end{bmatrix} \tag{5.9}$$

such that

$$\mathbf{L}([\mathbf{u}_1, p_1]^T) = 0. \tag{5.10}$$

We postulate that $\mathbf{u}_1$ is of the form

$$\mathbf{u}_1 = A(T)\boldsymbol{\psi}_1(r)e^{i(kz-\omega t)} + A^*(T)\boldsymbol{\psi}_1^*(r)e^{-i(kz-\omega t)}, \tag{5.11}$$

$$p_1 = A(T)p_1(r)e^{i(kz-\omega t)} + A^*(T)p_1^*(r)e^{-i(kz-\omega t)}, \tag{5.12}$$

where the superscript $*$ denotes the complex conjugate, $A(T)$ represents the slowly varying amplitude, and $[\boldsymbol{\psi_1}(r), p_1(r)]$ represents the radially varying mode shape, which we take to be given by the critical eigenmode of the Navier-Stokes operator linearized about the laminar base flow at $R = R_c$, normalized such that $||\boldsymbol{\psi}_1||_{L_2} = 1$. The frequency ω is the imaginary part of the eigenvalue $\lambda = 0 + i\omega$ at critically (in our case $\omega = 0$).

Continuing on to $O(\epsilon^2)$, we find

$$\mathbf{L}([\mathbf{u}_2, p_2]^T) = [-\mathbf{u}_1 \cdot \nabla \mathbf{u}_1 - \frac{1}{R_c}\nabla^2 \mathbf{u}_0 - \frac{\partial \mathbf{u}_0}{\partial T},\ \ 0]^T, \tag{5.13}$$

which simplifies to

$$\mathbf{L}([\mathbf{u}_2, p_2]^T) = [-\mathbf{u}_1 \cdot \nabla \mathbf{u}_1,\ \ 0]^T. \tag{5.14}$$

Plugging the ansatz for the form of $\mathbf{u}_1$ given by (5.11) into the right hand side of (5.14), we find

$$\begin{aligned} \mathbf{L}([\mathbf{u}_2, p_s]^T) = -[&A^2\boldsymbol{\psi}_1 \cdot \nabla_{+1}\boldsymbol{\psi}_1 e^{2ik_z z} + A^{*2}\boldsymbol{\psi}_1^* \cdot \nabla_{-1}\boldsymbol{\psi}_1^* e^{-2ik_z z} \\ &+ |A|^2 \left(\boldsymbol{\psi}_1 \cdot \nabla_{-1}\boldsymbol{\psi}_1^* + \boldsymbol{\psi}_1^* \cdot \nabla_{+1}\boldsymbol{\psi}_1\right),\ \ 0]^T. \end{aligned} \tag{5.15}$$

The gradient operator $\nabla_{\pm j}$ and LNS operator $\mathbf{L}_{\pm j}$ are defined here and going forward such that the spanwise (axial) derivative takes the form

$$\frac{\partial}{\partial z} = \pm ijk. \tag{5.16}$$

We note that the right hand side of (5.15) includes spanwise (axially) constant terms as well as terms proportional to $e^{\pm 2ikz}$. Therefore we postulate that at this order, the solution takes the form

$$\mathbf{u}_2 = A(T)^2\boldsymbol{\psi}_2(r)e^{2i(kz-\omega t)} + A^{*2}(T)\boldsymbol{\psi}_2^*(r)e^{-2i(kz-\omega t)} + |A_1|^2\mathbf{u}_2^0(r) \tag{5.17}$$

$$p_2 = A(T)^2 p_2(r) e^{2i(kz-\omega t)} + A^{*2}(T) p_2^*(r) e^{-2i(kz-\omega t)} + |A_1|^2 p_2^0(r). \tag{5.18}$$

Considering first the terms proportional to $e^{\pm 2ik_z z}$, we find

$$\mathbf{L}_2([\boldsymbol{\psi}_2, p_2]^T) = -[\boldsymbol{\psi}_1 \cdot \nabla_{+1}\boldsymbol{\psi}_1,\ \ 0]^T \tag{5.19}$$

$$[\boldsymbol{\psi}_2, p_2]^T = -\mathbf{H}_2[\boldsymbol{\psi}_1 \cdot \nabla_{+1}\boldsymbol{\psi}_1,\ \ 0]^T. \tag{5.20}$$

where $\mathbf{H} \equiv \mathbf{L}^{-1}$ is the resolvent operator. Examining next the terms proportional to e^0 we find

$$\mathbf{L}_0([\mathbf{u}_2^0, P_2^0]^T) = -[\left(\boldsymbol{\psi}_1 \cdot \nabla_{-1}\boldsymbol{\psi}_1^* + \boldsymbol{\psi}_1^* \cdot \nabla_{+1}\boldsymbol{\psi}_1\right),\ \ 0]^T \tag{5.21}$$

$$-\frac{1}{R_c}\nabla^2 \mathbf{u}_2^0 = -\left(\boldsymbol{\psi}_1 \cdot \nabla_{-1}\boldsymbol{\psi}_1^* + \boldsymbol{\psi}_1^* \cdot \nabla_{+1}\boldsymbol{\psi}_1\right). \tag{5.22}$$

Thus we identify $\boldsymbol{\psi}_2$ as the parasitic mode forced by $\boldsymbol{\psi}_1$, and $\mathbf{u}_2^0$ as the mean flow correction induced by the self interaction of $\boldsymbol{\psi}_1$.

Finally we consider the solution at $O(\epsilon^3)$. Here we will find the appearance of secular terms on the right hand side requiring a solvability condition which will lead to a Stuart-Landau type equation for the slowly varying amplitude $A(T)$. Grouping terms of $O(\epsilon^3)$ in system (5.4, 5.5), we find

$$\mathbf{L}([\mathbf{u}_3, p_3]^T) = [-\mathbf{u}_1 \cdot \nabla \mathbf{u}_2 - \mathbf{u}_2 \cdot \nabla \mathbf{u}_1 - \frac{1}{R_c}\nabla^2 \mathbf{u}_1 - \frac{\partial \mathbf{u}_1}{\partial T},\ \ 0]^T. \tag{5.23}$$

The solvability condition is found by gathering the terms proportional to $e^{ik_z z}$, which are given by

$$\boldsymbol{\psi}_1 \frac{\partial A}{\partial T} + \frac{1}{R_c}\nabla^2 \boldsymbol{\psi}_1 A + \left(\boldsymbol{\psi}_1 \cdot \nabla_0 \mathbf{u}_2^0 + \boldsymbol{U}_2^0 \cdot \nabla_{+1}\boldsymbol{\psi}_1 + \boldsymbol{\psi}_1^* \cdot \nabla_{+2}\boldsymbol{\psi}_2 + \boldsymbol{\psi}_2 \cdot \nabla_{-1}\boldsymbol{\psi}_1^*\right) A|A|^2. \tag{5.24}$$

The Fredholm alternative requires that this right hand side forcing term be orthogonal to the adjoint of the homogeneous solution: $\boldsymbol{\psi}^\dagger$ which is found by solving the adjoint LNS system

$$\mathbf{L}^\dagger([\boldsymbol{\psi}^\dagger, p^\dagger]) = 0, \qquad ||\boldsymbol{\psi}^\dagger||_{L_2} = 1. \tag{5.25}$$

Projecting (5.24) onto the adjoint eigenmode $\boldsymbol{\psi}^\dagger$ and integrating across the domain results in the Landau equation for the slowly varying amplitude $A(T)$

$$a_1 \frac{\partial A}{\partial T} + a_2 A + \kappa A|A|^2 = 0. \tag{5.26}$$

The coefficients are given by

$$a_1 = \langle \boldsymbol{\psi}_1^H \boldsymbol{\psi}_1 \rangle_{L_2} \tag{5.27}$$

$$a_2 = \langle \boldsymbol{\psi}_1^H \nabla^2 \boldsymbol{\psi}_1 \rangle_{L_2} \tag{5.28}$$

$$\kappa = \langle \boldsymbol{\psi}_1^H \left(\boldsymbol{\psi}_1 \cdot \nabla_0 \mathbf{u}_2^0 + \boldsymbol{U}_2^0 \cdot \nabla_{+1} \boldsymbol{\psi}_1 + \boldsymbol{\psi}_1^* \cdot \nabla_{+2} \boldsymbol{\psi}_2 + \boldsymbol{\psi}_2 \cdot \nabla_{-1} \boldsymbol{\psi}_1^* \right) \rangle_{L_2}. \tag{5.29}$$

The saturation value of the amplitude function $A(T; k, R)$ is then given by

$$A_e^2(k, R) = -\frac{a_2}{\kappa}. \tag{5.30}$$

Therefore the amplitude of the flow structure is given by

$$||\epsilon \mathbf{u}_1||^2 = \mathcal{A}^2 \equiv \epsilon^2 A_e^2 = -\frac{a_2}{\kappa} \epsilon^2 = -\frac{a_2}{\kappa} \left(\frac{1}{R_c} - \frac{1}{R} \right). \tag{5.31}$$

This gives us a means to calculate the amplitude for our mean flow iteration scheme.

5.3 Axial Wavenumber

Since the amplitude equation is formally an expansion about a super critical Hopf bifurcation, the mathematically rigorous choice of axial (spanwise) wave number k for the amplitude equation (5.30) is the critical wave number $k_c \approx \pi$ predicted by linear stability. However, for the resolvent modes computed during the iterative scheme using this critical wave number proves to be a poor choice. The underlying assumption on which the iterative scheme relies is the accuracy of the rank 1 approximation of the Reynolds stress divergence. Therefore it is advantageous to choose a wave number which maximizes the accuracy of this approximation at a given Reynolds number. We would like to choose a k that maximizes the singular value separation quantified by σ_1/σ_2 or some other suitable metric which quantifies the "low rankness" of the system dynamics. More specifically, we desire some some exponent α such that $k^* \sim R^\alpha$ maximizes σ_1/σ_2. Currently a rigorous theoretical prediction for such a power law is still outstanding, however an analysis using mean velocity profiles from DNS suggests that such a scaling exists. In fact at each Reynolds number there is in general a multiplicity of local maxima of $\sigma_1(k)$. Figure 5.1 shows both the largest and smallest most low rank (or equivalently most amplified) wave numbers as a function of the Reynolds number. The smallest amplified k represents the size of the most linearly amplified large structure. The size of this most amplified large structure is found to scale (approximately) as $R^{-0.55}$. Therefore we choose the wave number k in our iterative scheme according to the power law

$$k = 3.1 \left(\frac{R}{R_c} \right)^{-0.55}. \tag{5.32}$$

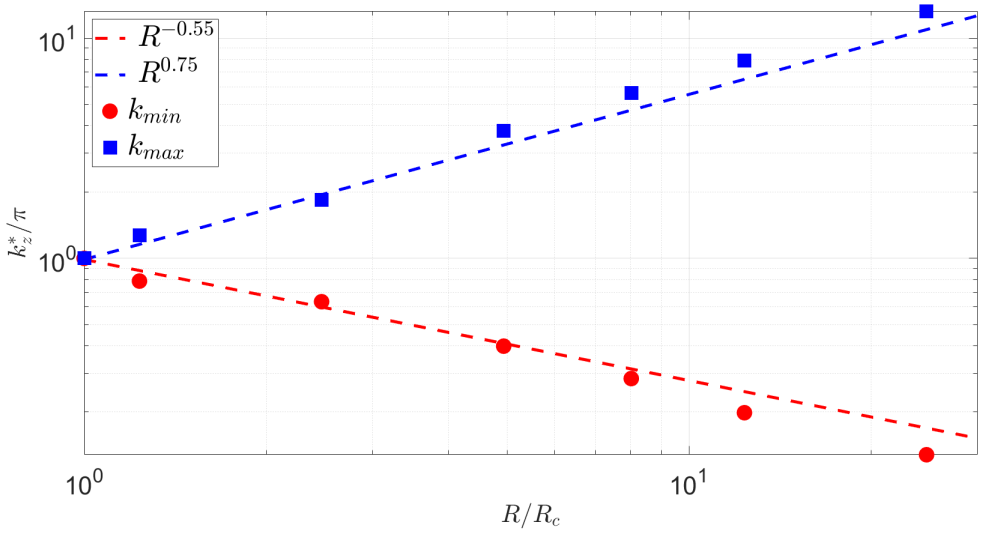

Figure 5.1: Axial wave numbers which maximize the singular value separation of the resolvent operator at a given Reynolds number.

We do not view this empirically determined power law as a major detracting factor from our model since the same result could be attained by simply performing a sweep over the local Fourier space at each iteration. Thus (5.32) simply allows us to bypass such a computationally expensive step in the iterative process. We acknowledge that choosing the optimal wavenumber (5.32) is somewhat inconsistent with the derivation of the amplitude which uses the critical wave number. However, we view this as a necessary and justified compromise between consistency and practicality.

5.4 Self Sustaining Mean Flow Iteration

The primary challenge of applying this iterative algorithm to the Taylor Couette geometry is the lack of wall normal symmetry in the cylindrical coordinate system. In the case of plane Couette flow, defined in a Cartesian coordinate system, the underlying equations are invariant with respect to reflection about the center of the channel. This results in resolvent modes which are either even or odd about the center line. The NSE in the cylindrical geometry of Taylor Couette flow do not exhibit this same explicit symmetry for Reynolds numbers $R >\sim 100$. Despite the lack of symmetry in the governing equations, the actual solution observed in Taylor Couette flow does roughly exhibit these symmetries. In order to account for this observation, we introduce the following symmetrizing scheme to more accurately capture the physical structure of the TVF.

$$\psi_1 = [u_r(r), u_\theta(r), u_z(r)] \rightarrow \psi_{1,sym} = [u_r(r), (u_\theta(r) + u_\theta(r - \overline{r})), u_z(r)] \tag{5.33}$$

The symmetrized mode is normalized such that $||\psi_{1,sym}||_{L_2} = 1$. Additionally, we introduce a relaxation parameter suggested by Mantič-Lugo et al. (2015) which improves the convergence properties of the algorithm. The iterative algorithm then proceeds as follows, where γ is the relaxation parameter which following Mantič-Lugo et al. (2015) is fixed at $\gamma = 0.5$.

- Calculate amplitude $\mathcal{A}(k_c, R_c)$ from (5.31)
- Set initial condition to laminar base flow $U_0 = U_{lam}$

1. Construct resolvent operator from current iterate U_j, Reynolds number R, and wave number $k(R)$.
2. Symmetrize leading resolvent mode according to (5.33).
3. Compute $f_0 = -\mathcal{A}^2 \nabla \cdot (\psi_1 \psi_1^*)$.
4. Compute mean flow correction: $\nabla^2 U_{new} = f_0$.
5. Update mean flow $U_{j+1} = \gamma U_{new} + (1 - \gamma) U_j$.
6. Iterate until convergence.

5.5 Results

Figure 5.2 compares the result of the iterative scheme for $R = 100$ and $R = 200$ to mean velocity profiles calculated from DNS. These values correspond to approximately 1.25 and 2.5 times the critical Reynolds number: $R_c = 81$. In each case, the input amplitude and wave number are set by (5.31) and (5.32) respectively. While the agreement is not perfect, our model captures the shape of the mean velocity profile remarkably well in both cases. The scheme converges to the results shown in 4 iterations for both $R = 100$ and $R = 200$. However, we note that the convergence can be improved by initializing higher Reynolds number cases with the results from models at lower Reynolds numbers. Finally, we note that unlike the work of Mantič-Lugo et al. (2015), we do not enforce the neutral stability of the mean flow, however our results are observed to be approximately neutrally stable.

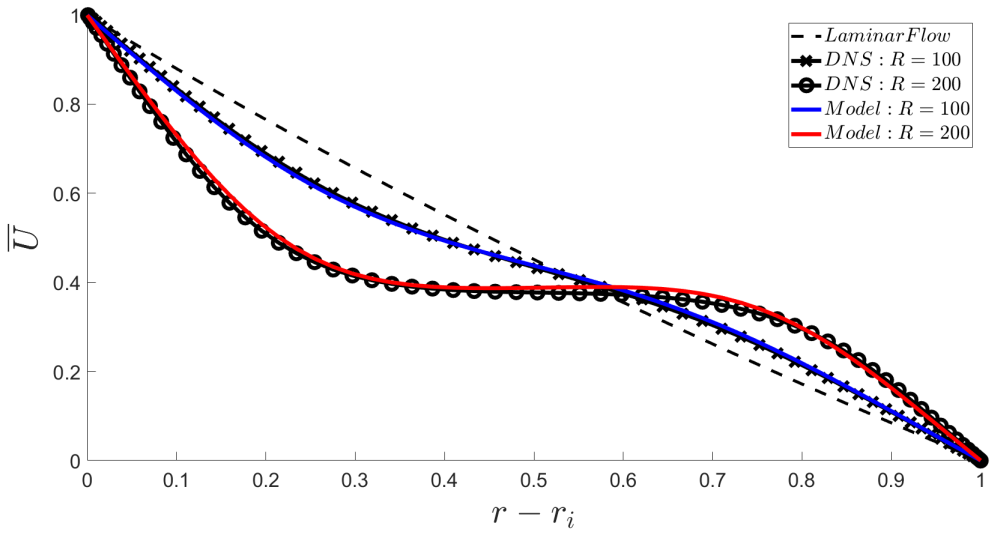

Figure 5.2: Mean velocity profile computed from self sustaining model (color) and DNS (black).

5.6 Wave Number Amplification Mechanism

Here we speculate on some physical mechanism which could be leading to the preferential linear amplification of wave numbers $k \sim R^{-0.55}$ observed in figure 5.1. The first question to ask is *what does linear amplification actually mean?* Since we are interested in steady TVF, we evaluate the resolvent operator at $\omega = 0$. Therefore a peak in the norm of the resolvent operator is indicative of the linearized NS operator having an eigenvalue, λ, close to zero, since $||H|| = \sigma_1 \rightarrow \infty$ as $\omega \rightarrow \lambda_j \ \ \forall j$. Therefore the task is to find the minimum $k(R)$ s.t. $||\mathbf{L}(R, k(R))||$ is minimized. We search for the smallest minimizing k since $||\mathbf{L}(k)||$ has multiple peaks for a given Reynolds number. Or more formally,

$$\begin{aligned} \min_{k \in \mathbb{R}} \quad & k^2, |\lambda(k, R)| \\ \text{s.t.} \quad & \mathbf{L}(k, R)\mathbf{q} = \lambda(k, R)\mathbf{q} \\ & \boldsymbol{q}(r_i) = \boldsymbol{q}(r_o) = 0. \end{aligned} \tag{5.34}$$

The tricky thing is that the linear operator $\mathbf{L}(k, R)$ depends on the mean velocity profile $\overline{U}(r; R)$ which is unknown. Therefore some physically motivated approximation of the mean velocity will be required to make progress. Furthermore, we know from analyzing the DNS mean velocity profiles that the number of peaks in $\sigma_1(k, R)$ increases with increasing Reynolds number, and we do not fully understand why.

The amplification mechanism we observe is solely a function of the linearized Navier

Stokes operator, which depends on k, R, and $\overline{U}(r;R)$. Therefore the dependence of the most amplified k as a function of R arises either due to R^{-1} appearing in the operator or due to the shape of the mean velocity profile changing with Reynolds number.

First we consider the hypothesis that it is the mean velocity profile which determines the scaling of the most amplified wave number. This view is supported by the observation that if the mean velocity $\overline{U}$ in the resolvent operator is replaced by the laminar base flow U_0 we do not observe the same power law (5.32) and instead observe a power law closer to $R^{-4/3}$.

Let us imagine the mean velocity profile as being comprised of two distinct regions as discussed by Ostilla et al. (2013), or Cheng et al. (2020). In this view, we have a bulk region in the center of the domain where the mean angular velocity $\overline{\Omega} \equiv \overline{U}/r$ is approximately constant and two boundary layers at the walls. Examining the mean velocity profiles in Figure 5.2, we see that while near criticality, at $R = 100$ this is a poor approximation, it is a plausible model for at least $R \geq 200$ where we do see a flat region in the center of the mean velocity profile. It is known from several studies such as Eckhardt et al. (2007); Ostilla-Mónico et al. (2014b); Sacco et al. (2019) that at the Reynolds numbers considered here the boundary layers are laminar, and therefore their height scales like $R^{-0.5}$. Therefore one could imagine that the observation that $k^* \sim R^{-0.5}$ arises due to a balance with the boundary layer thickness.

Alternatively, we may neglect the Reynolds number dependence of the mean velocity profile, and investigate the affect of the explicit Reynolds number dependence of the resolvent operator. The pressure may be eliminated from the governing equations to write the system in terms of u_r and u_θ. The resulting linear operator is then

$$\mathbf{L} = \begin{bmatrix} -\frac{1}{R}\nabla^4 & \frac{2k^2\overline{U}}{r} \\ \frac{1}{r}\frac{\partial}{\partial r}\left(r\overline{U}\right) & -\frac{1}{R}\nabla^2 \end{bmatrix}, \tag{5.35}$$

where $\nabla^2 \equiv \frac{\partial^2}{\partial r^2} + \frac{1}{r}\frac{\partial}{\partial r} - \frac{1}{r^2} - k^2$. Numerical tests imply that we can approximate the Laplacian as $\nabla^2 \approx \frac{\partial^2}{\partial r^2}$. This is reasonable since we expect k to decrease with Reynolds number and therefore we expect the radial derivatives to dominate. With this approximation, the linear operator is then

$$\mathbf{L} = \begin{bmatrix} -\frac{1}{R}\frac{\partial^4}{\partial r^4} & \frac{2k^2\overline{U}}{r} \\ \frac{1}{r}\frac{\partial}{\partial r}\left(r\overline{U}\right) & -\frac{1}{R}\frac{\partial^2}{\partial r^2} \end{bmatrix}. \tag{5.36}$$

We can derive the wave number scaling which minimizes the operator norm of this approximate $\mathbf{L}$ which corresponds to the maximization of the leading singular value of $\mathbf{H} = \mathbf{L}^{-1}$.

Consider a trial function $\psi = [u_r, u_\theta]$. The norm of $L\psi$ is then given by

$$||L\psi||^2 = A_1 R^{-2} + A_2 R^{-1} k^2 + A_3 k^4 + A_4 R^{-1} + A_5, \tag{5.37}$$

where the A_j are Reynolds number independent integrals involving r, ψ, and $\overline{U}$. Setting the derivative of this expression with respect to k equal to zero, we find

$$\frac{\partial}{\partial k}||L\psi||^2 = 2A_2 R^{-1} k + 4A_3 k^3 = 0. \tag{5.38}$$

This implies that the minimizing wave number k^* is given by

$$k^{*2} = -\frac{2A_2}{4A_3}\frac{1}{R}. \tag{5.39}$$

The optimal wavenumber therefore scales as $k^* \sim R^{-0.5}$. This result is consistent with the scaling of $R^{-0.55}$ for the smallest most amplified wave number observed numerically in Figure 5.1. Of course this derivation neglected the wavenumber dependence of the Laplacian operator as well as the wave number dependence of the resolvent modes, and is therefore not a mathematically rigorous analysis. We speculate that the multiplicity of peaks in the $\sigma_1(k, R)$ curves seen in Figure 5.1 could potentially be accounted for by the neglected k dependent terms in the Laplacian. However, a rigorous higher order analysis is beyond the scope of this thesis.

5.7 Summary

In this chapter, we have extended the self-consistent mean flow prediction algorithm described in Mantič-Lugo et al. (2014, 2015); Rosenberg and McKeon (2019a) to Taylor-Couette flow. As with those studies, the method described here starts from the laminar base flow and iteratively generates a mean flow sustained by the Reynolds stress of its own leading resolvent mode. However, unlike these previous studies, we preform an asymptotic expansion about the critical Reynolds number to derive the equilibrium amplitude of this Reynolds stress. A further contribution of this thesis is the extension to the cylindrical coordinate system relevant to TC flow. This leads to the loss of wall normal symmetry of the governing equations present in the Cartesian system. The challenge is that solutions observed in TC flow are (roughly) symmetric about the center line, and the resolvent basis (computed

from the non-symmetric equations) is not. To account for this, we have introduced a step into the algorithm which enforces the symmetry about the center line of the streamwise component of the leading resolvent mode at each iteration. The results of our method compare favorably to the mean velocity profiles computed from DNS for Reynolds numbers up to 2.5 times the critical Reynolds number. Extending this strategy to higher Reynolds number and deriving a mathematically rigorous approach to enforcing the wall normal symmetry is the topic of ongoing research.

Chapter 6

PHASE RECONSTRUCTION FROM TURBULENT SPECTRA

6.1 Introduction

In Chapter 4, we described exact representations of nonlinear, yet still relatively low dimensional solutions. However, most flows of practical interest are high dimensional and not amenable to such modeling strategies. One avenue for progress in the modeling of these more complex flows is the reconstruction of high dimensional representations of the solution from knowledge of lower dimensional representations. As an analogy, consider the concept of data compression. High dimensional data, such as a high resolution image, are compressed (often through SVD-based algorithms) for more efficient storage and transmission and then reconstructed using a second algorithm prior to use. Such data driven and machine learning-based techniques have already become popular, if not widespread in the field of fluid mechanics, often replacing the consideration of the governing equations entirely (Taira et al., 2017; Brenner et al., 2019; Kochkov et al., 2021; Brunton, 2021; Herrmann et al., 2021). While such techniques are powerful and have the potential to revolutionize all of physics, we believe that the governing equations have not taught us everything they have to give just yet.

Lower order statistics like the mean and spectrum can be thought of as "compressed" forms of the high dimensional flow data. Unfortunately, as yet a general decompression algorithm to reconstruct the full flow field from these statistics remains elusive. Nevertheless these zeroth order (mean) and first order (spectrum) moments of the velocity field are well studied and relatively well understood. The mean velocity profile is the most studied, and for high Reynolds numbers is known to satisfy a logarithmic profile that scales with Reynolds number. Resolvent analysis itself can be thought of a type of "data decompression" in the sense that it extracts linearly amplified structures of the fluctuation field from the mean velocity profile. The velocity spectrum is also well studied. The most famous result in this regard is that homogeneous, isotropic turbulence satisfies the $k^{-5/3}$ velocity spectrum (Pope, 2000). For wall bounded turbulent flows, several models for the shape of the spectrum have been proposed, the most famous of which being the attached eddy hypothesis suggested by Townsend (1951, 1961, 1980) and recently summarized by Marusic and Monty

(2019). Furthermore, years of numerical and experimental research have lead to significant empirical insight into the qualitative and quantitative characteristics of the turbulent spectrum (Álamo et al., 2004; Smits et al., 2011). For example, the velocity spectrum is known to exhibit a two-peaked structure corresponding to the "near-wall cycle" and the "very-large scale structures" observed in the wake region (Mathis et al., 2009).

At sufficiently high Reynolds numbers the mean velocity and velocity spectrum scale with Reynolds number, implying that we can predict (with reasonable certainty) their behaviour at a given Reynolds number from data at a lower Reynolds number. If one could derive a transformation (decompression) from the first order moment, the velocity spectrum, to higher order moments, one could in principle extend our predictive capabilities to higher order moments, such as the cross spectral density or skewness, where often the Reynolds number scaling behaviour is less well understood. In the context of turbulent flows, such a transformation is equivalent to the reconstruction of the phase information lost in the compression of the full velocity field to the energy spectrum. While the off-diagonal terms of the velocity spectrum tensor, known as the cross spectral density, contains some phase information of a particular Fourier mode, it does not encode the phase shift between Fourier modes. Some studies such as Zare et al. (2017) have used the stochastically forced NSE to predict second order statistics in turbulent channel flow, however a comprehensive framework for the prediction of higher order moments remains elusive.

It has been showed by a variety of authors that these phase shifts between Fourier modes (structures) play a significant role in the physics of turbulent flows. Of particular interest has been the interaction between very large scale motions (VLSM's) whose size is greater than the boundary layer, and the small scale motions which make up the near wall cycle. It has been established that the primary mechanism in this interaction is the amplitude modulation of the near wall small scales by the very large scales (Hutchins and Marusic, 2007a,b; Mathis et al., 2009). Experimental evidence has shown that this amplitude modulation strongly resembles the skewness profile (third moment) of the velocity (Schlatter and Örlü, 2010b; Mathis et al., 2011). The only information contained in the skewness not contained in the spectrum is the relative phase shifts between the large and small scales. This implies that the amplitude modulation of the near wall cycle is related to these phase shifts. Jacobi et al. (2021) developed a resolvent analysis-based model to interaction between a single large scale and the small scale turbulent fluctuations characterized by the

Reynolds stresses. They found that the wall normal location where the amplitude modulation coincides with the critical layer location of the large scale structure, indicating a relative phase shift of $-\pi/2$ between the turbulent fluctuations and the large scale.

In this chapter, we propose a purely equations-driven algorithm for the reconstruction of this lost phase information based on an observation made by Schmid and Henningson (2001) that the nonlinearity of the NSE is not only globally energy conserving but also on the level of an individual triad. Throughout this chapter, the quantity $a \in [-\pi, \pi]$ refers to the phase of a complex number.

6.2 Phase Reconstruction from Spectra

Consider a doubly periodic simulation of a wall bounded shear flow on the domain $x \in [0, L_x]$, $y \in [-1, 1]$, and $z \in [0, L_z]$, which is statistically stationary and homogeneous in the streamwise, x, and spanwise, z, directions. Such a flow may be expanded in a Fourier series

$$\mathbf{u}(\mathbf{x}, y, t) = \sum_{\mathbf{k}} \hat{\mathbf{u}}_{\mathbf{k}}(y) e^{i\mathbf{k}\cdot\mathbf{x}} + c.c. \tag{6.1}$$

where $\mathbf{x} \equiv [x, z, t]$ and $\mathbf{k} = [k_x, k_z, \omega]$. The three-dimensional energy spectrum is defined as

$$E(y; \mathbf{k}) = \hat{\mathbf{u}}_{\mathbf{k}}(y)\hat{\mathbf{u}}^*_{\mathbf{k}}(y) \tag{6.2}$$

and represents the wall normal kinetic energy distribution at a given length and time scale. The energy spectrum which encodes only the kinetic energy provides no information on either the wall normal phase variation of the Fourier modes nor the relative phase shifts between the Fourier modes. While studies such as Jacobi et al. (2021) have proposed models for the prediction of these phase shifts, a comprehensive understanding remains outstanding.

Here we propose an algorithm for the reconstruction of the phase information from solely knowledge of the spectrum. The algorithm is based on the optimization-based resolvent reconstruction of the spectrum developed by Moarref et al. (2014a); McMullen et al. (2020) and an observation made by Schmid and Henningson (2001) that individual triads of Fourier modes are energy conserving. The former reconstructs the time averaged velocity spectrum as an expansion in resolvent modes, thereby recovering (an approximation) of the wall normal phase variation of the full Fourier modes. The latter allows us to recover the relative phase shift between the Fourier modes.

6.3 Spectrum Optimization

We adopt the optimization framework introduced by Moarref et al. (2014a) and improved upon by McMullen et al. (2020) which minimizes the differences between the time averaged spectra from DNS and those computed from an expansion in resolvent modes. The resolvent three-dimensional spectra may be written as

$$E_r\left(y;k_x,k_z,\omega\right)=\mathcal{R}\left\{\mathrm{tr}\left(\mathbf{A}_{\mathbf{k},r}\mathbf{X}_{\mathbf{k}}\right)\right\} \tag{6.3}$$

where $r\in\{uu,vv,ww,uv\}$, $\mathbf{k}=[k_x,k_z,\omega]$, $\mathcal{R}(\cdot)$ indicates the real part of a complex number and $\mathrm{tr}(\cdot)$ denotes the matrix trace. The entries of the matrices $\mathbf{A}_{uu}$ are given by

$$\mathbf{A}_{\mathbf{k},uu,ij}=\sigma_{\mathbf{k},i}\sigma_{\mathbf{k},j}\left(\boldsymbol{\psi}_{\mathbf{k},i}\cdot\hat{\mathbf{e}}_x\right)\left(\boldsymbol{\psi}_{\mathbf{k},j}\cdot\hat{\mathbf{e}}_x\right)^* \tag{6.4}$$

with the other components defined similarly. These matrices are computed a priori from the SVD of the resolvent operator for a fixed set of k_x,k_z,ω. The matrix of unknown weights $\mathbf{X}_{\mathbf{k},ij}=\chi_{\mathbf{k},i}\chi^*_{\mathbf{k},j}$. The time averaged spectra are obtained over a discrete integral over a range of N_c wavespeeds $c=\omega/k_x\in[0,\overline{U}_0]$ where $\overline{U}_0$ is the mean velocity at the centerline of the channel.

$$\overline{E}_r(y;k_x,k_z)=\sum_{l=1}^{N_c}k_x\mathcal{R}\left\{\mathrm{tr}\left(\mathbf{A}_{\mathbf{k},r,l}\mathbf{X}_{\mathbf{k},l}\right)\right\}dc \tag{6.5}$$

The following optimization problem is formulated for fixed k_x, k_z.

$$\min_{\mathbf{X}_{l=1,2,\ldots N_c}}\|\overline{E}_r^{DNS}-\overline{E}_r(\mathbf{X})\| \tag{6.6}$$

$$\text{subject to} \tag{6.7}$$

$$\mathbf{X}_l\succ\mathbf{0},l=1,2,\ldots N_c. \tag{6.8}$$

The optimization is performed using the Matlab-based convex programming application CVX (Grant and Boyd, 2014). The finer details of the optimization are not the focus of this work and the interested reader is referred to McMullen et al. (2020) for more details. However, we highlight two crucial observations. First, since the variable in the optimization is $\mathbf{X}_{\mathbf{k},ij}=\chi_{\mathbf{k},i}\chi^*_{\mathbf{k},j}=|\chi_{\mathbf{k},i}||\chi_{\mathbf{k},j}|e^{i(a_{\mathbf{k},i}-a_{\mathbf{k},j})}$, we actually recover the relative phase shift between the resolvent modes at a given wavenumber. Second, we note that despite the fact that the optimization is performed on the time averaged spectra, the reconstruction of the temporal spectrum using Welch's method exhibits many of the features observed in observed in DNS, such as the localization about the critical layer (McMullen et al., 2020).

6.4 Energy Conserving Triads

Schmid and Henningson (2001) demonstrated that the nonlinearity of the NSE is energy conserving on a triad by triad basis. We have extended their analysis, which was formulated in the time domain, to the temporal frequency domain. Consider a set of triadically consistent Fourier modes, $\hat{\mathbf{u}}_\mathbf{a}$, $\hat{\mathbf{u}}_\mathbf{b}$, and $\hat{\mathbf{u}}_\mathbf{c}$, where $\mathbf{a} = \mathbf{b} + \mathbf{c}$. We define the *"intra-triad energy transfer"*

$$T_{\mathbf{a},\mathbf{b},\mathbf{c}} \equiv \mathcal{R}\{\langle \hat{\mathbf{u}}_\mathbf{a}, \hat{\mathbf{f}}_{\mathbf{b},\mathbf{c}} \rangle + \langle \hat{\mathbf{u}}_\mathbf{b}, \hat{\mathbf{f}}_{\mathbf{a},-\mathbf{c}} \rangle + \langle \hat{\mathbf{u}}_\mathbf{c}, \hat{\mathbf{f}}_{\mathbf{a},-\mathbf{b}} \rangle\}, \tag{6.9}$$

where

$$\hat{\mathbf{f}}_{\alpha,\beta} \equiv \hat{\mathbf{u}}_\alpha \cdot \nabla \hat{\mathbf{u}}_\beta + \hat{\mathbf{u}}_\beta \cdot \nabla \hat{\mathbf{u}}_\alpha \tag{6.10}$$

and

$$\langle \mathbf{q}_1, \mathbf{q}_2 \rangle \equiv \int_{-1}^{1} \mathbf{q}_1^* \mathbf{q}_2 dy. \tag{6.11}$$

It can then be show using integration by parts that

$$T_{\mathbf{a},\mathbf{b},\mathbf{c}} = 0 \ \ \forall \ \ \mathbf{a} = \mathbf{b} + \mathbf{c}. \tag{6.12}$$

A detailed derivation of (6.12) is presented in Appendix C.1. Throughout this chapter, we define the property (6.12) as *"intra-triad energy conservation"* and this general phenomenon as the concept of *"energy conserving triads*" (ECT).

6.5 Symmetries

The algorithm relies on the Fourier symmetries afforded by the statistically stationary homogeneous nature of the flow. Let $\hat{\mathbf{u}}_\mathbf{k} = [\hat{u}, \hat{v}, \hat{w}]$, $\mathbf{k} = [k_x, k_z, \omega]$, and $\tilde{\mathbf{k}} = [k_x, -k_z, \omega]$. Analysis of the resolvent formulation of the governing equations Fourier transformed in x, z, and t reveals that

$$\hat{\mathbf{u}}_{-\mathbf{k}} = [\hat{u}^*, \hat{v}^*, \hat{w}^*] \tag{6.13}$$

$$\hat{\mathbf{u}}_{\tilde{\mathbf{k}}} = [\hat{u}, \hat{v}, -\hat{w}] \tag{6.14}$$

$$\hat{\mathbf{u}}_{-\tilde{\mathbf{k}}} = [\hat{u}^*, \hat{v}^*, -\hat{w}^*]. \tag{6.15}$$

We note that the Fourier transform of the nonlinear term $\hat{\mathbf{f}}_\mathbf{k}$ obeys the same symmetries. See Appendix C.2 for the detailed derivation of these symmetries. Throughout this work, if $\mathbf{k} = [k_x, k_z]$, we use the notation $\tilde{\mathbf{k}}$ to refer to the transformation $k_z \rightarrow -k_z$, and thus $-\tilde{\mathbf{k}}$ refers to the transformation $k_x \rightarrow -k_x$.

Restrictions and Assumptions

As a starting point, we restrict ourselves to a single user specified wave speed $c = \omega/k_x$. This means that the temporal frequency ω is a function of k_x: $\omega(k_x) = ck_x$. This allows us to compress the 3D space time coordinates $[x, z, t]$ into the 2D coordinates

$$[\tilde{x}, z] = [x - ct, z]. \tag{6.16}$$

Thus going forward wave number vectors will be 2-dimensional: $\mathbf{k} = [k_x, k_z]$. The restriction to a single wave speed is approximately equivalent to the restriction to a fixed wall normal height since the Fourier modes of the solution generally have relatively localized support at their critical layer.

Further we assume that all Fourier modes of the solution are harmonics of the fundamentals, that is to say all wave numbers may be written in the form $\mathbf{k} = 2\pi[m/L_x, n/L_z]$ where $m, n \in \mathbb{Z}$. To avoid notational clutter, we rescale k_x and k_z by $L_x/2\pi$ and $L_z/2\pi$, respectively, such that the wave number $\mathbf{k} = 2\pi[m/L_x, n/L_z]$ is written as $\mathbf{k} = [m, n]$.

The proposed approach relies on a reference wave number whose phase is taken as an input to the algorithm. Therefore, our algorithm only predicts the phase information up to an unknown reference phase. We define the reference wave number $\mathbf{k}_0 = [1, 1]$ and its phase $a_{\mathbf{k}_0}$.

6.6 Algorithm

Using the magnitude of the resolvent weights $|\chi_{\mathbf{k},j}|$ obtained from the convex optimization, we may write each Fourier mode as an expansion in resolvent modes

$$\hat{\mathbf{u}}_{\mathbf{k}}(y) = e^{ia_{\mathbf{k},j}}|\chi_{\mathbf{k},j}|\sigma_{\mathbf{k},j}\boldsymbol{\psi}_{\mathbf{k},j}(y) \tag{6.17}$$

where summation over j is implied, and $\|\boldsymbol{\psi}_{\mathbf{k},j}\| = 1$. Recall that the relative phase shifts between the resolvent modes, $\Delta_{\mathbf{k},j} = a_{\mathbf{k},j} - a_{\mathbf{k},1}$, are known from the optimization described in §6.3. This allows us to write (6.17) as

$$\hat{\mathbf{u}}_{\mathbf{k}}(y) = e^{ia_{\mathbf{k},1}}\left(e^{i(a_{\mathbf{k},j}-a_{\mathbf{k},1})}|\chi_{\mathbf{k},j}|\sigma_{\mathbf{k},j}\boldsymbol{\psi}_{\mathbf{k},j}\right) = e^{ia_{\mathbf{k},1}}\left(e^{i\Delta_{\mathbf{k},j}}|\chi_{\mathbf{k},j}|\sigma_{\mathbf{k},j}\boldsymbol{\psi}_{\mathbf{k},j}\right) \tag{6.18}$$

where everything inside the parenthesis is known from the optimization. This implies that regardless of the number of resolvent modes retained in the optimization there is only a single unknown phase per wavenumber vector. For the sake of brevity and generality, we drop the subscript $_1$ and write $a_{\mathbf{k},1}$ as $a_{\mathbf{k}}$. This allows us to write (6.18) as

$$\hat{\mathbf{u}}_{\mathbf{k}}(y) = e^{ia_{\mathbf{k}}}\hat{\mathbf{q}}_{\mathbf{k}}(y) \tag{6.19}$$

where $\hat{\mathbf{q}}_{\mathbf{k}} \equiv e^{i\Delta_{\mathbf{k},j}}|\chi_{\mathbf{k},j}|\sigma_{\mathbf{k},j}\psi_{\mathbf{k},j}$ captures both the amplitude and wall normal shape of the Fourier mode. The combination of (6.19) and (6.9) leads to

$$T_{\mathbf{a},\mathbf{b},\mathbf{c}} = Q_{\mathbf{a},\mathbf{b},\mathbf{c}}e^{i\gamma} + Q^*_{\mathbf{a},\mathbf{b},\mathbf{c}}e^{-i\gamma}. \tag{6.20}$$

where $\gamma = -a_{\mathbf{a}} + a_{\mathbf{b}} + a_{\mathbf{c}}$. The complex constant $Q_{\mathbf{a},\mathbf{b},\mathbf{c}}$ is then defined as

$$Q_{\mathbf{a},\mathbf{b},\mathbf{c}} \equiv \langle \hat{\mathbf{q}}_{\mathbf{a}}, \hat{\mathbf{g}}_{\mathbf{b},\mathbf{c}} \rangle + \langle \hat{\mathbf{q}}_{\mathbf{b}}, \hat{\mathbf{g}}_{\mathbf{a},-\mathbf{c}} \rangle^* + \langle \hat{\mathbf{q}}_{\mathbf{c}}, \hat{\mathbf{g}}_{\mathbf{a},-\mathbf{b}} \rangle^* \tag{6.21}$$

where

$$\hat{\mathbf{g}}_{\alpha,\beta} \equiv \hat{\mathbf{q}}_{\alpha} \cdot \nabla \hat{\mathbf{q}}_{\beta} + \hat{\mathbf{q}}_{\beta} \cdot \nabla \hat{\mathbf{q}}_{\alpha}. \tag{6.22}$$

First we notice that the energy transfer $T_{\mathbf{a},\mathbf{b},\mathbf{c}}$ is not positive definite, and is in fact guaranteed to have exact zeros. Second, $T_{\mathbf{a},\mathbf{b},\mathbf{c}}$ does not depend independently on the individual phases $a_{\mathbf{a}}, a_{\mathbf{b}}, a_{\mathbf{c}}$ but is rather a function of the single variable $\gamma(a_{\mathbf{a}}, a_{\mathbf{b}}, a_{\mathbf{c}})$. Therefore the natural strategy of minimizing the residual of $|T_{\mathbf{a},\mathbf{b},\mathbf{c}}|$ is not viable because its three gradients are equal (up to a sign). Given these two observations, we thus look for exact zeroes of $T_{\mathbf{a},\mathbf{b},\mathbf{c}}$

$$T_{\mathbf{a},\mathbf{b},\mathbf{c}} = 0. \tag{6.23}$$

Consider the wave number triad $\mathbf{a} = \mathbf{b} + \mathbf{c}$. Solving (6.23) for the phases leads to

$$a_{\mathbf{a}} - a_{\mathbf{b}} - a_{\mathbf{c}} = \angle(Q_{\mathbf{a},\mathbf{b},\mathbf{c}}) - \pi/2 + r\pi \tag{6.24}$$

where $r \in \mathbb{Z}$ the term $+r\pi$ is due to the multiplicity of the complex logarithm and $Q_{\mathbf{a},\mathbf{b},\mathbf{c}}$ is a known function of the magnitudes of the resolvent weights and the resolvent modes. In practice the only relevant options are $r = 0, 1$ since we can restrict the phases such that $a_{\mathbf{k}} \in [-\pi, \pi]$. This means that (6.24) can equivalently be written as

$$a_{\mathbf{a}} - a_{\mathbf{b}} - a_{\mathbf{c}} = \angle(Q_{\mathbf{a},\mathbf{b},\mathbf{c}}) \pm \pi/2. \tag{6.25}$$

Note that the ambiguity $+r\pi$ in the phase is equivalent to an ambiguity in the sign of the Fourier mode. To avoid notational clutter, we drop the term $+r\pi$ going forward.

Outline

Using the Fourier symmetries (6.13)-(6.15), one can derive the phases, $a_{\mathbf{k}_x}$ and $a_{\mathbf{k}_z}$, of the 1D fundamental wave numbers $\mathbf{k}_x = [1, 0]$ and $\mathbf{k}_z = [0, 1]$ as a function of the reference phase $a_{\mathbf{k}_0}$ and the reference wave number $\mathbf{k}_0 = [1, 1]$. From there, it is possible to sequentially derive the phase, $a_{m\mathbf{k}_x}$ and $a_{n\mathbf{k}_z}$, of all harmonics of the 1D wave numbers $m\mathbf{k}_x = [m, 0]$ and $n\mathbf{k}_z = [0, n]$. This then allows us to recover

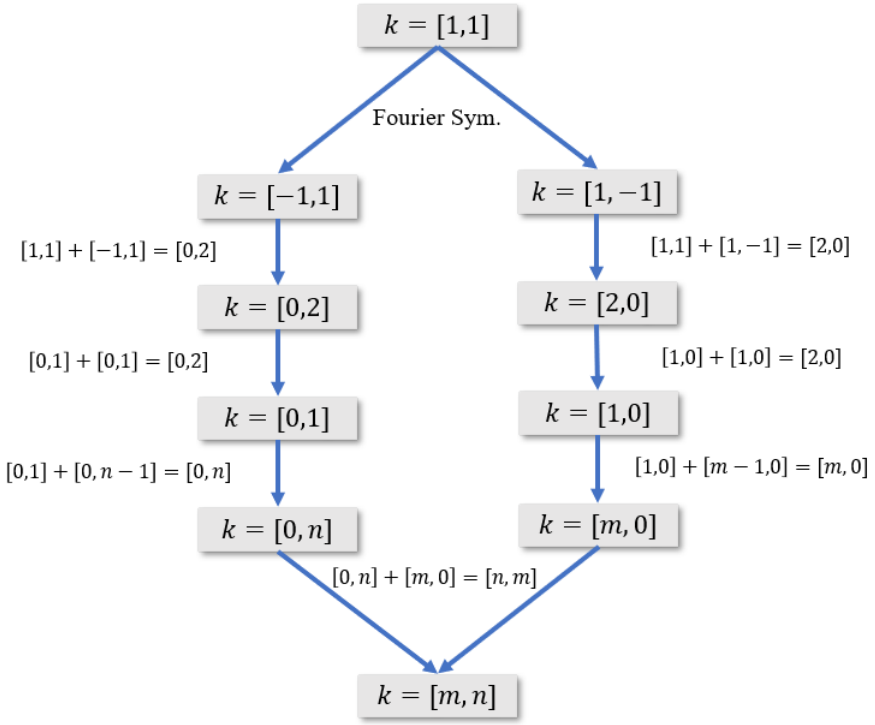

Figure 6.1: General outline of the phase reconstruction algorithm starting from the user defined reference phase for mode $\mathbf{k} = [1,1]$ to the phase of any arbitrary wavenumber $\mathbf{k} = [m,n]$. Note that at each step, there is only a single unknown phase.

the phase of any arbitrary wave number $\mathbf{k}_{m,n} = [m,n]$ using (6.24) through the triad $[m,n] = [m,0] + [0,n]$.[1] The outline of the general algorithm is summarized as a flow chart in Figure 6.1 and illustrated graphically in Figure 6.2.

Step 1: Streamwise Constant Wavenumbers

We first consider the triad: $\mathbf{a} = \mathbf{b} + \mathbf{c}$ where $\mathbf{a} = 2\mathbf{k}_z = [0,2]$, $\mathbf{b} = \mathbf{k}_0 = [1,1]$, and $\mathbf{c} = -\tilde{\mathbf{k}}_0 = [-1,1]$. The symmetry (6.13) reveals that the transformation $k_x \longrightarrow -k_x$ conjugates the resolvent weights which in this case implies that: $a_{\mathbf{c}} = -a_{\mathbf{b}} = -a_{\mathbf{k}_0} = 0$. We can then compute the phase of $\mathbf{a} = 2\mathbf{k}_z$ using (6.24)

$$a_{2\mathbf{k}_z} - \left(a_{\mathbf{k}_0} - a_{\mathbf{k}_0}\right) = \angle(Q_{2\mathbf{k}_z,\mathbf{k}_0,-\tilde{\mathbf{k}}_0}) - \pi/2 \tag{6.26}$$

$$a_{2\mathbf{k}_z} = \angle(Q_{2\mathbf{k}_z,\mathbf{k}_0,-\tilde{\mathbf{k}}_0}) - \pi/2. \tag{6.27}$$

[1] Note that to reconstruct all phase information, it is not necessary to consider every possible triadic interaction. One need only analyze enough triads such that each Fourier mode is included at least once.

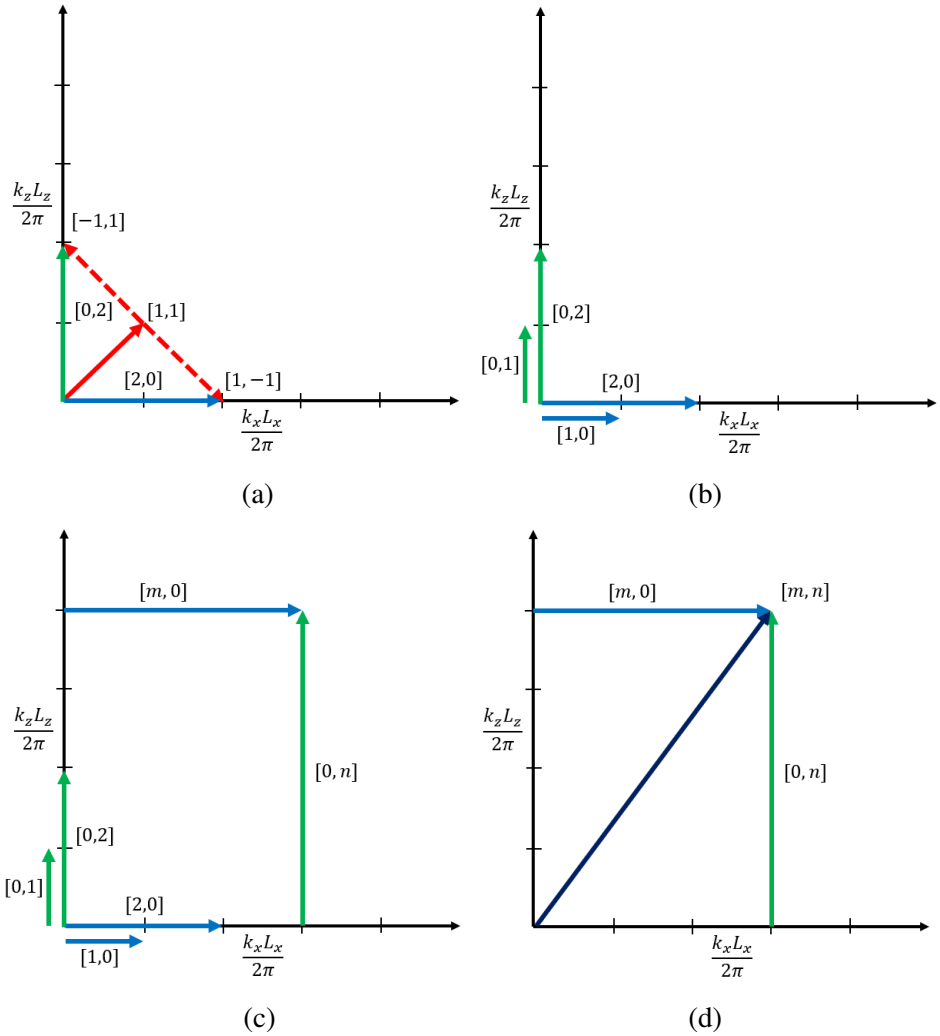

Figure 6.2: The four general steps in the proposed algorithm. a) From the reference mode $[1, 1]$ (solid red) Fourier symmetries give $\pm[1, -1]$ (dashed red) and their interaction gives $[2, 0]$ (green) and $[0, 2]$ (blue). b) The modes $[2, 0]$ and $[0, 2]$ are used to compute $[1, 0]$ and $[0, 1]$. c) From $[1, 0]$ and $[0, 1]$ one may calculate all $[m, 0]$ and $[0, n]$. d) Any arbitrary $[m, n]$ may be computed from the triad $[m, 0]$ and $[0, n]$.

Next we consider the triad: $\mathbf{a} = \mathbf{b} + \mathbf{c}$ where $\mathbf{a} = 2\mathbf{k}_z = [0, 2]$, $\mathbf{b} = \mathbf{k}_z = [0, 1]$, and $\mathbf{c} = \mathbf{k}_z = [0, 1]$. We can again use (6.24) to compute the phase $a_{\mathbf{k}_z}$.

$$a_{\mathbf{2k_z}} - \left(a_{\mathbf{k_z}} + a_{\mathbf{k_z}}\right) = \angle(Q_{2\mathbf{k}_z,\mathbf{k}_z,\mathbf{k}_z}) - \pi/2 \tag{6.28}$$

$$a_{\mathbf{k_z}} = \frac{1}{2}\left(a_{\mathbf{2k_z}} - \angle(Q_{2\mathbf{k}_z,\mathbf{k}_z,\mathbf{k}_z}) + \pi/2\right). \tag{6.29}$$

We can then use (6.27) to write

$$a_{\mathbf{k_z}} = \frac{1}{2}\left(\angle(Q_{2\mathbf{k}_z,\mathbf{k}_0,-\tilde{\mathbf{k}_0}}) - \angle(Q_{2\mathbf{k}_z,\mathbf{k}_z,\mathbf{k}_z})\right). \tag{6.30}$$

This now allows us to sequentially compute the phase of all harmonics of $\mathbf{k}_z$.

$$a_{n\mathbf{k}_z} = \left(a_{(n-1)\mathbf{k}_z} + a_{\mathbf{k}_z}\right) + \angle(Q_{n\mathbf{k}_z,(n-1)\mathbf{k}_z,\mathbf{k}_z}) - \pi/2 \tag{6.31}$$

$$a_{n\mathbf{k}_z} = a_{(n-1)\mathbf{k}_z} + \frac{1}{2}\left(\angle(Q_{2\mathbf{k}_z,\mathbf{k}_0,-\tilde{\mathbf{k}_0}}) - \angle(Q_{2\mathbf{k}_z,\mathbf{k}_z,\mathbf{k}_z})\right) + \angle(Q_{n\mathbf{k}_z,(n-1)\mathbf{k}_z,\mathbf{k}_z}) - \pi/2 \tag{6.32}$$

Note that the phases of these streamwise constant modes are independent of the reference phase $a_{\mathbf{k}_0}$. This implies that the phase information of the streamwise constant component of the flow does not depend on the streamwise varying component. This independence is due to the symmetry (6.15) which is valid in the frequency domain, but is generally not observed in DNS, which is formulated in the time domain. Therefore, when applied to temporal data, this one-way coupling is not expected to be exactly accurate.

Step 2: Spanwise Constant Wavenumbers

Next we perform the same analysis for the spanwise constant modes and consider the triad: $\mathbf{a} = \mathbf{b} + \mathbf{c}$ where $\mathbf{a} = 2\mathbf{k}_x = [2, 0]$, $\mathbf{b} = \mathbf{k}_0 = [1, 1]$, and $\mathbf{c} = \tilde{\mathbf{k}}_0 = [1, -1]$. The symmetry (6.14) reveals that the resolvent weights are invariant to the transformation $k_z \to -k_z$ which in this case implies that they have the same phase: $a_{\mathbf{c}} = a_{\mathbf{b}} = a_{\mathbf{k}_0} = 0$. We can then compute the phase of $\mathbf{a} = 2\mathbf{k}_x$ using (6.24)

$$a_{\mathbf{2k_x}} - \left(a_{\mathbf{k}_0} + a_{\mathbf{k}_0}\right) = \angle(Q_{2\mathbf{k}_x,\mathbf{k}_0,\tilde{\mathbf{k}_0}}) - \pi/2 \tag{6.33}$$

$$a_{\mathbf{2k_z}} = 2a_{\mathbf{k}_0} + \angle(Q_{2\mathbf{k}_z,\mathbf{k}_0,\tilde{\mathbf{k}_0}}) - \pi/2. \tag{6.34}$$

Next we consider the triad: $\mathbf{a} = \mathbf{b} + \mathbf{c}$ where $\mathbf{a} = 2\mathbf{k}_x = [2, 0]$, $\mathbf{b} = \mathbf{k}_x = [1,]$, and $\mathbf{c} = \mathbf{k}_x = [1, 0]$. We can again use (6.24) to compute the phase $a_{\mathbf{k}_x}$.

$$a_{\mathbf{2k_x}} - \left(a_{\mathbf{k_x}} + a_{\mathbf{k_x}}\right) = \angle(Q_{2\mathbf{k}_x,\mathbf{k}_x,\mathbf{k}_x}) - \pi/2 \tag{6.35}$$

$$a_{\mathbf{k_x}} = \frac{1}{2}\left(a_{\mathbf{2k_x}} - \angle(Q_{2\mathbf{k}_x,\mathbf{k}_x,\mathbf{k}_x}) + \pi/2\right) \tag{6.36}$$

We can then use (6.34) to write

$$a_{\mathbf{k_x}} = \frac{1}{2}\left(2a_{\mathbf{k}_0} + \angle(Q_{2\mathbf{k}_x,\mathbf{k}_0,\tilde{\mathbf{k}_0}}) - \angle(Q_{2\mathbf{k}_x,\mathbf{k}_x,\mathbf{k}_x})\right). \tag{6.37}$$

This now allows us to sequentially compute the phase of all harmonics of $\mathbf{k}_x$.

$$a_{n\mathbf{k}_x} = \left(a_{(n-1)\mathbf{k}_x} + a_{\mathbf{k}_x}\right) + \angle(Q_{n\mathbf{k}_x,(n-1)\mathbf{k}_x,\mathbf{k}_x}) - \pi/2 \tag{6.38}$$

$$a_{n\mathbf{k}_x} = a_{(n-1)\mathbf{k}_x} + a_{\mathbf{k}_0} + \frac{1}{2}\left(\angle(Q_{2\mathbf{k}_x,\mathbf{k}_0,\tilde{\mathbf{k}_0}}) - \angle(Q_{2\mathbf{k}_x,\mathbf{k}_x,\mathbf{k}_x})\right) + \angle(Q_{n\mathbf{k}_x,(n-1)\mathbf{k}_x,\mathbf{k}_x}) - \pi/2 \tag{6.39}$$

Note that unlike the streamwise constant modes, the phase of the spanwise constant modes does depend on the phase of the reference mode $\mathbf{k}_0$.

Step 3: Arbitrary 2D Wavenumbers

We now have phase information for all Fourier modes which are either spanwise or streamwise constant. This now allows us to reconstruct the phase information of any arbitrary Fourier mode with wave number $\mathbf{k}_{m,n} = [m, n]$ using (6.24).

$$a_{\mathbf{k}_{m,n}} = \left(a_{m\mathbf{k}_x} + a_{n\mathbf{k}_z}\right) + \angle(Q_{\mathbf{k}_{m,n},m\mathbf{k}_x,n\mathbf{k}_z}) - \pi/2 + r\pi \tag{6.40}$$

The phases $a_{n\mathbf{k}_z}$ and $a_{m\mathbf{k}_x}$ are given by (6.32) and (6.39), respectively. We have thus reconstructed the phase information of the rank 1 approximation of all Fourier modes with fixed wave speed c up to the as yet unspecified reference phase.

We would like to highlight a subtlety in (6.40). The first term on the right hand side (6.39) depends on the reference phase while the second term, (6.32), does not. There is a one-way coupling between the phases of the streamwise constant and streamwise varying modes. The $k_x = 0$ affect the evolution of the $k_x > 0$ phases, while these 3D modes do not feed back onto the streamwise constant component.

6.7 Example

Here we present several examples of how the proposed algorithm works in practice. The effectiveness of the resolvent spectrum optimization outlined in §6.3 is well described in McMullen et al. (2020), and we do not address it here. We focus on the novel contributions of this thesis: the phase reconstruction based on the energy

conserving triads described in §6.6. In order to illustrate our proposed algorithm, we apply it to a series of exact solutions to the NSE. In this case, we have exact knowledge of the Fourier modes and their relative phase shifts, which allows us to test the ability of our algorithm to reconstruct the relative phase shifts with knowledge of the exact mode shapes and amplitudes.

Such phase shifts are only defined relative to some fixed anchor point in space. If we define the anchor point, y_0, then the data may be written in the form (6.19) as follows

$$\hat{\mathbf{u}}_{\mathbf{k}}(y) = e^{i(\angle \hat{\mathbf{u}}_{\mathbf{k}}(y))} |\hat{\mathbf{u}}_{\mathbf{k}}(y)| \tag{6.41}$$

$$\hat{\mathbf{u}}_{\mathbf{k}}(y) = e^{ia_{\mathbf{k}}} \left(e^{i(\angle \hat{\mathbf{u}}_{\mathbf{k}}(y) - a_{\mathbf{k}})} |\hat{\mathbf{u}}_{\mathbf{k}}(y)| \right) \tag{6.42}$$

where $a_{\mathbf{k}}$ is the phase at the anchor point. The Fourier mode can then be written in the form

$$\hat{\mathbf{u}}_{\mathbf{k}} = e^{ia_{\mathbf{k}},} \hat{\mathbf{q}}_{\mathbf{k}} \tag{6.43}$$

such that (6.43) is equivalent to the form (6.19). We then use the "unshifted" modes $\hat{\mathbf{q}}_{\mathbf{k}}(y)$ as the input to our algorithm and compare the phase shifts predicted by our algorithm to the exact phases computed from the data using (6.43). Since our algorithm is only defined up to a reference phase, we compare the phase shift from that reference wave number, $\mathbf{k}_0 = [1, 1]$,

$$\Delta a_{\mathbf{k}} = \frac{a_{\mathbf{k}} - a_{\mathbf{k}_0}}{\pi}. \tag{6.44}$$

Exact Coherent States

First we analyze four time invariant equilibrium solutions: EQ3, EQ4, EQ5, and EQ6. The solutions were taken from the open source database available at *channelflow.org* (Gibson, 2014). A Fourier decomposition in x and z was performed on the data to obtain a spectral representation of the form (6.43). In this case, we define the anchor point as the center line, and define the phase of each Fourier mode as phase of the streamwise velocity component at the center line.

The results are plotted in Figure 6.3. The phase shifts predicted by our algorithm are shown in circles and the reference phase shifts computed directly from data are plotted as triangles. For the solutions considered here, the modes with $k_x < 3$ contain more than 99.9% of the kinetic energy. Therefore we plot only the phase shifts for $k_x = 0, 1, 2$, which the algorithm is able to accurately reconstruct. Furthermore, we exactly capture the phases of the streamwise constant modes as these do not rely on the reference phase.

Turbulent Channel Flow

Second, we analyze the DNS of a turbulent channel flow at $Re_\tau = 550$ with channel half height h and centerline velocity $\overline{U}_0$. The DNS was computed using the spectral code described in Flores and Jiménez (2006)[2]. We first interpolate the data onto a uniform time grid and then perform a temporal Fourier transform over a time horizon of $125h/\overline{U}_0$ to again obtain a spectral representation of the form (6.43). We consider two fixed values of the wave speed, $c/\overline{U}_0 = 0.1$ and 0.5. This means that for each k_x we only retain the temporal frequency $\omega = ck_x$. This then implies that the data is parameterized by a 2D wave number as outlined in §6.5. In this case we define the anchor point as the critical layer, the point where $\overline{U}(y) = c$, and define the phase of each Fourier mode as phase of the streamwise velocity component at that critical layer.

The results for turbulent channel flow for $c/\overline{U}_0 = 0.1$ and 0.5 are shown in Figures 6.4 and 6.5, respectively. In this case, we plot the phase shifts for $k_x = 0, 1, 2, 3$. The algorithmic prediction is not exact as in the ECS example, but is reasonably accurate, and captures the qualitative trend of the phase shifts as a function of k_z. The error in this example is in part due to the fact that the DNS solution does not generally obey the frequency domain symmetries (6.13) - (6.15) which are central to the algorithm. This is likely due to the fact that we have computed the frequency content through a simple FFT of a single time signal of data, and the time interval we considered was likely not long enough for the phases to be fully converged. These convergence issues could potentially be addressed using a windowing method, however such an analysis was not pursued here. It is interesting to observe that these trends exhibit some similarities across wave speeds. This indicates that it may be possible to derive simple rules governing inter-wavespeed phase shifts. However, such an analysis is beyond the scope of this work.

Outlook

These results are intended as a proof of concept to illustrate the efficacy of the proposed algorithm, and as such we would like to highlight some of the assumptions made in this analysis. First, we reiterate that we have used the exact Fourier mode shapes as an input, and thus the excellent prediction is expected. Applying this algorithm to the resolvent model output from the optimization described in §6.3 is the topic of ongoing research. Second, at each step in the algorithm the prediction of the phase is only defined up to $r\pi$ with $r = 0, 1$. To illustrate the potential of our

[2]The DNS data was computed and generously provided by Yuting Huang.

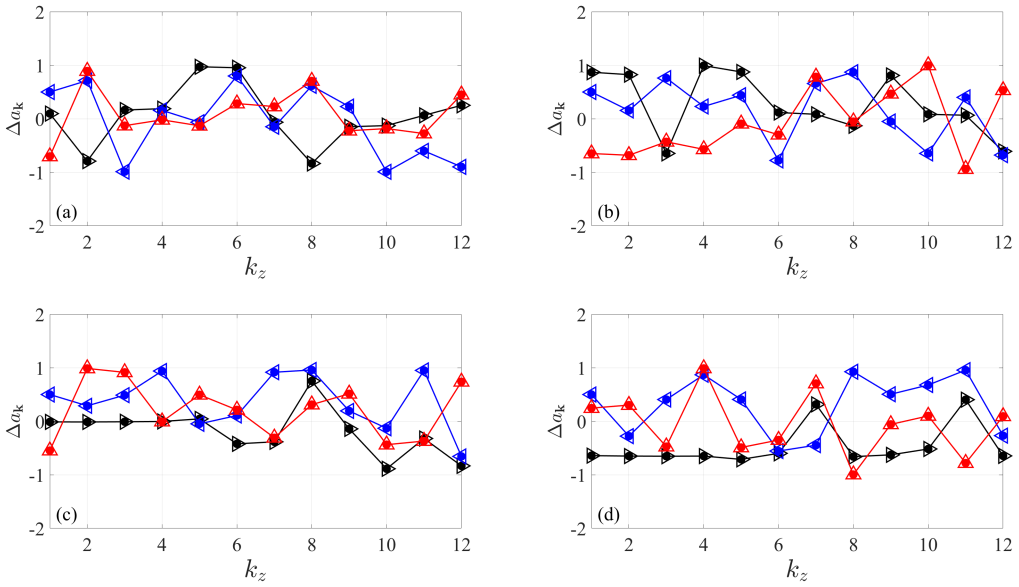

Figure 6.3: Phase shifts from reference mode for $k_x = 0$ (black), $k_x = 1$ (blue), and $k_x = 2$ (red). Algorithmic prediction (circles) and reference phase shifts computed from data (triangles). Solutions EQ3 - EQ6 (a) - (d).

algorithm, at each step we choose the value of r that leads to the best approximation of the reference phase shifts. A first principles-based prediction of the optimal value of r is a topic of ongoing research. Finally, we note that these results does not imply the full recovery of the phase information of the solution since the reference phase $a_{\mathbf{k}_0}$ is still unknown. Nevertheless, we believe these results show the potential of the ECT framework to open new avenues of nonlinear physics-based models.

6.8 Discussion and Possible Extensions

Here we summarize the challenges of the proposed framework as well as potential avenues for future research.

Limitations and Potential Problems

As illustrated by the example described in §6.7, our algorithm is capable of exploiting the principle of intra-triad energy conservation to predict phase information given knowledge of the mode shapes. However, this approach is not without limitations and challenges. The primary difficulty in successfully applying our method in practice is the sensitivity of the predicted phase to errors in the quantity $Q_{\mathbf{a},\mathbf{b},\mathbf{c}}$. Such errors are possible even with supposedly "exact" knowledge of the mode shapes. First of all, note that roughly speaking $Q_{\mathbf{a},\mathbf{b},\mathbf{c}}$ scales with the cube of the

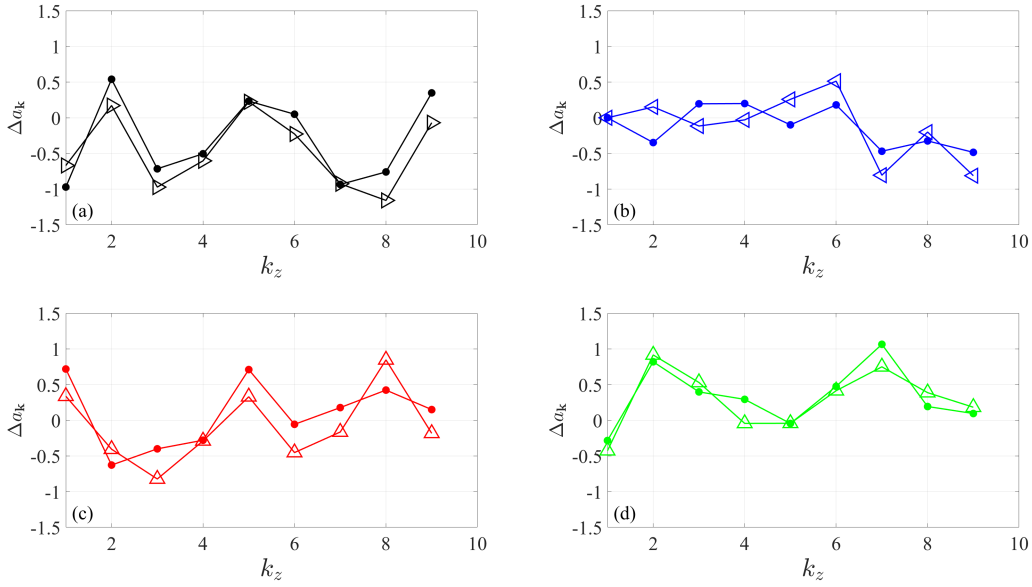

Figure 6.4: Phase shifts from reference mode for turbulent channel flow at $Re_\tau = 550$ for $c/\overline{U}_0 = 0.1$. Algorithmic prediction (circles) and reference phase shifts computed from data (triangles). $k_x = 0, 1, 2, 3$ (a) - (d).

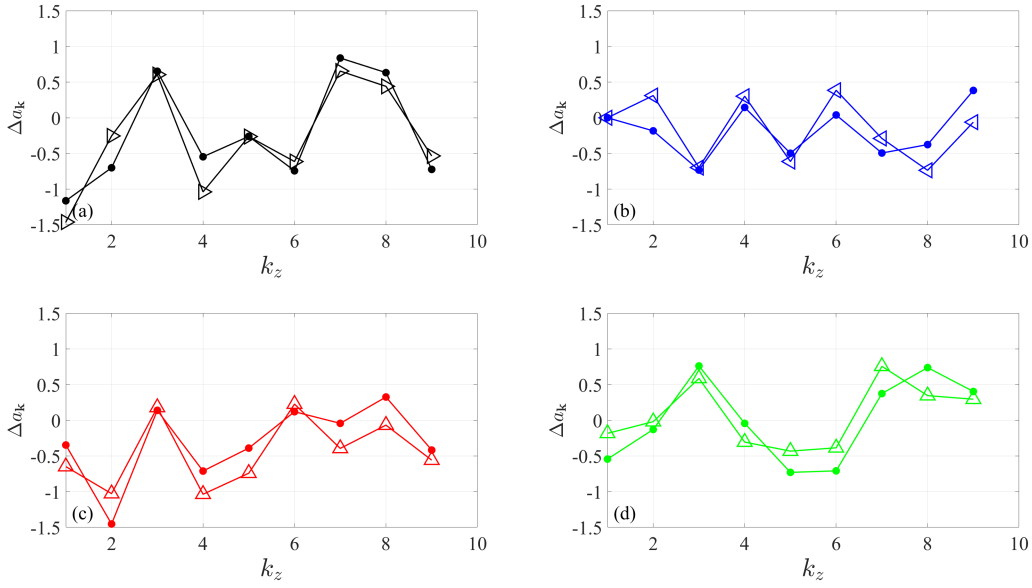

Figure 6.5: Phase shifts from reference mode for turbulent channel flow at $Re_\tau = 550$ for $c/\overline{U}_0 = 0.5$. Algorithmic prediction (circles) and reference phase shifts computed from data (triangles). $k_x = 0, 1, 2, 3$ (a) - (d).

velocity, i.e. $Q_{\mathbf{a},\mathbf{b},\mathbf{c}} \sim O(\hat{\mathbf{u}}^3)$. If we assume the mean velocity is of order one, then for some general triad with $\mathbf{a}, \mathbf{b}, \mathbf{c} \neq 0$ inspection of the data reveals that each Fourier mode is generally $O(10^{-3})$ or $O(10^{-4})$ meaning that we may have $Q_{\mathbf{a},\mathbf{b},\mathbf{c}} \sim O(10^{-12})$ regardless of the phase of the Fourier modes. In fact, evaluating the intra-triad energy transfer (6.9) for the full DNS solution, which mathematically should be exactly zero, gives values which are also $\sim O(10^{-12})$. This implies that our algorithm is searching for zeros of a quantity, which from a numerical point of view, is vanishingly small regardless of its argument.

Furthermore, in order to compute this quantity, we perform a numerical Fourier transform of the velocity field to obtain the Fourier modes, then numerically differentiate these modes to obtain the gradient in the nonlinear term, and then finally perform a numerical integration to arrive at the scalar $Q_{\mathbf{a},\mathbf{b},\mathbf{c}}$. Each of these operations, particularly the numerical differentiation is susceptible to small but potentially impactful numerical errors. In cases where the exact mode shape is not known, the error in the mode shape would of course exacerbate these problems.

On a more fundamental level, the inherent limitation of our algorithm is the indeterminacy of the reference phase. While even moments are invariant with respect to this reference phase, odd moments such as the skewness are not. Therefore, the derivation of this phase from first principles remains a topic of ongoing research. Naively one might assume that this phase could be computed through iteratively analyzing the triad $[1, 0] + [0, 1] = [1, 1]$, however, when evaluated for this triad, the reference phase drops out of the expression (6.24). Additionally, the multi-valued nature of the complex logarithm leads to the arbitrary $r\pi$ shift in (6.24). Since in §6.7, we had the luxury of knowing the DNS phases we were able to choose the correct value for r, however in a practical application it is not clear how this value would be optimally chosen.

Application to Quasilinear Theory

Quasilinear (QL) and generalized quasilinear (GQL) theory are simplified models of the Navier-Stokes equations which neglect the direct affect of the nonlinear interaction between small scales on the evolution of those small scales. While QL theory has had success in the prediction of several features of turbulent flows, there are still discrepancies between the flow predicted by QL simulations and DNS (Marston et al., 2016; Hwang and Eckhardt, 2020; Skouloudis and Hwang, 2021). This motivates the desire to either a) augment the QL simulation by introducing a forcing

model to replace the neglected nonlinear interactions or b) derive a transformation on the QL solution to better approximate the DNS solution. In regards to the former, our algorithm could augment stochastic forcing models such as those used by Hwang and Eckhardt (2020) to better approximate the true nonlinearity.

However, we are most optimistic about the potential of our framework to lead to a post-hoc transformation of QL solution to something which more accurately resembles the true DNS solution. Since the QL simulation neglects the nonlinear interaction of small scales in the forcing of those same small scales, triads involving only small scales do not obey the energy conservation principle discussed in §6.4. Given the Fourier modes of the QL solution written in the form (6.19), one could discard the phases of these Fourier modes and reconstruct them using an algorithm similar to that described here ensuring that the small scale velocity obeys the energy conserving properties required by the full NSE. This could be done online, at each time step, or a posteriori.

6.9 Summary

In this chapter, we have suggested an algorithm for the reconstruction of the phase information lost in the compression of the full velocity field to the kinetic energy spectrum. The wall normal phase variation of the flow is recovered through the convex optimization approach introduced by Moarref et al. (2014a) and McMullen et al. (2020). The novel contribution of this thesis is the reconstruction of the relative phase shifts between Fourier modes based on the intra-triad conservation of kinetic energy. Given the magnitude and wall normal variation of the mode shapes, the relative phase shifts are computed by setting the net intra-triad energy transfer to zero. These triads are analyzed sequentially, such that in each step of the algorithm there is only one unknown phase. We illustrated the phase reconstruction capabilities of the algorithm by applying it to a series of exact solutions to the NSE, and demonstrated that given exact knowledge of the mode shapes the algorithm is able to accurately predict their relative phase shifts. We concluded with a discussion of the possible application of these concepts to QL simulations through online or a posteriori enforcement of the intra-triad energy conservation of the small scales.

Chapter 7

CONCLUSIONS AND FUTURE WORK

This thesis has contributed to both the linear and nonlinear aspects of resolvent analysis and general equations driven modeling of wall-bounded flows. This chapter summarizes the key contributions of this thesis and suggests avenues for future research.

The first contribution was the alternative theoretical framework for resolvent analysis described in Chapter 2. This alternative framework, coined VRA, is based on the calculus of variations and avoids the reliance on the inversion of the linear operator. Instead of defining the resolvent modes as the singular value decomposition of the resolvent operator, this framework extends the concept of the "optimal" forcing and response to defining the entire resolvent basis as stationary points of the operator norm of the linearized dynamics. Inverse free methods have been used by other researchers as numerical strategies, however the rigorous variational foundation introduced here is a novel contribution of this thesis. Furthermore, we proposed a method based on the variational formulation which allows for the approximation of computationally intensive 2D/3C resolvent response modes as an expansion in cheap 1D modes. We illustrated the proposed method through a series of examples including both streamwise periodic and streamwise developing base flows. In the former case, the VRA prediction of the response modes displayed excellent quantitative agreement with the SVD-based reference. In the latter case, the VRA prediction of the response modes became progressively less accurate with increased streamwise development of the base flow. This deterioration was found to be due to the boundary condition mismatch between the streamwise periodic input modes and the non-periodic nature of the base flow. Due to the directional amplification of the resolvent operator, the VRA prediction of the 2D/3C forcing modes was considerably less accurate. The improvement of the prediction of the forcing modes as well as the exploration of other modeling types of basis are fruitful avenues of future research. Finally, unlike the SVD-based formulation, the variational definition allows for systematic and rigorous way to define the resolvent with respect to any arbitrary type of norm. In this thesis, we consider only quadratic norms, however in theory the variational formulation allows for other types of norms such as 1-norms which could be used to promote sparsity in the resolvent basis.

The second contribution was the nonlinear resolvent model of Taylor vortex flow discussed in Chapter 4. Even though resolvent analysis formally retains the nonlinear coupling between the forcing and response, the explicit nonlinearity is neglected in most RA-based studies, some of the notable exceptions being Rosenberg (2018) who computed nonlinear models of ECS and Nogueira et al. (2020) who analyzed the statistics of the nonlinear forcing. We illustrate that the resolvent form of the nonlinear fluctuation equation (2.17) can be solved effectively, thereby demonstrating an explicit closure of the resolvent loop illustrated in Figure 1.1. In Chapter 5 we augment these results by computing the mean velocity profile from the laminar base flow alleviating the reliance of the resolvent model on an input mean velocity profile. We expand on the results of Rosenberg (2018) and demonstrated that the flow transitions from a regime where the forcing cascade is purely downscale to a regime where an equal and opposite upscale forcing cascade emerges. This analysis illustrates the explicit physical phenomenon which causes the breakdown of weakly nonlinear analysis. We showed analytically that this transition is a direct consequence of the functional form of the nonlinearity of the NSE and the decay rate of the energy spectrum. A decay faster than k^{-2} is indicative of a weakly nonlinear regime, while a slower decay indicates a fully nonlinear flow. The immediate next steps of this branch of inquiry is the extension of the optimization-based technique described here to higher Reynolds numbers and more complex flows. The primary challenge in this regard is the dense 6^{th} order tensor in (4.29) which becomes prohibitively large with increasing degrees of freedom. Therefore, the application of this method to higher dimensional flows must be accompanied by the development of more efficient sets of basis functions. This could potentially be addressed through an intelligent choice of norm permitted by the VRA framework. In the Taylor Couette context, this could for example be used to enforce the approximate wall normal symmetry observed in the solution but not the resolvent basis. Another potential strategy would be to apply the ECT framework discussed in Chapter 6 to sequentially compute the solution one triad at a time. This would limit the degrees of freedom required in each optimization, and could lead to a straightforward approach to continue solutions to higher Reynolds numbers through the sequential inclusion of additional triads.

The third contribution is that we have proposed an algorithm to reconstruct phase information from the energy spectrum. The algorithm is based on the concept of energy conserving triads introduced by Schmid and Henningson (2001), a framework that is largely unexplored in the literature. We apply our algorithm to a series of

exact solutions to the NSE for which we are able to accurately predict the phase shifts between Fourier modes. The prediction of the phase information would allow for a transformation from first order statistics to higher order moments derived directly from the NSE. Our results have merely illustrated the potential of the ECT framework in the development of highly truncated equations-based models. Of particular relevance is the ability to introduce the nonlinear dynamics in a sequential manner since each triad can be analyzed in turn, such that at each step there is only a single unknown variable. For example our algorithm could be used to augment QL simulations to enforce energy conservation among the small scales whose nonlinear interaction is neglected in the QL equations, a topic of ongoing research.

Overall, we hope this thesis has highlighted the potential avenues for extending resolvent analysis and equations driven modeling in general. Our variational formulation opens up the concept of resolvent analysis to a wider range of applications enabled by its cost saving potential as well as its theoretical framing in terms of arbitrary norms. Additionally we have highlighted the potential for reduced order models to accurately model nonlinear dynamics if the nonlinear interactions are incorporated in a systematic and sequential manner.

Appendix A

CHAPTER III

A.1 Variation Over Complex Fields

The following derivation is an extension of the theory derived in Wirtinger (1927) and Brandwood (1983). Let $J = \langle F(q, q^*, \nabla q, \nabla q^*)\rangle \in \mathbb{R}$ where $q = a + ib \in \mathbb{C}^\infty$, with $a, b \in \mathbb{R}^\infty$. The functional J can equivalently be written as $J = \langle F(a, b, \nabla a, \nabla b)\rangle$. The Euler-Lagrange equations defining stationary points of J with respect to a and b are given by:

$$\frac{\delta F}{\delta a} \equiv \frac{\partial F}{\partial a} - \nabla \frac{\partial F}{\partial \nabla a} = 0 \tag{A.1}$$

$$\frac{\delta F}{\delta b} \equiv \frac{\partial F}{\partial b} - \nabla \frac{\partial F}{\partial \nabla b} = 0. \tag{A.2}$$

Since $F \in \mathbb{R}$, a simple change of variables to q and q^* leads to

$$\frac{\delta F}{\delta q} = \frac{1}{2}\left(\frac{\delta F}{\delta a} - i\frac{\delta F}{\delta b}\right) \tag{A.3}$$

$$\frac{\delta F}{\delta q^*} = \frac{1}{2}\left(\frac{\delta F}{\delta a} + i\frac{\delta F}{\delta b}\right) \tag{A.4}$$

which implies that

$$\frac{\delta F}{\delta a} = \frac{\delta F}{\delta b} = 0 \Rightarrow \frac{\delta F}{\delta q} = \frac{\delta F}{\delta q^*} = 0. \tag{A.5}$$

Furthermore, since F, a, and b are real functions, it follows that

$$\frac{\delta F}{\delta q} = 0 \Rightarrow \frac{\delta F}{\delta a} = \frac{\delta F}{\delta b} = 0 \tag{A.6}$$

$$\frac{\delta F}{\delta q^*} = 0 \Rightarrow \frac{\delta F}{\delta a} = \frac{\delta F}{\delta b} = 0 \tag{A.7}$$

and therefore either of the above conditions is necessary and sufficient for stationarity.

A.2 Orr-Sommerfeld Eigenfunctions

The Orr-Sommerfeld eigenvalue problem for $k_x = 0$ on the domain $y \in [-1, +1]$ is given by

$$-i\omega\nabla^2 v_j - \frac{1}{R}\nabla^4 v_j = \lambda_j^{OS}\nabla^2 v_j \tag{A.8}$$

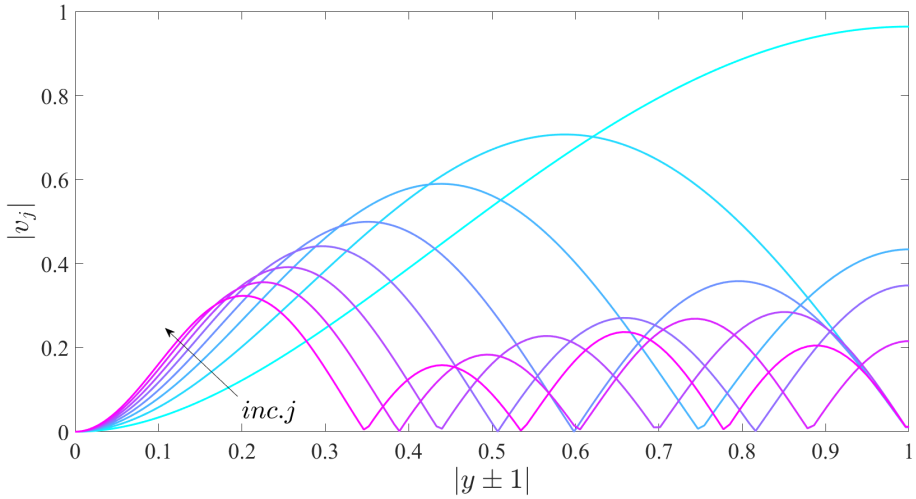

Figure A.1: Absolute value of the Orr-Sommerfeld eigenfunctions v_j ($j = 1...8$) for $k_x = 0$, $k_z = 6$, and $\omega = 0.1$.

subject to the boundary condition $v(\pm 1) = v_y(\pm 1) = 0$. This problem has been analyzed by several authors including Dolph and Lewis (1958); Jovanović and Bamieh (2005), and the solutions are found to be:

$$\begin{aligned} v_j(y; k_z) = A_j \left(\cos(\gamma_j(y+1)) - \cosh(k_z(y+1))\right) + \\ B_j \left(\sin(\gamma_j(y+1)) - \gamma_j k_z^{-1} \sinh(k_z(y+1))\right) \end{aligned} \tag{A.9}$$

$$\lambda_j^{OS} = \frac{1}{R}\left(\gamma_j^2 + k_z^2\right) - i\omega \tag{A.10}$$

where the γ_j are defined as the roots of the following equation:

$$\cos(2\gamma)\cosh(2k_z) - \left(\frac{k_z^2 - \gamma^2}{2k_z\gamma}\right)\sin(2\gamma)\sinh(2k_z) - 1 = 0. \tag{A.11}$$

The relative amplitudes A_j and B_j are defined for each γ_j as the solutions of the following system:

$$\begin{bmatrix} \cos(2\gamma_j) - \cosh(2k_z) & \sin(2\gamma_j) - \left(\gamma_j k_z^{-}1\right)\sinh(2k_z) \\ -\gamma_j \sin(2\gamma_j) - k_z \sinh(2k_z & \gamma_j\left(\cos(2\gamma_n) - \cosh(2k_z)\right) \end{bmatrix} \begin{bmatrix} A_j \\ B_j \end{bmatrix} = \begin{bmatrix} 0 \\ 0 \end{bmatrix}. \tag{A.12}$$

In Figure A.1, we plot the eigenfunctions v_j for the same parameters plotted in §3.2: $k_x = 0$, $k_z = 6$, and $\omega = 0.1$.

A.3 Singular Value Scaling

The resolvent operator we consider in §3.2 is defined as

$$\mathbf{H} = \begin{bmatrix} L_{OS} & 0 \\ \bar{U}_y & L_{SQ} \end{bmatrix}^{-1} = \begin{bmatrix} L_{OS}^{-1} & 0 \\ -L_{SQ}^{-1}\bar{U}_y L_{OS}^{-1} & L_{SQ}^{-1} \end{bmatrix}. \tag{A.13}$$

Noting the definitions (3.22) and (3.21), if $\omega = 0$, $\mathbf{H}$ may be written in the form

$$\mathbf{H} = \begin{bmatrix} RH_{vv} & 0 \\ R^2 H_{uv} & RH_{uu} \end{bmatrix}, \tag{A.14}$$

where $H_{vv}, H_{uv}, H_{uu} \neq f(R)$. This reveals that as $R \to \infty$, $\|H\| = \sigma_1 \to R^2\|H_{uv}\| \sim R^2$. If we further consider the limit $k_z \to \infty$ and rescale the wall normal coordinate $Y = k_z y$, we find

$$\|H_{uv}\| = \nabla^{-2}\bar{U}_y\nabla^{-2} = k_z^{-3}\tilde{\nabla}^{-2}\bar{U}_y\tilde{\nabla}^{-2}, \tag{A.15}$$

where $\tilde{\nabla}^2 = \frac{\partial^2}{\partial Y^2} - 1$. Thus for $k_x = 0$ and as $\omega \to 0$, $R \to \infty$ and $k_z \to \infty$, we find that

$$\sigma_1 \sim R^2 k_z^{-3}. \tag{A.16}$$

A more in depth analysis can be found in Jovanović and Bamieh (2005).

A.4 Select Input Basis Elements

In this section, we plot a selection of representative input basis elements used in the 2D examples presented in this work. Figure A.2 shows four of the local resolvent modes used in the VRA reconstruction of the 2D resolvent modes computed about EQ1 in §3.3. Figure A.3 shows two of the local resolvent modes used in the reconstruction of the 2D resolvent modes computed about the ZPGTBL in §3.4. Figure A.3a represents a "wall-attached" mode used in the reconstruction of the global resolvent inner-mode with $[k_z, \omega] = [44.0, 1.8]$. Figure A.3b represents a "wall-detached" mode used for the outer-mode with $[k_z, \omega] = [11.0, 2.3]$.

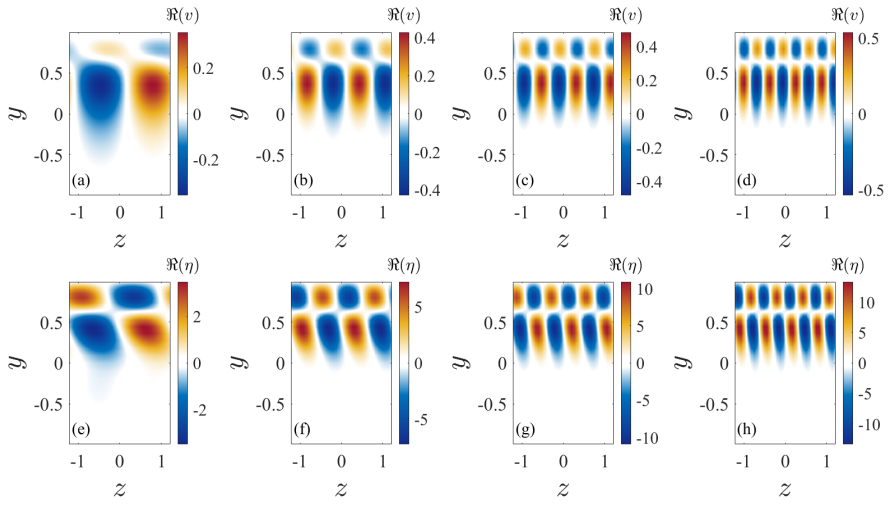

Figure A.2: Select elements of input resolvent basis: $q(y,z) = \psi_{k_x,k_z,\omega,j}(y)e^{ik_z z}$ for $k_x = 0.5$, $\omega = 0.375$, $j = 1$ and $L_z k_z/2\pi = 1$ (a,e), 2 (b,f), 3 (c,g), and 4 (d,h). Top row: v, bottom row: η.

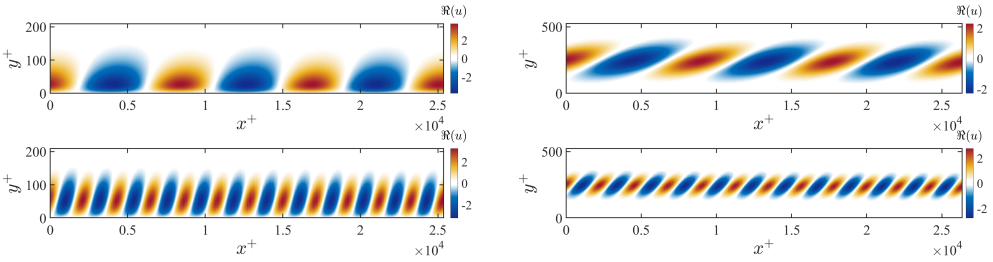

(a) (b)

Figure A.3: Select elements of input resolvent basis: $q(x,y) = \psi_{k_x,k_z,\omega,j}(y)e^{ik_x x}$ for $[k_z,\omega] = [44.0, 0.65U_\infty/k_x]$ (a) and $[k_z,\omega] = [11.0, 0.8U_\infty/k_x]$ (b). In both cases $L_x k_x/2\pi = 3$ (top panel) and 12 (lower panel), and in all cases $j = 1$.

A.5 Singular Value Sensitivity

The true singular value/mode pairs satisfy

$$\sigma_j^2 = \left(\mathbf{H}\boldsymbol{\phi}_j\right)^H \mathbf{Q}\left(\mathbf{H}\boldsymbol{\phi}_j\right) = \left(\left(\mathbf{L}\boldsymbol{\psi}_j\right)^H \mathbf{Q}\left(\mathbf{L}\boldsymbol{\psi}_j\right)\right)^{-1}. \tag{A.17}$$

Consider a perturbation to either $\boldsymbol{\psi}_j$ or $\boldsymbol{\phi}_j$:

$$\begin{aligned} \boldsymbol{\psi}_{j,\epsilon} &= \boldsymbol{\psi}_j + \epsilon\mathbf{r} \\ \boldsymbol{\phi}_{j,\epsilon} &= \boldsymbol{\phi}_j + \epsilon\mathbf{g} \end{aligned} \tag{A.18}$$

where $||\boldsymbol{\psi}_j|| = ||\boldsymbol{\phi}_j|| = ||\mathbf{r}|| = ||\mathbf{g}|| = 1$ and $\epsilon \ll 1$. The error in the singular value due to a perturbation in $\boldsymbol{\psi}$ may be bounded as follows.

$$\sigma_{j,\epsilon,L}^{-2} = \left(\mathbf{L}\left(\boldsymbol{\psi} + \epsilon\mathbf{r}\right)\right)^H \mathbf{Q}\left(\mathbf{L}\left(\boldsymbol{\psi} + \epsilon\mathbf{r}\right)\right) = \sigma_j^{-2} + 2\epsilon\Re\{\left(\mathbf{L}\boldsymbol{\psi}\right)^H \mathbf{Q}\left(\mathbf{L}\mathbf{r}\right)\} + \mathcal{O}(\epsilon^2) \tag{A.19}$$

Using the definition $\mathbf{L}\boldsymbol{\psi}_j = \sigma_j^{-1}\boldsymbol{\phi}$ and rearranging slightly we find

$$\sigma_{j,\epsilon,L} = \sigma_j \left(1 + 2\epsilon\sigma_j \Re\{(\boldsymbol{\phi})^H \mathbf{Q}\,(\mathbf{L}\mathbf{r})\}\right)^{-0.5}. \tag{A.20}$$

Taylor expanding for small ϵ gives

$$\sigma_{j,\epsilon,L} = \sigma_j \ - \epsilon\sigma_j^2 \Re\{(\boldsymbol{\phi})^H \mathbf{Q}\,(\mathbf{L}\mathbf{r})\} + O(\epsilon^2). \tag{A.21}$$

Further, applying the Cauchy-Schwartz inequality and noting that $\|\boldsymbol{\phi}_j\| = \|\mathbf{r}\| = 1$ leads to

$$\frac{|\sigma_{j,\epsilon,L} - \sigma_j\|}{\sigma_j} \leq \epsilon\sigma_j \|\mathbf{L}\|. \tag{A.22}$$

Conversely, the error in the singular value due to a perturbation in $\boldsymbol{\phi}$ may be bounded as follows.

$$\sigma_{j,\epsilon,H}^2 = (\mathbf{H}\,(\boldsymbol{\phi} + \epsilon\mathbf{g}))^H \mathbf{Q}\,(\mathbf{H}\,(\boldsymbol{\phi} + \epsilon\mathbf{g})) = \sigma_j^2 + 2\epsilon\Re\{(\mathbf{H}\boldsymbol{\psi})^H \mathbf{Q}\,(\mathbf{H}\mathbf{g})\} + O(\epsilon^2) \tag{A.23}$$

Using the definition $\mathbf{H}\boldsymbol{\phi}_j = \sigma_j\boldsymbol{\psi}$ and rearranging slightly, we find

$$\sigma_{j,\epsilon,H} = \sigma_j \left(1 + 2\epsilon\sigma_j^{-1} \Re\{(\boldsymbol{\psi})^H \mathbf{Q}\,(\mathbf{H}\mathbf{g})\}\right)^{0.5}. \tag{A.24}$$

Taylor expanding for small ϵ gives

$$\sigma_{j,\epsilon,H} = \sigma_j \ + \epsilon\Re\{\boldsymbol{\psi}^H \mathbf{Q}\,(\mathbf{H}\mathbf{g})\} + O(\epsilon^2). \tag{A.25}$$

Again, applying the Cauchy-Schwartz inequality and noting that given that $\|\boldsymbol{\psi}_j\| = \|\mathbf{g}\| = 1$ and $\|\mathbf{H}\| = \sigma_1$ leads to

$$\frac{|\sigma_{j,\epsilon,H} - \sigma_j\|}{\sigma_j} \leq \epsilon\frac{\sigma_1}{\sigma_j}. \tag{A.26}$$

A.6 Singular Mode Sensitivity

Here we derive bounds on the sensitivity of $\boldsymbol{\phi}_j$.

$$\boldsymbol{\phi}_{j,\epsilon,\psi} = \sigma_{j,\epsilon,L}\mathbf{L}\left(\boldsymbol{\psi}_j + \epsilon\mathbf{r}\right) = \sigma_{j,\epsilon,L}\mathbf{L}\boldsymbol{\psi}_j + \epsilon\sigma_{j,\epsilon,L}\mathbf{L}\mathbf{r} \tag{A.27}$$

Again, we assume $\|\boldsymbol{\psi}_j\| = \|\mathbf{r}\| = 1$ and $\epsilon \ll 1$. Subtracting $\boldsymbol{\phi}_j = \sigma_j\mathbf{L}\boldsymbol{\psi}_j$ from both sides and rearranging the right hand side slightly results in

$$\boldsymbol{\phi}_{j,\epsilon,\psi} - \boldsymbol{\phi}_j = \left(\sigma_{j,\epsilon,L} - \sigma_j\right)\mathbf{L}\boldsymbol{\psi}_j + \epsilon\left(\sigma_{j,\epsilon,L} - \sigma_j\right)\mathbf{L}\mathbf{r} + \epsilon\sigma_j\mathbf{L}\mathbf{r}. \tag{A.28}$$

We note from the results of Appendix A.5 that $\left(\sigma_{j,\epsilon,L} - \sigma_j\right) \sim \epsilon$ which allows us to write

$$\boldsymbol{\phi}_{j,\epsilon,\psi} - \boldsymbol{\phi}_j = \left(\sigma_{j,\epsilon,L} - \sigma_j\right)\mathbf{L}\boldsymbol{\psi}_j + \epsilon\sigma_j\mathbf{L}\mathbf{r} + O(\epsilon^2). \tag{A.29}$$

Next, we analyze the norm of both the left and right hand side, which upon application of the triangle inequality, the Cauchy-Schwartz inequality, and (A.22) results in

$$\|\boldsymbol{\phi}_{j,\epsilon,\psi} - \boldsymbol{\phi}_j\| \leq \epsilon \left(\sigma_j \|\mathbf{L}\| + 1\right) \sigma_j \|\mathbf{L}\|. \tag{A.30}$$

The same analysis may be applied to derive bounds on the sensitivity of $\boldsymbol{\psi}_j$,

$$\boldsymbol{\psi}_{j,\epsilon,\phi} \equiv \sigma_{j,\epsilon,H}^{-1} \mathbf{H} \left(\boldsymbol{\phi}_j + \epsilon \mathbf{g}\right) = \sigma_{j,\epsilon,H}^{-1} \mathbf{H} \boldsymbol{\phi}_j + \epsilon \sigma_{j,\epsilon,H}^{-1} \mathbf{H} \mathbf{g}, \tag{A.31}$$

where again we assume $\|\boldsymbol{\phi}_j\| = \|\mathbf{g}\| = 1$ and $\epsilon \ll 1$. Subtracting $\boldsymbol{\psi}_j = \sigma_j^{-1} \mathbf{H} \boldsymbol{\phi}_j$ from both sides and rearranging the right hand side slightly results in

$$\boldsymbol{\psi}_{j,\epsilon,\phi} - \boldsymbol{\psi}_j = \frac{\sigma_j - \sigma_{j,\epsilon,H}}{\sigma_j \sigma_{j,\epsilon,H}} \mathbf{H} \boldsymbol{\phi}_j + \epsilon \frac{\sigma_j - \sigma_{j,\epsilon,H}}{\sigma_j \sigma_{j,\epsilon,H}} \mathbf{H} \mathbf{g} + \epsilon \sigma_j^{-1} \mathbf{H} \mathbf{g}. \tag{A.32}$$

Taylor expanding about $\epsilon = 0$ and noting that $\left(\sigma_{j,\epsilon,H} - \sigma_j\right) \sim \epsilon$ results in

$$\boldsymbol{\psi}_{j,\epsilon,\phi} - \boldsymbol{\psi}_j = \frac{\sigma_j - \sigma_{j,\epsilon,H}}{\sigma_j^2} \mathbf{H} \boldsymbol{\phi}_j + \epsilon \sigma_j^{-1} \mathbf{H} \mathbf{g} + O(\epsilon^2). \tag{A.33}$$

Next we analyze the norm of both the left and right hand side, which upon application of the triangle inequality, the Cauchy-Schwartz inequality, and (A.26) results in

$$\|\boldsymbol{\psi}_{j,\epsilon,\phi} - \boldsymbol{\psi}_j\| \leq \epsilon \left(\frac{\sigma_1}{\sigma_j} + 1\right) \frac{\sigma_1}{\sigma_j}. \tag{A.34}$$

Appendix B

CHAPTERS IV-V

B.1 Linear Operator for Taylor Vortex Flow

The Navier-Stokes operator in cylindrical coordinates linearized about a one-dimensional azimuthal mean flow $U(r)$ and Fourier transformed in z, θ, and t is given by

$$\mathcal{L}_{\mathbf{k}} = \begin{bmatrix} \frac{inU}{r} + \frac{1}{R}\left(\frac{1}{r^2} - \nabla^2\right) & \frac{1}{R}\left(\frac{2in}{r^2}\right) - \frac{2U}{r} & 0 & \frac{\partial}{\partial r} \\ \left(\frac{\partial U}{\partial r} + \frac{U}{r}\right) - \frac{1}{R}\left(\frac{2in}{r^2}\right) & \frac{inU}{r} + \frac{1}{R}\left(\frac{1}{r^2} - \nabla^2\right) & 0 & \frac{in}{r} \\ 0 & 0 & \frac{inU}{r} - \frac{1}{R}\nabla^2 & ik \\ \frac{1}{r} + \frac{\partial}{\partial r} & \frac{in}{r} & ik & 0 \end{bmatrix}, \quad \text{(B.1)}$$

where the Laplacian operator is defined as

$$\nabla^2 = \frac{\partial^2}{\partial r^2} + \frac{1}{r}\frac{\partial}{\partial r} - \left(k^2 + \frac{n^2}{r^2}\right). \quad \text{(B.2)}$$

The weight matrix, M, is defined as

$$M \equiv \begin{bmatrix} 1 & 0 & 0 & 0 \\ 0 & 1 & 0 & 0 \\ 0 & 0 & 1 & 0 \\ 0 & 0 & 0 & 0 \end{bmatrix}. \quad \text{(B.3)}$$

Appendix C

CHAPTER VI

C.1 Intra-Triad Energy Transfer in Frequency Space

Here we verify that the results derived in the time domain by Schmid and Henningson (2001) are also valid in the frequency domain. Consider the Triad of wavenumbers $\mathbf{a} = \mathbf{b} + \mathbf{c}$, where $\mathbf{a} = [\alpha_a, \beta_a, \omega_a]$, $\mathbf{b} = [\alpha_b, \beta_b, \omega_b]$, and $\mathbf{c} = [\alpha_c, \beta_c, \omega_c]$. We define the quantity

$$E_{\mathbf{a},\mathbf{b},\mathbf{c}} = \mathcal{R}\left\{\int \hat{\mathbf{u}}^*_{\mathbf{a},i}\hat{\mathbf{u}}_{\mathbf{b},j}\frac{\partial}{\partial x_j}\left(\hat{\mathbf{u}}_{\mathbf{c},i}\right)dy\right\} \tag{C.1}$$

where summation over the indices $i, j = 1, 2, 3$ is assumed. Note that since (C.1) is defined as the real part, we have the symmetry $E_{\mathbf{a},\mathbf{b},\mathbf{c}} = E_{-\mathbf{a},-\mathbf{b},-\mathbf{c}}$. Integrating by parts leads to

$$E_{\mathbf{a},\mathbf{b},\mathbf{c}} = \mathcal{R}\left\{\int \frac{\partial}{\partial x_j}\left(\hat{\mathbf{u}}^*_{\mathbf{a},i}\hat{\mathbf{u}}_{\mathbf{b},j}\hat{\mathbf{u}}_{\mathbf{c},i}\right)dy - \int \hat{\mathbf{u}}_{\mathbf{c},i}\frac{\partial}{\partial x_j}\left(\hat{\mathbf{u}}^*_{\mathbf{a},i}\hat{\mathbf{u}}_{\mathbf{b},j}\right)dy\right\}. \tag{C.2}$$

The first term in (C.2) vanishes due to the homogeneous Dirichlet boundary conditions relevant to the wall bounded flows considered here.

$$E_{\mathbf{a},\mathbf{b},\mathbf{c}} = \mathcal{R}\left\{-\int \hat{\mathbf{u}}_{\mathbf{c},i}\frac{\partial}{\partial x_j}\left(\hat{\mathbf{u}}^*_{\mathbf{a},i}\hat{\mathbf{u}}_{\mathbf{b},j}\right)dy\right\}. \tag{C.3}$$

Integrating by parts again leads to

$$E_{\mathbf{a},\mathbf{b},\mathbf{c}} = \mathcal{R}\left\{-\int \hat{\mathbf{u}}_{\mathbf{c},i}\left(\hat{\mathbf{u}}^*_{\mathbf{a},i}\frac{\partial}{\partial x_j}\left(\hat{\mathbf{u}}_{\mathbf{b},j}\right) + \hat{\mathbf{u}}_{\mathbf{b},j}\frac{\partial}{\partial x_j}\left(\hat{\mathbf{u}}^*_{\mathbf{a},i}\right)\right)dy\right\}. \tag{C.4}$$

The first term of (C.3) vanishes due to the continuity constraint that $\nabla \cdot \mathbf{u} = 0$.

$$E_{\mathbf{a},\mathbf{b},\mathbf{c}} = \mathcal{R}\left\{-\int \hat{\mathbf{u}}_{\mathbf{c},i}\hat{\mathbf{u}}_{\mathbf{b},j}\frac{\partial}{\partial x_j}\left(\hat{\mathbf{u}}^*_{\mathbf{a},i}\right)dy\right\} = -E_{-\mathbf{c},\mathbf{b},-\mathbf{a}} \tag{C.5}$$

This indicates that

$$E_{\mathbf{a},\mathbf{b},\mathbf{c}} + E_{-\mathbf{c},\mathbf{b},-\mathbf{a}} = 0. \tag{C.6}$$

Similarly we can show that

$$E_{\mathbf{a},\mathbf{c},\mathbf{b}} + E_{-\mathbf{b},\mathbf{c},-\mathbf{a}} = 0. \tag{C.7}$$

The energy transfer from the interaction of modes $\hat{\mathbf{u}}_{\mathbf{b}}(y)$ and $\hat{\mathbf{u}}_{\mathbf{c}}(y)$ to mode $\hat{\mathbf{u}}_{\mathbf{a}}(y)$ is then given by

$$T_{\mathbf{a}} = E_{\mathbf{a},\mathbf{b},\mathbf{c}} + E_{\mathbf{a},\mathbf{c},\mathbf{b}}. \tag{C.8}$$

Similarly, the energy transfer from the interaction of modes $\hat{\mathbf{u}}_{\mathbf{a}}(y)$ and $\hat{\mathbf{u}}_{-\mathbf{c}}(y)$ to mode $\hat{\mathbf{u}}_{\mathbf{b}}(y)$ and the energy transfer from $\hat{\mathbf{u}}_{\mathbf{a}}(y)$ and $\hat{\mathbf{u}}_{-\mathbf{b}}(y)$ to mode $\hat{\mathbf{u}}_{\mathbf{c}}(y)$ are given by

$$T_{\mathbf{b}} = E_{\mathbf{b},\mathbf{a},-\mathbf{c}} + E_{\mathbf{b},-\mathbf{c},\mathbf{a}} \tag{C.9}$$

$$T_{\mathbf{c}} = E_{\mathbf{c},\mathbf{a},-\mathbf{b}} + E_{\mathbf{c},-\mathbf{b},\mathbf{a}} \tag{C.10}$$

where

$$E_{\mathbf{b},\mathbf{a},-\mathbf{c}} + E_{\mathbf{c},\mathbf{a},-\mathbf{b}} = 0 \tag{C.11}$$

$$E_{\mathbf{b},-\mathbf{c},\mathbf{a}} + E_{-\mathbf{a},-\mathbf{c},-\mathbf{b}} = 0 \tag{C.12}$$

$$E_{\mathbf{c},\mathbf{a},-\mathbf{b}} + E_{\mathbf{b},\mathbf{a},-\mathbf{c}} = 0 \tag{C.13}$$

$$E_{\mathbf{c},-\mathbf{b},\mathbf{a}} + E_{-\mathbf{a},-\mathbf{b},-\mathbf{c}} = 0. \tag{C.14}$$

Summing (C.6), (C.7) and (C.11)-(C.14) and utilizing the fact that $E_{\mathbf{a},\mathbf{b},\mathbf{c}} = E_{-\mathbf{a},-\mathbf{b},-\mathbf{c}}$ leads to

$$T_{\mathbf{a},\mathbf{b},\mathbf{c}} \equiv T_{\mathbf{a}} + T_{\mathbf{b}} + T_{\mathbf{c}} = 0. \tag{C.15}$$

We define the quantity $T_{\mathbf{a},\mathbf{b},\mathbf{c}}$ as the *"intra-triad energy transfer"*, but reiterate that the result (C.15) is originally due to Schmid and Henningson (2001). We simply verify its validity in the temporal frequency domain.

C.2 Fourier Symmetries of Governing Equations

Evaluating the linearized Navier-Stokes or Orr-Sommerfeld/Squire operator reveals that the resolvent modes $\psi_{\mathbf{k},j}$, $\phi_{\mathbf{k},j}$ as well as the Fourier modes of the response and forcing, $\hat{\mathbf{u}}_{\mathbf{k}}$, $\hat{\mathbf{f}}_{\mathbf{k}}$ obey the symmetries (6.13-6.15). This allows us to derive the symmetries of the resolvent weights which are defined as

$$\chi_{\mathbf{k},j} \equiv \langle \phi_{\mathbf{k},j}, \hat{\mathbf{f}}_{\mathbf{k}} \rangle \tag{C.16}$$

$$\chi_{\mathbf{k},j} = \langle \phi^*_{x,\mathbf{k},j} \hat{f}_{x,\mathbf{k}} + \phi^*_{y,\mathbf{k},j} \hat{f}_{y,\mathbf{k}} + \phi^*_{z,\mathbf{k},j} \hat{f}_{z,\mathbf{k}} \rangle. \tag{C.17}$$

The transformation $k_z \longrightarrow -k_z$ leads to

$$\tilde{\chi}_{\mathbf{k},j} = \langle \phi^*_{x,\mathbf{k},j} \hat{f}_{x,\mathbf{k}} + \phi^*_{y,\mathbf{k},j} \hat{f}_{y,\mathbf{k}} + (-\phi^*_{z,\mathbf{k},j})(-\hat{f}_{z,\mathbf{k}}) \rangle. \tag{C.18}$$

$$\tilde{\chi}_{\tilde{\mathbf{k}},j} = \langle \phi^*_{x,\mathbf{k},j} \hat{f}_{x,\mathbf{k}} + \phi^*_{y,\mathbf{k},j} \hat{f}_{y,\mathbf{k}} + \phi^*_{z,\mathbf{k},j} \hat{f}_{z,\mathbf{k}} \rangle = \chi_{\mathbf{k},j} \tag{C.19}$$

The weights are unaffected by the transformation $k_z \to -k_z$. This confirms that the full Fourier mode $\hat{\mathbf{u}}_{\mathbf{k}} = \chi_{\mathbf{k},j}\sigma_{\mathbf{k},j}\psi_{\mathbf{k},j}$ obeys the same symmetry as $\psi_{\mathbf{k},j}$, namely,

$$\hat{\mathbf{u}}_{\mathbf{k}} = [\hat{u}, \hat{v}, \hat{w}] \to [\hat{u}, \hat{v}, -\hat{w}] \tag{C.20}$$

as $k_z \to -k_z$. The transformation as $k_x \to -k_x$ follows immediately. The combination of the derived conclusion that $\chi_{\mathbf{k},j}$ is independent of the sign of k_z and the requirement that the physical space representation of the velocity is real necessitates that the negation of k_x results in the conjugation of $\chi_{\mathbf{k},j}$, i.e. as $k_x \to -k_x$, we have $\chi_{\mathbf{k},j} \to \chi^*_{\mathbf{k},j}$ We note that these Fourier symmetries are true in the resolvent form but generally not observed in DNS which is formulated in the time domain.

Bibliography

C. David Andereck, S. S. Liu, and Harry L. Swinney. Flow regimes in a circular Couette system with independently rotating cylinders. *Journal of Fluid Mechanics*, 164:155–183, March 1986.

C. Arratia and J.-M. Chomaz. On the longitudinal optimal perturbations to inviscid plane shear flow: formal solution and asymptotic approximation. *Journal of Fluid Mechanics*, 737:387–411, December 2013.

D Barkley. Linear analysis of the cylinder wake mean flow. *Europhysics Letters (EPL)*, 75:750–756, September 2006.

D. Barkley. Theoretical perspective on the route to turbulence in a pipe. *Journal of Fluid Mechanics*, 803, September 2016.

Benedikt Barthel, Xiaojue Zhu, and Beverley McKeon. Closing the loop: nonlinear Taylor vortex flow through the lens of resolvent analysis. *Journal of Fluid Mechanics*, 924, October 2021.

Cédric Beaume, Gregory P. Chini, Keith Julien, and Edgar Knobloch. Reduced description of exact coherent states in parallel shear flows. *Physical Review E*, 91 (4):043010, April 2015.

Yacine Bengana and Laurette S. Tuckerman. Spirals and ribbons in counter-rotating Taylor-Couette flow: Frequencies from mean flows and heteroclinic orbits. *Physical Review Fluids*, 4(4):044402, April 2019.

Yacine Bengana and Laurette S. Tuckerman. Frequency prediction from exact or self-consistent meanflows. *arXiv:2102.07255 [physics]*, February 2021.

Luca Brandt. The lift-up effect: The linear mechanism behind transition and turbulence in shear flows. *European Journal of Mechanics - B/Fluids*, 47:80–96, September 2014.

D.H. Brandwood. A complex gradient operator and its application in adaptive array theory. *IEE Proceedings F - Communications, Radar and Signal Processing*, 130 (1):11–16, February 1983.

M. P. Brenner, J. D. Eldredge, and J. B. Freund. Perspective on machine learning for advancing fluid mechanics. *Physical Review Fluids*, 4(10):100501, October 2019.

Steven L. Brunton. Applying Machine Learning to Study Fluid Mechanics. *arXiv:2110.02083 [physics]*, October 2021.

W. Cheng, D. I. Pullin, and R. Samtaney. Large-eddy simulation and modelling of Taylor–Couette flow. *Journal of Fluid Mechanics*, 890, May 2020.

Donald Coles. Transition in circular Couette flow. *Journal of Fluid Mechanics*, 21 (3):385–425, March 1965.

A. Davey. The growth of Taylor vortices in flow between rotating cylinders. *Journal of Fluid Mechanics*, 14(3):336–368, November 1962.

Scott T. M. Dawson and Beverley J. McKeon. On the shape of resolvent modes in wall-bounded turbulence. *Journal of Fluid Mechanics*, 877:682–716, October 2019.

Tommy Dessup, Laurette S. Tuckerman, José Eduardo Wesfreid, Dwight Barkley, and Ashley P. Willis. Self-sustaining process in Taylor-Couette flow. *Physical Review Fluids*, 3(12):123902, December 2018.

C. L. Dolph and D. C. Lewis. On the application of infinite systems of ordinary differential equations to perturbations of plane Poiseuille flow. *Quarterly of Applied Mathematics*, 16(2):97–110, 1958.

P. G. Drazin and W. H. Reid. *Hydrodynamic Stability*. Cambridge Mathematical Library. Cambridge University Press, Cambridge, 2 edition, 2004.

Yves-Marie Ducimetière, Edouard Boujo, and François Gallaire. Weak nonlinearity for strong nonnormality. *arXiv:2110.08064 [physics]*, October 2021.

Bruno Eckhardt, Siegfried Grossmann, and Detlef Lohse. Torque scaling in turbulent Taylor–Couette flow between independently rotating cylinders. *Journal of Fluid Mechanics*, 581:221–250, June 2007.

Brian F. Farrell and Petros J. Ioannou. Dynamics of streamwise rolls and streaks in turbulent wall-bounded shear flow. *Journal of Fluid Mechanics*, 708:149–196, October 2012.

Brian F. Farrell, Petros J. Ioannou, Javier Jiménez, Navid C. Constantinou, Adrián Lozano-Durán, and Marios-Andreas Nikolaidis. A statistical state dynamics-based study of the structure and mechanism of large-scale motions in plane Poiseuille flow. *Journal of Fluid Mechanics*, 809:290–315, December 2016.

Oscar Flores and Javier Jiménez. Effect of wall-boundary disturbances on turbulent channel flows. *Journal of Fluid Mechanics*, 566:357–376, November 2006.

F. Gallaire, E. Boujo, V. Mantic-Lugo, C. Arratia, B. Thiria, and P. Meliga. Pushing amplitude equations far from threshold: application to the supercritical Hopf bifurcation in the cylinder wake. *Fluid Dynamics Research*, 48(6):061401, December 2016.

X. Garnaud, L. Lesshafft, P. J. Schmid, and P. Huerre. The preferred mode of incompressible jets: linear frequency response analysis. *Journal of Fluid Mechanics*, 716:189–202, February 2013.

D. F. Gayme, B. J. McKeon, A. Papachristodoulou, B. Bamieh, and J. C. Doyle. A streamwise constant model of turbulence in plane Couette flow. *Journal of Fluid Mechanics*, 665:99–119, December 2010.

Thomas Gebhardt and Siegfried Grossmann. The Taylor-Couette eigenvalue problem with independently rotating cylinders. *Zeitschrift für Physik B Condensed Matter*, 90(4):475–490, December 1993.

J. F. Gibson. A spectral Navier-Stokes simulator in C++. Technical report, U. New Hampshire, 2014.

J. F. Gibson, J. Halcrow, and P. Cvitanović. Visualizing the geometry of state space in plane Couette flow. *Journal of Fluid Mechanics*, 611:107–130, September 2008.

Michael Grant and Stephen Boyd. CVX: Matlab software for disciplined convex programming, version 2.1. `http://cvxr.com/cvx`, March 2014.

Siegfried Grossmann, Detlef Lohse, and Chao Sun. High–Reynolds Number Taylor-Couette Turbulence. *Annual Review of Fluid Mechanics*, 48(1):53–80, 2016.

F. Gómez and H. M. Blackburn. Data-driven approach to design of passive flow control strategies. *Physical Review Fluids*, 2(2):021901, February 2017.

N. Halko, P. G. Martinsson, and J. A. Tropp. Finding Structure with Randomness: Probabilistic Algorithms for Constructing Approximate Matrix Decompositions. *SIAM Review*, 53(2):217–288, January 2011.

James M. Hamilton, John Kim, and Fabian Waleffe. Regeneration mechanisms of near-wall turbulence structures. *Journal of Fluid Mechanics*, 287:317–348, March 1995.

Carlos G. Hernández and Yongyun Hwang. Spectral energetics of a quasilinear approximation in uniform shear turbulence. *Journal of Fluid Mechanics*, 904, December 2020.

Carlos G. Hernández, Qiang Yang, and Yongyun Hwang. Generalised quasilinear approximations of turbulent channel flow: Part 1. Streamwise nonlinear energy transfer. *arXiv:2108.12395 [physics]*, August 2021.

Benjamin Herrmann, Peter J. Baddoo, Richard Semaan, Steven L. Brunton, and Beverley J. McKeon. Data-driven resolvent analysis. *Journal of Fluid Mechanics*, 918, July 2021.

Sergio Hoyas and Javier Jiménez. Scaling of the velocity fluctuations in turbulent channels up to $re_\tau = 2003$. *Physics of Fluids*, 18:011702, January 2006.

Sander G. Huisman, Roeland C. A. van der Veen, Chao Sun, and Detlef Lohse. Multiple states in highly turbulent Taylor-Couette flow. *Nature Communications*, 5:3820, May 2014.

N. Hutchins and Ivan Marusic. Evidence of very long meandering features in the logarithmic region of turbulent boundary layers. *Journal of Fluid Mechanics*, 579:1–28, May 2007a.

Nicholas Hutchins and Ivan Marusic. Large-scale influences in near-wall turbulence. *Philosophical Transactions of the Royal Society A: Mathematical, Physical and Engineering Sciences*, 365(1852):647–664, March 2007b.

Yongyun Hwang and Carlo Cossu. Linear non-normal energy amplification of harmonic and stochastic forcing in the turbulent channel flow. *Journal of Fluid Mechanics*, 664:51–73, December 2010.

Yongyun Hwang and Bruno Eckhardt. Attached eddy model revisited using a minimal quasi-linear approximation. *Journal of Fluid Mechanics*, 894, July 2020.

Simon J. Illingworth. Streamwise-constant large-scale structures in Couette and Poiseuille flows. *Journal of Fluid Mechanics*, 889, April 2020.

Ian Jacobi, Daniel Chung, Subrahmanyam Duvvuri, and Beverley J. McKeon. Interactions between scales in wall turbulence: phase relationships, amplitude modulation and the importance of critical layers. *Journal of Fluid Mechanics*, 914, May 2021.

Jinah Jeun, Joseph W. Nichols, and Mihailo R. Jovanović. Input-output analysis of high-speed axisymmetric isothermal jet noise. *Physics of Fluids*, 28(4):047101, April 2016.

Javier Jiménez. Coherent structures in wall-bounded turbulence. *Journal of Fluid Mechanics*, 842, May 2018.

Javier Jiménez and Parviz Moin. The minimal flow unit in near-wall turbulence. *Journal of Fluid Mechanics*, 225:213–240, April 1991.

C. A. Jones. Nonlinear Taylor vortices and their stability. *Journal of Fluid Mechanics*, 102:249–261, January 1981.

Mihailo R. Jovanović and Bassam Bamieh. Componentwise energy amplification in channel flows. *Journal of Fluid Mechanics*, 534:145–183, July 2005.

S. J. Kline, W. C. Reynolds, F. A. Schraub, and P. W. Runstadler. The structure of turbulent boundary layers. *Journal of Fluid Mechanics*, 30(4):741–773, December 1967.

Dmitrii Kochkov, Jamie A. Smith, Ayya Alieva, Qing Wang, Michael P. Brenner, and Stephan Hoyer. Machine learning–accelerated computational fluid dynamics. *Proceedings of the National Academy of Sciences*, 118(21), May 2021.

Vladislav Mantič-Lugo, Cristóbal Arratia, and François Gallaire. Self-consistent mean flow description of the nonlinear saturation of the vortex shedding in the cylinder wake. *Physical Review Letters*, 113(8):084501, August 2014.

Vladislav Mantič-Lugo, Cristóbal Arratia, and François Gallaire. A self-consistent model for the saturation dynamics of the vortex shedding around the mean flow in the unstable cylinder wake. *Physics of Fluids*, 27(7):074103, July 2015.

Philip S. Marcus. Simulation of Taylor-Couette flow. Part 1. Numerical methods and comparison with experiment. *Journal of Fluid Mechanics*, 146:45–64, September 1984.

Simon Maretzke, Björn Hof, and Marc Avila. Transient growth in linearly stable Taylor–Couette flows. *Journal of Fluid Mechanics*, 742:254–290, March 2014.

J. B. Marston, G. P. Chini, and S. M. Tobias. Generalized quasilinear approximation: Application to zonal jets. *Physical Review Letters*, 116(21):214501, May 2016.

Eduardo Martini, Daniel Rodríguez, Aaron Towne, and André V. G. Cavalieri. Efficient computation of global resolvent modes. *Journal of Fluid Mechanics*, 919, July 2021.

I. Marusic, B. J. McKeon, P. A. Monkewitz, H. M. Nagib, A. J. Smits, and K. R. Sreenivasan. Wall-bounded turbulent flows at high Reynolds numbers: Recent advances and key issues. *Physics of Fluids*, 22(6):065103, June 2010.

Ivan Marusic and Jason P. Monty. Attached eddy model of wall turbulence. *Annual Review of Fluid Mechanics*, 51(1):49–74, 2019.

Romain Mathis, Nicholas Hutchins, and Ivan Marusic. Large-scale amplitude modulation of the small-scale structures in turbulent boundary layers. *Journal of Fluid Mechanics*, 628:311–337, June 2009.

Romain Mathis, Ivan Marusic, Nicholas Hutchins, and K. R. Sreenivasan. The relationship between the velocity skewness and the amplitude modulation of the small scale by the large scale in turbulent boundary layers. *Physics of Fluids*, 23(12):121702, December 2011. ISSN 1070-6631. doi: 10.1063/1.3671738. URL https://aip-scitation-org.caltech.idm.oclc.org/doi/full/10.1063/1.3671738. Publisher: American Institute of Physics.

B. J. McKeon. The engine behind (wall) turbulence: perspectives on scale interactions. *Journal of Fluid Mechanics*, 817, April 2017.

B. J. McKeon and A. S. Sharma. A critical-layer framework for turbulent pipe flow. *Journal of Fluid Mechanics*, 658:336–382, September 2010.

Beverley J. McKeon. Self-similar hierarchies and attached eddies. *Physical Review Fluids*, 4(8):082601, August 2019.

Ryan M. McMullen, Kevin Rosenberg, and Beverley J. McKeon. Interaction of forced Orr-Sommerfeld and Squire modes in a low-order representation of turbulent channel flow. *Physical Review Fluids*, 5(8):084607, August 2020.

R. Moarref, M. R. Jovanović, J. A. Tropp, A. S. Sharma, and B. J. McKeon. A low-order decomposition of turbulent channel flow via resolvent analysis and convex optimization. *Physics of Fluids*, 26(5):051701, May 2014a.

Rashad Moarref, Ati S. Sharma, Joel A. Tropp, and Beverley J. McKeon. Model-based scaling of the streamwise energy density in high-Reynolds-number turbulent channels. *Journal of Fluid Mechanics*, 734:275–316, November 2013.

Rashad Moarref, Ati S. Sharma, Joel A. Tropp, and Beverley J. McKeon. A foundation for analytical developments in the logarithmic region of turbulent channels. *arXiv:1409.6047 [physics]*, September 2014b.

Antonios Monokrousos, Espen Åkervik, Luca Brandt, and Dan S. Henningson. Global three-dimensional optimal disturbances in the Blasius boundary-layer flow using time-steppers. *Journal of Fluid Mechanics*, 650:181–214, May 2010.

Pierluigi Morra, Petrônio A. S. Nogueira, André V. G. Cavalieri, and Dan S. Henningson. The colour of forcing statistics in resolvent analyses of turbulent channel flows. *Journal of Fluid Mechanics*, 907:A24, January 2021.

M. Nagata. Three-dimensional finite-amplitude solutions in plane Couette flow: bifurcation from infinity. *Journal of Fluid Mechanics*, 217:519–527, August 1990.

Petrônio A. S. Nogueira, André V. G. Cavalieri, Peter Jordan, and Vincent Jaunet. Large-scale streaky structures in turbulent jets. *Journal of Fluid Mechanics*, 873: 211–237, August 2019.

Petrônio A. S. Nogueira, André V. G. Cavalieri, Ardeshir Hanifi, and Dan S. Henningson. Resolvent analysis in unbounded flows: role of free-stream modes. *Theoretical and Computational Fluid Dynamics*, 34(1-2):163–176, April 2020.

Petrônio A. S. Nogueira, Pierluigi Morra, Eduardo Martini, André V. G. Cavalieri, and Dan S. Henningson. Forcing statistics in resolvent analysis: application in minimal turbulent Couette flow. *Journal of Fluid Mechanics*, 908, February 2021.

Rodolfo Ostilla, Richard J. A. M. Stevens, Siegfried Grossmann, Roberto Verzicco, and Detlef Lohse. Optimal Taylor–Couette flow: direct numerical simulations. *Journal of Fluid Mechanics*, 719:14–46, March 2013.

Rodolfo Ostilla-Mónico, Erwin P. van der Poel, Roberto Verzicco, Siegfried Grossmann, and Detlef Lohse. Exploring the phase diagram of fully turbulent Taylor–Couette flow. *Journal of Fluid Mechanics*, 761:1–26, December 2014a.

Rodolfo Ostilla-Mónico, Erwin P. van der Poel, Roberto Verzicco, Siegfried Grossmann, and Detlef Lohse. Boundary layer dynamics at the transition between the classical and the ultimate regime of Taylor-Couette flow. *Physics of Fluids*, 26 (1):015114, January 2014b.

Ethan Pickering, Georgios Rigas, Oliver T. Schmidt, Denis Sipp, and Tim Colonius. Optimal eddy viscosity for resolvent-based models of coherent structures in turbulent jets. *Journal of Fluid Mechanics*, 917, June 2021.

Stephen B. Pope. *Turbulent Flows*. Cambridge University Press, Cambridge, 2000.

Wei Ran, Armin Zare, Joseph W. Nichols, and Mihailo R. Jovanovic. The effect of sponge layers on global stability analysis of Blasius boundary layer flow. In *47th AIAA Fluid Dynamics Conference*, AIAA AVIATION Forum. American Institute of Aeronautics and Astronautics, June 2017.

Wei Ran, Armin Zare, M. J. Philipp Hack, and Mihailo R. Jovanović. Stochastic receptivity analysis of boundary layer flow. *Physical Review Fluids*, 4(9):093901, September 2019.

David Rand. Dynamics and symmetry. Predictions for modulated waves in rotating fluids. *Archive for Rational Mechanics and Analysis*, 79(1):1–37, July 1982.

Osborne Reynolds. XXIX. An experimental investigation of the circumstances which determine whether the motion of water shall be direct or sinuous, and of the law of resistance in parallel channels. *Philosophical Transactions of the Royal Society of London*, 174:935–982, January 1883.

Jean Hélder Marques Ribeiro, Chi-An Yeh, and Kunihiko Taira. Randomized resolvent analysis. *Physical Review Fluids*, 5(3):033902, March 2020.

Georgios Rigas, Denis Sipp, and Tim Colonius. Nonlinear input/output analysis: application to boundary layer transition. *Journal of Fluid Mechanics*, 911, March 2021.

Carlos Rosales and Charles Meneveau. A minimal multiscale Lagrangian map approach to synthesize non-Gaussian turbulent vector fields. *Physics of Fluids*, 18(7):075104, July 2006.

Kevin Rosenberg. *Resolvent-based modeling of flows in a channel*. PhD thesis, California Institute of Technology, May 2018.

Kevin Rosenberg and Beverley J. McKeon. Computing exact coherent states in channels starting from the laminar profile: A resolvent-based approach. *Physical Review E*, 100(2):021101, August 2019a.

Kevin Rosenberg and Beverley J. McKeon. Efficient representation of exact coherent states of the Navier–Stokes equations using resolvent analysis. *Fluid Dynamics Research*, 51(1):011401, January 2019b.

Kevin Rosenberg, Sean Symon, and Beverley J. McKeon. Role of parasitic modes in nonlinear closure via the resolvent feedback loop. *Physical Review Fluids*, 4: 052601, May 2019.

Joseph Ruan and Guillaume Blanquart. Direct numerical simulations of a statistically stationary streamwise periodic boundary layer via the homogenized Navier-Stokes equations. *Physical Review Fluids*, 6(2):024602, February 2021.

Francesco Sacco, Roberto Verzicco, and Rodolfo Ostilla-Mónico. Dynamics and evolution of turbulent Taylor rolls. *Journal of Fluid Mechanics*, 870:970–987, July 2019.

Philipp Schlatter and Ramis Örlü. Assessment of direct numerical simulation data of turbulent boundary layers. *Journal of Fluid Mechanics*, 659:116–126, September 2010a.

Philipp Schlatter and Ramis Örlü. Quantifying the interaction between large and small scales in wall-bounded turbulent flows: A note of caution. *Physics of Fluids*, 22(5), May 2010b.

Peter J. Schmid and Luca Brandt. Analysis of Fluid Systems: Stability, Receptivity, Sensitivity. *Applied Mechanics Reviews*, 66(2):024803, March 2014.

Peter J. Schmid and Dan S. Henningson. *Stability and Transition in Shear Flows*, volume 142 of *Applied Mathematical Sciences*. Springer New York, New York, NY, 2001.

Oliver T. Schmidt, Aaron Towne, Georgios Rigas, Tim Colonius, and Guillaume A. Brès. Spectral analysis of jet turbulence. *Journal of Fluid Mechanics*, 855: 953–982, November 2018.

A. S. Sharma, R. Moarref, and B. J. McKeon. Scaling and interaction of self-similar modes in models of high-Reynolds number wall turbulence. *Philosophical Transactions of the Royal Society A: Mathematical, Physical and Engineering Sciences*, 375(2089):20160089, March 2017.

Ati S. Sharma, Rashad Moarref, Beverley J. McKeon, Jae Sung Park, Michael D. Graham, and Ashley P. Willis. Low-dimensional representations of exact coherent states of the Navier-Stokes equations from the resolvent model of wall turbulence. *Physical Review E*, 93(2):021102, February 2016.

Denis Sipp and Olivier Marquet. Characterization of noise amplifiers with global singular modes: the case of the leading-edge flat-plate boundary layer. *Theoretical and Computational Fluid Dynamics*, 27(5):617–635, September 2013.

Nikolaos Skouloudis and Yongyun Hwang. Scaling of turbulence intensities up to $re_\tau = 10^6$ with a resolvent-based quasilinear approximation. *Physical Review Fluids*, 6(3):034602, March 2021.

Alexander J. Smits, Beverley J. McKeon, and Ivan Marusic. High–Reynolds Number Wall Turbulence. *Annual Review of Fluid Mechanics*, 43(1):353–375, 2011.

J. T. Stuart. On the non-linear mechanics of hydrodynamic stability. *Journal of Fluid Mechanics*, 4(1):1–21, May 1958.

J. T. Stuart. On the non-linear mechanics of wave disturbances in stable and unstable parallel flows Part 1. The basic behaviour in plane Poiseuille flow. *Journal of Fluid Mechanics*, 9(3):353–370, November 1960.

Sean Symon, Kevin Rosenberg, Scott T. M. Dawson, and Beverley J. McKeon. Non-normality and classification of amplification mechanisms in stability and resolvent analysis. *Physical Review Fluids*, 3(5):053902, May 2018.

Sean Symon, Denis Sipp, Peter J. Schmid, and Beverley J. McKeon. Mean and Unsteady Flow Reconstruction Using Data-Assimilation and Resolvent Analysis. *AIAA Journal*, 58(2):575–588, February 2020.

Sean Symon, Simon J. Illingworth, and Ivan Marusic. Energy transfer in turbulent channel flows and implications for resolvent modelling. *Journal of Fluid Mechanics*, 911, March 2021.

Kunihiko Taira, Steven L. Brunton, Scott T. M. Dawson, Clarence W. Rowley, Tim Colonius, Beverley J. McKeon, Oliver T. Schmidt, Stanislav Gordeyev, Vassilios Theofilis, and Lawrence S. Ukeiley. Modal Analysis of Fluid Flows: An Overview. *AIAA Journal*, 55(12):4013–4041, December 2017.

Geoffrey Ingram Taylor. VIII. Stability of a viscous liquid contained between two rotating cylinders. *Philosophical Transactions of the Royal Society of London. Series A, Containing Papers of a Mathematical or Physical Character*, 223(605-615):289–343, January 1923.

Vaughan L. Thomas, Binh K. Lieu, Mihailo R. Jovanović, Brian F. Farrell, Petros J. Ioannou, and Dennice F. Gayme. Self-sustaining turbulence in a restricted nonlinear model of plane Couette flow. *Physics of Fluids*, 26(10):105112, October 2014.

A. Towne, T. Colonius, P. Jordan, A. V. Cavalieri, and G. A. Brès. AIAA AVIATION Forum. June 2015. doi: 10.2514/6.2015-2217.

A. Towne, G. Rigas, E. Pickering, and T. Colonius. Efficient global resolvent analysis via the one-way Navier-Stokes equations. Part 1. Forced response. *arXiv:2111.09269 [physics]*, November 2021.

Aaron Towne, Oliver T. Schmidt, and Tim Colonius. Spectral proper orthogonal decomposition and its relationship to dynamic mode decomposition and resolvent analysis. *Journal of Fluid Mechanics*, 847:821–867, July 2018.

A. A. Townsend. The structure of the turbulent boundary layer. *Mathematical Proceedings of the Cambridge Philosophical Society*, 47(2):375–395, April 1951.

A. A. Townsend. Equilibrium layers and wall turbulence. *Journal of Fluid Mechanics*, 11(1):97–120, August 1961.

AAR Townsend. *The structure of turbulent shear flow*. Cambridge university press, 1980.

Lloyd N. Trefethen. *Spectral Methods in MATLAB*. Software, Environments and Tools. Society for Industrial and Applied Mathematics, January 2000.

Lloyd N. Trefethen and Mark Embree. Do pseudospectra determine behavior? In *Spectra and Pseudospectra*, The Behavior of Nonnormal Matrices and Operators, pages 437–441. Princeton University Press, 2005.

Lloyd N. Trefethen, Anne E. Trefethen, Satish C. Reddy, and Tobin A. Driscoll. Hydrodynamic Stability Without Eigenvalues. *Science*, 261(5121):578–584, July 1993.

Joel A. Tropp, Alp Yurtsever, Madeleine Udell, and Volkan Cevher. Streaming Low-Rank Matrix Approximation with an Application to Scientific Simulation. *SIAM Journal on Scientific Computing*, 41(4):A2430–A2463, January 2019.

Sam E. Turton, Laurette S. Tuckerman, and Dwight Barkley. Prediction of frequencies in thermosolutal convection from mean flows. *Physical Review E*, 91(4): 043009, April 2015.

Erwin P. van der Poel, Rodolfo Ostilla-Mónico, John Donners, and Roberto Verzicco. A pencil distributed finite difference code for strongly turbulent wall-bounded flows. *Computers & Fluids*, 116:10–16, August 2015.

Dennis P. M. van Gils, Gert-Wim Bruggert, Daniel P. Lathrop, Chao Sun, and Detlef Lohse. The Twente turbulent Taylor-Couette (T3C) facility: strongly turbulent (multiphase) flow between two independently rotating cylinders. *The Review of Scientific Instruments*, 82(2):025105, February 2011.

Dennis P. M. van Gils, Sander G. Huisman, Siegfried Grossmann, Chao Sun, and Detlef Lohse. Optimal Taylor–Couette turbulence. *Journal of Fluid Mechanics*, 706:118–149, September 2012.

R. Verzicco and P. Orlandi. A Finite-Difference Scheme for Three-Dimensional Incompressible Flows in Cylindrical Coordinates. *Journal of Computational Physics*, 123(2):402–414, February 1996.

Fabian Waleffe. On a self-sustaining process in shear flows. *Physics of Fluids*, 9(4): 883–900, April 1997.

J. Watson. On the non-linear mechanics of wave disturbances in stable and unstable parallel flows Part 2. The development of a solution for plane Poiseuille flow and for plane Couette flow. *Journal of Fluid Mechanics*, 9(3):371–389, November 1960.

W. Wirtinger. Zur formalen Theorie der Funktionen von mehr komplexen Veränderlichen. *Mathematische Annalen*, 97:357–376, 1927.

H. Yahata. Slowly-Varying Amplitude of the Taylor Vortices near the Instability Point. II: Mode-Coupling-Theoretical Approach. *Progress of Theoretical Physics*, 57(5):1490–1496, May 1977.

Chi-An Yeh and Kunihiko Taira. Resolvent-analysis-based design of airfoil separation control. *Journal of Fluid Mechanics*, 867:572–610, May 2019.

Armin Zare, Mihailo R. Jovanović, and Tryphon T. Georgiou. Colour of turbulence. *Journal of Fluid Mechanics*, 812:636–680, February 2017.

Xiaojue Zhu, Everett Phillips, Vamsi Spandan, John Donners, Gregory Ruetsch, Joshua Romero, Rodolfo Ostilla-Mónico, Yantao Yang, Detlef Lohse, Roberto Verzicco, Massimiliano Fatica, and Richard J. A. M. Stevens. AFiD-GPU: A versatile Navier–Stokes solver for wall-bounded turbulent flows on GPU clusters. *Computer Physics Communications*, 229:199–210, August 2018.

Emanuele Zuccoli and Franco Auteri. Derivation of the Ginzburg-Landau equation and its application to the Taylor-Couette flow. Master's thesis, Politecnico di Milano, 2019.

Juan C. Del Álamo, Javier Jiménez, Paulo Zandonade, and Robert D. Moser. Scaling of the energy spectra of turbulent channels. *Journal of Fluid Mechanics*, 500: 135–144, January 2004.